

A Photoabsorption Study of  $\text{La}^{3+}$  and Au in  
the Giant Resonance Energy Region

A thesis submitted for the degree of

**Doctor of Philosophy**

by

Ulrich Köble

Diplomphysiker

School of Physical Sciences


Dublin City University

August 1994

Research Supervisor

Prof Eugene T. Kennedy

I hereby certify that this material, which I now submit for assessment on the programme of study leading to the award of Doctor of Philosophy, is entirely my own work and has not been taken from the work of others save and to extent that such work has been cited and acknowledged within the text of my work

Signed 

Date 14/09/ 1994

Candidate

## Abstract

# A Photoabsorption Study of $\text{La}^{3+}$ and Au in the Giant Resonance Energy Region

The Dual Laser Plasma technique has been employed in order to investigate the time and space resolved photoabsorption behaviour of laser generated Ba, La, Ce, Eu and Au plasmas in the giant resonance energy region. For the first time, photoelectric based photoabsorption cross sections of  $\text{Ba}^+$ ,  $\text{Ba}^{2+}$ ,  $\text{La}^{3+}$  and Au have been measured. The study of the 4d photoabsorption behaviour of the X-isoelectronic sequence has been extended beyond  $\text{Ba}^{2+}$  to  $\text{La}^{3+}$  and atomic Au has been investigated in the 5p excitation region following previous results for the 5d transition metals W and Pt. Selected results for  $\text{Ba}^{2+}$ ,  $\text{La}^{3+}$  and Au have been discussed with use of *LS*-term dependent Hartree-Fock, (R)TDLDA/(R)LDA, RPAE/MBPT many body theories.

# Contents

<b>Introduction</b>	<b>8</b>
<b>1 Time and Space Resolved XUV Photoabsorption Experiment on Laser Produced Plasmas</b>	<b>11</b>
1 1 Experiment	11
1 2 Time and Space Resolved Photoabsorption Spectra of Laser Produced Plasmas	17
<b>2 The <i>ab initio</i> Theory of Atomic Structure</b>	<b>28</b>
2 1 The Independent Particle Approximation of a Multielectron System	29
2 2 Intra and Inter Configuration Interactions	36
2 2 1 Coulomb Interaction	38
2 2 2 Spin-Orbit Interaction	40
2 2 3 Relativistic Corrections	45
2 2 4 Intermediate Coupling	45
2 2 5 Interconfiguration Interactions	46
2 3 Electromagnetic Dipole Transitions	49
2 3 1 Resonant Photoabsorption	56
2 4 Many-Body Effects	61
2 4 1 RPAE	63
2 4 2 TDLDA	65
2 4 3 Self Energy	68

<b>3</b>	<b>Near Threshold 4d Photoabsorption in Xenon-like Lanthanum</b>	<b>71</b>
3 1	4d-Photoabsorption of Xe, Ba, La and the Rare Earths	72
3 2	4d-Photoabsorption in La <sup>3+</sup>	78
3 2 1	Configuration Interaction Hartree-Fock Calculations	80
3 2 2	Random Phase Approximation Calculations in Combination with the Many-Body Perturbation Theory	88
3 2 3	Time Dependent Local Density Approximation Calculations	92
3 2 4	Ba <sup>2+</sup> and La <sup>3+</sup> in Isoelectronic Comparison	95
3 2 5	4d Photoabsorption of La <sup>3+</sup> , Solid LaF <sub>3</sub> , LaCl <sub>3</sub> and La Metal	97
<b>4</b>	<b>XUV Photoabsorption of Laser Generated Au Vapour</b>	<b>102</b>
4 1	Introduction	102
4 2	Photoabsorption of Au in the 5p and 4f Excitation Region	104
4 3	Hartree-Fock Calculations for Au	109
4 4	Time Dependent Local Density Approximation Calculations for Au	112
4 5	Conclusion	113
	<b>Final Conclusion</b>	<b>115</b>

# List of Figures

1 1	Experimental setup of the DLP- facility	13
1 2	Schematic illustration of the DLP technique,	15
1 3	PDA spectra at 16 5inch without and with an absorbing La plasma	17
1 4	Photoabsorption of the Ba, Ba <sup>+</sup> and Ba <sup>2+</sup> isonuclear sequence using the RLDI technique	19
1 5	Photoabsorption of the Ba, Ba <sup>+</sup> and Ba <sup>2+</sup> isonuclear sequence using the DLP technique	20
1 6	Photoabsorption spectra of a lanthanum plasma under different experimental conditions	22
1 7	Photoabsorption spectra of a cerium plasma under different experimental conditions	23
1 8	Time resolved photoabsorption study of a europium plasma	24
1 9	Photoabsorption study of a EuI in comparison with the total photon yield	26
1 10	Photoabsorption study of a gold plasma in the 40-110eV energy region under different experimental conditions	27
2 1	4 <i>f</i> ( <sup>1</sup> <i>P</i> ) orbital of La <sup>3+</sup> in a frozen core and fully relaxed calculation	34
2 2	Schematic drawing of the development of an energy-level structure of the 4 <i>d</i> <sup>9</sup> 4 <i>f</i> and 4 <i>d</i> <sup>9</sup> 8 <i>f</i> configurations of La <sup>3+</sup>	47
2 3	Photoabsorption cross section of Ba 4 <i>d</i> → <i>εf</i> ( <sup>1</sup> <i>P</i> ) with use of relaxed and frozen core orbitals	55

2 4	Fano profiles for different q values	59
2 5	Beutler-Fano photoabsorption profile for the $1s^2(^1S_0) \rightarrow 2s2p(^1P_1)$ double excitation in $Li^+$	61
3 1	Plot of the configuration average (CA)HF 4f and the LS term dependent $4f(^1P)$ local single electron potentials and radial wavefunctions for the $4d^94f$ configuration in Ba	73
3 2	Photoabsorption spectrum of Xe	75
3 3	Photoabsorption spectra of Ba, La, Ce, Sm and Eu	76
3 4	Photoabsorption spectrum of $La^{3+}$	79
3 5	LS term dependence for the $4f(^1P)$ of $La^{3+}$	83
3 6	Calculated photoabsorption spectrum in the 4d excitation region for $La^{3+}$ with the CI-HF method	87
3 7	Photoabsorption spectrum in the 4d excitation region of $La^{3+}$ calculated with the MBPT/RPAE method	89
3 8	Photoabsorption cross sections in the 4d excitation region of $La^{3+}$ calculated with the TDLDA method	93
3 9	Photoabsorption cross sections in the 4d excitation region of $Ba^{2+}$ and $La^{3+}$ calculated with the relativistic (R)TDLDA method	94
3 10	Photoabsorption spectra of $Ba^{2+}$ and $La^{3+}$	96
3 11	$4f(^1P)$ radial wavefunctions and their appropriate effective local potentials for $Ba^{2+}$ , $La^{3+}$ and $Ce^{4+}$	98
3 12	Absorption spectrum of $La^{3+}$ in comparison with La metal, solid $LaF_3$ and solid $LaCl_3$	99
4 1	Relative absorption cross sections of Au vapour in the $4f \rightarrow 5d$ excitation region taken at different time delays	105
4 2	Relative absorption cross section of Au vapour in the 5p and 4f excitation region	107
4 3	Photoabsorption in the $5p \rightarrow 5d$ and $4f \rightarrow 5d$ excitation region	110

4 4	Calculated photoabsorption spectra of Au within the (R)HF and RTDLDA theory for the ground and valence excited state	111
4 5	Measured relative photoabsorption cross section of a gold vapour in comparison with calculated absolute cross sections within the RLDA, the RTDLDA and the (R)HF theory	114



# List of Tables

2 1	Configuration average energies $E_{av}$ and Slater integrals $F^k$ and $G^k$ of $\text{La}^{3+}$	39
2 2	Angular coefficients $f^k$ and $g^k$ of the d-f and d-p direct and exchange contributions of the energies $E_{Coul}^{ij}$ for the terms $^1P_1$ , $^3P_1$ and $^3D_1$	40
2 3	Calculated Coulomb energies $E_{Coul}^{ij}$ for the terms $^1P_1$ , $^3P_1$ and $^3D_1$ of the $4d^94f$ and $4d^98f$ configurations in $\text{La}^{3+}$	41
2 4	Calculated spin-orbit radial integrals for the $4d^9nf, mp$ configurations of $\text{La}^{3+}$	43
2 5	Spin-orbit energies for the $4d^94f$ states with $J = 1$ of $\text{La}^{3+}$ calculated in the jj coupling scheme	43
2 6	Spin-orbit energies for the $4d^94f$ and $4d^98f$ states with $J = 1$ of $\text{La}^{3+}$ calculated in the LS coupling scheme	44
2 7	Mixing coefficients for the $4d^94f$ and $4d^98f$ states of $\text{La}^{3+}$ in the intermediate coupling scheme	46
2 8	Energy integrals for the $4d^9nf - 4d^9mf$ interconfiguration Coulomb interactions in $\text{La}^{3+}$	50
2 9	Calculated energy values for the $4d^94f(^1P) - 4d^9mf(^1P)$ interconfiguration Coulomb interactions in $\text{La}^{3+}$	51
2.10	Fine structure components of the $4d^94f$ configuration	54
2 11	Fano parameters of the $1s^2(^1S_0) \rightarrow 2s2p(^1P_1)$ resonance line in $\text{Li}^+$	62

3 1	Hartree-Fock parameters for the $4d^9 4f^1 5s^2 5p^6 ({}^1P_1)$ term in $\text{La}^{3+}$	81
3 2	Calculated single configuration (SC) ( <i>ab initio</i> ) and configuration interaction Hartree-Fock (CI-HF) energies	85
3 3	Excitation energies, widths and oscillator strengths for the dipole transitions from the 4d shell in ground state $\text{La}^{3+}$ calculated with the MBPT/RPAE method	90
4 1	Transition lines from states belonging to the $5d^{10}6s^1$ and $5d^9 6s^2$ configurations of neutral gold	108

# Introduction

Giant resonances have been the subject of many theoretical and experimental investigations in atomic, molecular and solid state physics (Connerade et al 1987). Their appearance as strong, broad and asymmetric resonance profiles arises from their multiparticle nature, which is of general interest in the study of many body effects. Very recently a giant plasmon resonance in fullerene  $C_{60}$  has been measured (Hertel et al 1992), where many body calculations utilizing the random phase approximation (RPA) predicted a resonance with tremendous oscillator strength (Bertsch et al 1991).

Atoms are particularly well suited for studying many body theories because of their relatively simple structure and because the electromagnetic interaction between the constituents of the many particle system is well known. A prominent example is the 4d giant dipole resonance in Ba, La and the lanthanides which has been extensively discussed within different many body theories (Wendin 1973, Wendin 1984, Amusia & Sheftel 1976, Zangwill & Soven 1980, Pan et al 1987, Zangwill 1987, Amusia et al 1989b). Recent experimental studies of the decay channels of atomic Ba (Baier et al 1994) in the 4d giant resonance energy region using a new developed technique, the so called photoelectron-ion coincidence spectroscopy, permitted the measurement of the decay probabilities from different  $Ba^+$  inner hole states to higher charged  $Ba^{2+}$ ,  $Ba^{3+}$  and  $Ba^{4+}$  ions and provided a direct link between photoelectron and photoion spectroscopy. The partial photoion yields of atomic La in the 4d excitation region has been measured by Dzionk et al (1989), which complement the measured photoelectron

data of atomic La in the same energy region by Richter et al (1988) Sairanen et al (1991) measured the resonant Auger and autoionization processes in solid La after  $4d \rightarrow 4f$  excitation using electron spectroscopy and a very recent study of resonant electron emission of atomic Eu and Sm around the 4d giant resonance by Kukk et al (1994) displays the continuing interest in this topic. Theorists have also focused on the 4d inner-shell photoexcitation of neutral, singly or multiply ionized atoms along the Ba (Nuroh et al 1982) and La isonuclear (Amusia et al 1989a) sequence and the Xe isoelectronic (Cheng & Froese Fischer 1983, Cheng & Johnson 1983) sequence in order to gain further insight into fundamental aspects such as electron-correlation effects, centrifugal barrier effects and orbital collapse in term dependent Hartree-Fock potentials

However, very little is known experimentally on photoexcitation processes for ionic species due to the severe experimental difficulties inherent in production of a sufficiently dense ion column. Only very few cross section measurements for ions are available to date for comparison with theory. Absolute cross sections for  $K^+$ ,  $Ca^+$ ,  $Sr^+$  and  $Ba^+$  ions were measured by Lyon et al (1986,1987), the Cr,  $Cr^+$ , Mn and  $Mn^+$  sequences were studied by Cooper et al (1989) and Costello et al (1991). The classic experimental results for Ba,  $Ba^+$  and  $Ba^{2+}$  by Lucatorto et al (1981) remain the only existing data for an extended isonuclear sequence in the giant resonance energy region. A dramatic change in the photoabsorption behaviour in moving along the isonuclear sequence between  $Ba^+$  and  $Ba^{2+}$  was observed. This led to considerable discussion in the literature (see Connerade et al 1987 and contributions therein). Further calculations for ions in the Xe isoelectronic sequence (Cheng & Froese Fischer 1983, Cheng & Johnson 1983) predicted that in moving from  $Ba^{2+}$  to its isoelectronic partner  $La^{3+}$  the gradual orbital collapse in the  $^1P$  channel should lead to the  $4d^9 4f(^1P)$  resonance becoming the dominant photoabsorption feature. In order to test their prediction the Xe isoelectronic sequence was extended beyond  $Ba^{2+}$  to  $La^{3+}$  with use of the Dual Laser Plasma (DLP) technique (Hansen et al 1989). While the photograph-

ically recorded photoabsorption spectrum showed absorption lines successfully assigned to  $\text{La}^{3+}$  the  $4d^9 4f(1P)$  resonance was *not* observed. Further insight into the orbital collapse phenomenon was provided, in that calculations (Hansen et al 1989) showed that the increase of oscillator strength occurs concomitantly with a strong broadening of the resonance line, this makes it difficult to observe its feature in a photographic based experiment. A very recent calculation for the  $4d \rightarrow 4f$  transition for  $\text{Ce}^{4+}$  by Ivanov (1992) supports this contention.

In this work, the Dual Laser Plasma technique has been employed in order to study the time and space resolved photoabsorption behaviour of laser generated Ba, La, Ce, Eu and Au plasmas. For the first time photoelectric based photoabsorption cross section data for  $\text{Ba}^+$ ,  $\text{Ba}^{2+}$  and  $\text{La}^{3+}$  are provided, which enables a critical comparison between experimental results and predictions based on LS-term dependent Hartree-Fock and (R)TDLDA, RPAE/MBPT many-body theories.

Remarkably the 4p and 5p excitation spectra of the 4d and 5d transition metals in atomic form have been the subject of only a few investigations when compared with the abundance of experimental and theoretical work on the 3p *giant resonance* in the 3d transition metals (Sonntag & Zimmermann 1992). Therefore a detailed photoabsorption study of atomic gold ( $Z = 79$ ) in the corresponding inner-shell excitation region was undertaken in this work. Gold is the last member of the 5d transition metal series and together with copper ( $Z = 29$ ) and silver ( $Z = 47$ ) are often termed the noble metals. The simple term structure of atomic gold in the ground ( $5d^{10}6s^1$ ) and valence excited states ( $5d^9 6s^2$ ), with only one vacancy in the electron configuration in the  $5p \rightarrow 5d$  and  $4f \rightarrow 5d$  excitation energy region, makes gold an ideal representative of the heavier elements for the study of electron correlations effects within (R)HF and RTDLDA theories.

# Chapter 1

## Time and Space Resolved XUV Photoabsorption Experiment on Laser Produced Plasmas

The purpose of this chapter is to provide an overview of the experimental approach which was taken in this work and to show how the time and space resolved XUV photoabsorption spectra of the Ba, La, Ce, Eu and Au plasmas were obtained. In subsequent chapters selected experimental results for  $\text{La}^{3+}$  and Au are discussed in detail and additional experimental information is provided when applicable.

### 1.1 Experiment

The photoabsorption data were recorded with use of the Dual Laser Plasma (DLP) technique which is illustrated schematically in Figure 1.1. The backlighting XUV source was a plasma produced by a flashlamp pumped Nd YAG laser (Spectron Laser Systems) with an output of 1J and 10ns pulse width focussed onto a tungsten target. It has been shown in a previous study by Carroll et al (1980), that with use of appropriate targets, such laser produced plasmas pro-

vide essentially line free continua which have the temporal characteristics of the exciting laser pulse, suitable for time resolved photoabsorption spectroscopy on dynamic systems in the XUV energy region. The continuum radiation passed through the absorbing medium produced by a second flashlamp pumped ruby laser (System 2000 J K Lasers) with an output of 1J in 30ns, or alternatively by a flashlamp pumped dye laser (SLL-500 Candela Laser Corp) with an output of about 2J and 0.8 $\mu$ s pulse width focussed onto suitable targets for creating the absorption column. The radiation transmitted through the absorption medium was collected by a toroidal mirror and imaged on the entrance slit (20 $\mu$ m) of a 2.2 grazing incidence spectrometer (McPherson 247) conformed to a Rowland circle mounting for concave gratings. The spectrometer was equipped with a 1200g/mm gold coated Bausch and Lomb ruled grating with a blaze angle of 1°47', which diffracted the light off all wavelengths and focussed it horizontally on the circumferences of a circle with a diameter R (Rowland circle) equal to the radius of the grating. Spectral detection was via a MgF<sub>2</sub> coated MCP (Galileo Electro Optics Corp) mounted on the Rowland circle and which was coupled via a fiber optic reducer to a self scanning photodiode array (Reticon 1024S). The MCP as the photosensitive element was operated with a positive voltage of about 800V which amplified the photoelectrons by a factor of  $\sim 10^4$ . The electrons ejected from the MCP were accelerated by a potential difference of +4.2kV onto a (P-20) phosphor screen coated onto a fiber optic bundle which converted the electrical signal into visible photons and transferred them onto the photodiode array (PDA) which had 1024 pixels with a spatial resolution of 25 $\mu$ m. The use of the fiber optic bundle matched the MCP length to that of the PDA allowing a larger simultaneous spectral coverage with only a small reduction in the spatial resolution. The PDA was controlled by an optical multichannel analyser (OMA) supplied by EG&G Princeton Applied Research Corp which digitized and stored the video output from the PDA after each laser shot.

The combination MCP, fiber optic reducer and PDA resulted in a detection

## experimental setup

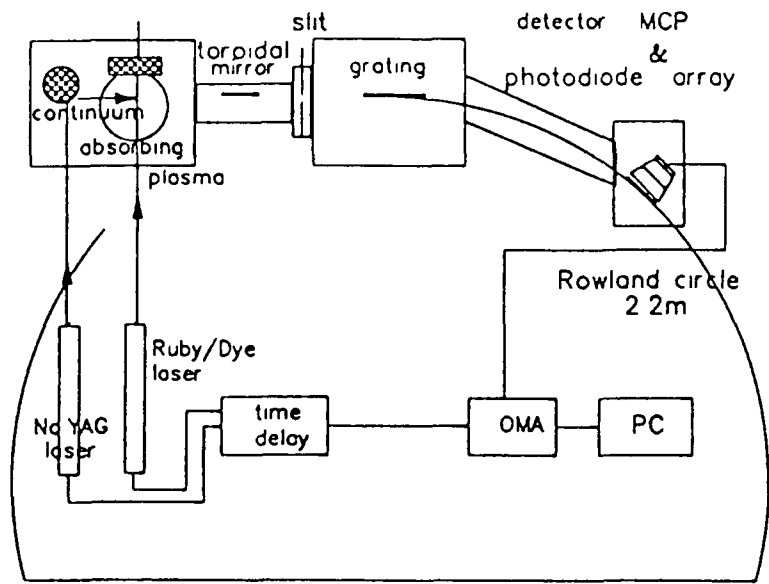


Figure 1 1 *Experimental setup of the DLP- facility*

system with high resolution and sensitivity (single shot sensitivity), with linear response and good dynamic range for XUV observations. Similar systems are described in detail by Cromer et al (1985) and Schwob et al (1987)

The energy range which could be covered per MCP setting varies along the Rowland circle from about 3eV at 30eV to 40eV at 120eV. Therefore the resolution of the system depends on the position of the MCP along the Rowland circle.

The instrument was operated with a pressure  $< 4 * 10^{-7}$  mbar in the MCP chamber,  $< 2 * 10^{-6}$  mbar in the toroidal mirror chamber and between  $10^{-4} - 10^{-5}$  mbar in the target chamber.

The two lasers were synchronized electronically and allowed a variable inter laser time delay. The absorption target was movable with respect to the optical axis and the focus of the laser pulse onto the target could be varied via an appropriate lens which allowed the core of the plasma to be moved in and out of the optical axis. By varying the irradiance conditions on the absorber target, its position relative to the optical axis and the inter laser time delay, time and space



resolved photoabsorption spectroscopy of the absorbing medium was achieved. A schematic diagram of the experimental parameters is given in Figure 1.2. Since in an expanding plasma plume, the ions with higher charge move faster away from the target than those with lower charge, the separation of the different ion stages in space and time can be achieved with use of the DLP technique.

The instrument used in this work enabled the measurement of relative photoabsorption cross sections of a wide range of atoms and ions. The absorption coefficient  $k$  is given as a function of the photon energy by the well known relation

$$I(E) = I_0(E)e^{-k(E)} \quad (1.1)$$

where  $I$  is the transmitted intensity and  $I_0$  the incident intensity. In practice  $I_0$  is observed without, while  $I$  with the absorbing medium which yields to an absorption coefficient which can be determined through

$$k(E) = \ln \left( \frac{I_0(E)}{I(E)} \right) \quad (1.2)$$

Usually  $I_0$  and  $I$  should be corrected for contributions due to stray light  $I_{s0}$  and  $I_s$  respectively and the emission  $I_e$  from the absorption plasma which results in a more complicated relation between absorption coefficient  $k$  and the measured intensities (Jannitti et al 1987), but a detailed study of the performance and capability of the system by Kiernan (1994) showed that these contributions are negligible and the relative cross sections can be obtained through eqn (1.2).

The absorption coefficient is proportional to the photoionization cross section  $\sigma(E)$  which is the characteristic quantity for the specific absorption medium with

$$k(E) = \sigma(E) \int_l n(E, y) dy \quad (1.3)$$

$n(E, y)$  is the density of atoms/ions along the optical axis which are able to absorb photons of the energy  $E$ . Since the density was unknown in the DLP experiments, the information which could be obtained was restricted to the relative magnitude of the photoabsorption behaviour.

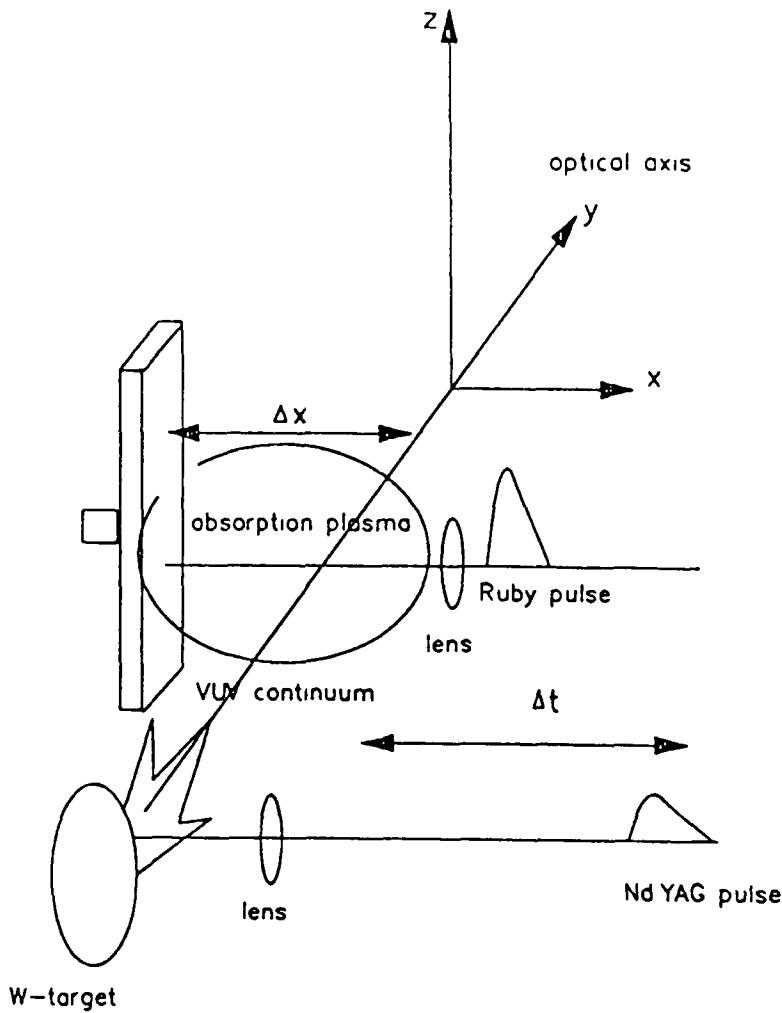


Figure 1 2 Schematic illustration of the DLP technique, with various experimental parameters  $\Delta x$  and  $\Delta t$  used to perform time and space resolved spectroscopy of the absorption plasma. The XUV source used here was a plasma produced by Nd YAG laser pulse focussed on a W-target. The continuum radiation passed through the absorbing plasma which was produced by a second synchronized ruby or dye laser pulse focussed onto a suitable absorption target. The absorbing ion stage could be chosen by varying the irradiance conditions on the absorption target, its relative position to the optical axis  $\Delta x$  and the inter laser time delay  $\Delta t$  between the two laser pulses.

Figure 1.3 shows three typical PDA spectra recorded at the MCP setting of 16.5 mch which were used in order to obtain the absorption coefficient  $k(E)$  of  $\text{La}^{3+}$ . The upper two spectra present the W emission spectrum without ( $I_0$ ) and with ( $I$ ) the absorbing La plasma. The natural logarithm of the ratio  $I_0/I$  yielded to the photoabsorption data of Figure 1.6 (lowest spectrum) after energy calibration was achieved by recording emission lines of an aluminium plasma (Figure 1.3 lowest spectrum) as a reference spectrum (Kelly 1987). Although the instrument is sensitive enough to measure single laser shot photoabsorption spectra, 15-25 shots were typically accumulated for each spectral range in order to improve the signal to noise ratio. The shot to shot reproducibility was assessed by recording simultaneously the laser pulses and the single shot photoabsorption spectrum on high speed HP-54502A oscilloscopes in order to check the jitter in the inter laser time delay, the laser pulse signals and the consistency in the photoabsorption signal using the same experimental parameters. When operating the laser system under extreme conditions (very short time delay between the laser pulses and using high voltages for the Pockels cell of the ruby laser), every single shot event was assessed before accumulated to the previous spectra. After about 20 laser shots, the alignment of the backlighting plasma along the optical axis was checked and if necessary optimized in order to obtain maximum photon intensity on the detector.

The major difficulty of the experiments was to find the right experimental parameters to obtain cross section data of the absorbing medium in a pure atomic or ionic state. Therefore a detailed experimental investigation of the absorption behaviour under various experimental conditions had to be carried out. Photoabsorption cross section data which were already known could be very easily reproduced and the optimization of the experimental parameters were usually straight forward as shown later for the Ba,  $\text{Ba}^+$  and  $\text{Ba}^{2+}$  isonuclear sequence or the Ba, La, Ce, Sm and Eu sequence. In order to obtain new cross section data, an extensive theoretical study was carried out in conjunction with the ex-

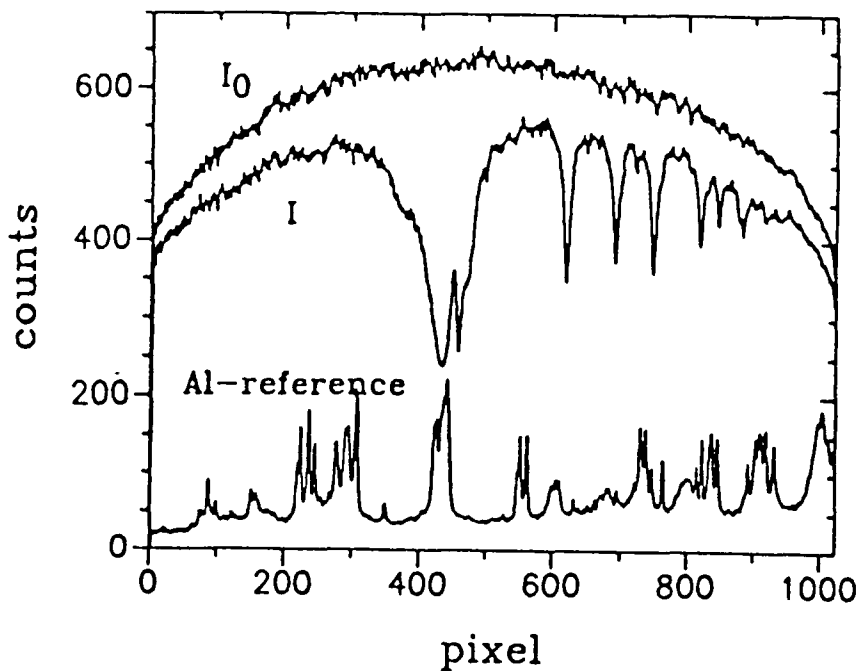


Figure 1.3 PDA spectra at 16.5 inch of a W emission spectrum without ( $I_0$ ) and with ( $I$ ) an absorbing La plasma. For energy calibration purposes an aluminium emission spectrum was recorded at the same MCP setting.

perimental work. The theoretical and experimental investigations complemented one another in an iterative way in order to produce the new data, particularly of  $\text{La}^{3+}$  and gold, presented in this work.

## 1.2 Time and Space Resolved Photoabsorption Spectra of Laser Produced Plasmas

The following paragraphs describe briefly the experimental investigations of the laser produced Ba, La, Ce, Eu and Au plasmas.

### Isolation of Ba, $\text{Ba}^+$ and $\text{Ba}^{2+}$ : Comparison with previous results

The capability of the DLP-system was assessed by recording the Ba,  $\text{Ba}^+$  and  $\text{Ba}^{2+}$  isonuclear sequence, which was measured previously by Lucatorto et al. (1981) using a heat pipe and the Resonant Laser Driven Ionization (RLDI) tech-

nique with photographic detection (see Figure 1.4)

In the RLDI technique, the  $\text{Ba}^+$  ions were produced by tuning a dye laser pulse into the  $6s^2(^1S) \rightarrow 6s^16p^1(^1P)$  resonance line of Ba vapour atoms. Ionisation of the laser excited Ba atoms occurred mainly via multiphoton absorption or collisional processes with other excited Ba atoms, until the electron temperature was hot enough, so that the Ba atoms in ground and excited state were ionized via electron impact (Lucatorto & McIlrath 1980). The  $\text{Ba}^{2+}$  ions were produced by tuning a second pulsed dye laser into the  $6s^1(^2S) \rightarrow 6p^1(^2P)$  resonance of  $\text{Ba}^+$ . The XUV source in the RLDI experiment was an uranium anode spark, which was synchronized with the laser pulses. The DLP results are presented in Figure 1.5. Good agreement in general with the RLDI data is obtained for  $\text{Ba}^{2+}$ , whereas the shape of our  $\text{Ba}^+$  appears slightly different and resembles more that of neutral Ba. Recent measurements of the total photoion yield of  $\text{Ba}^+$  ions (Kravis et al 1993) showed excellent agreement with the DLP photoabsorption data.

All three spectra were recorded using the ruby laser for the production of the Ba absorption plasma. In the case of the Ba spectrum, a lens with a point focus was used, the laser pulse was strongly defocussed onto the Ba-target in order to create as many as possible free Ba atoms through ablation instead of through recombination processes of ions. The distance of the Ba-target to the optical axis was 0.5mm and a  $3\mu\text{s}$  time delay was chosen. The  $\text{Ba}^+$  spectrum was obtained by using a cylindrical lens tightly focussed onto the Ba-target in order to produce many Ba ions. With a distance  $\Delta x$  of 0.2mm and a time delay  $\Delta t = 500\text{ns}$ , the higher charged ions were already expelled far away from the target and the slower  $\text{Ba}^+$  ions just passed the optical axis. The  $\text{Ba}^{2+}$  spectrum was recorded by increasing the distance to the optical axis  $\Delta x$  to 3mm and shortening the time delay  $\Delta t$  at the same time down to 250ns.

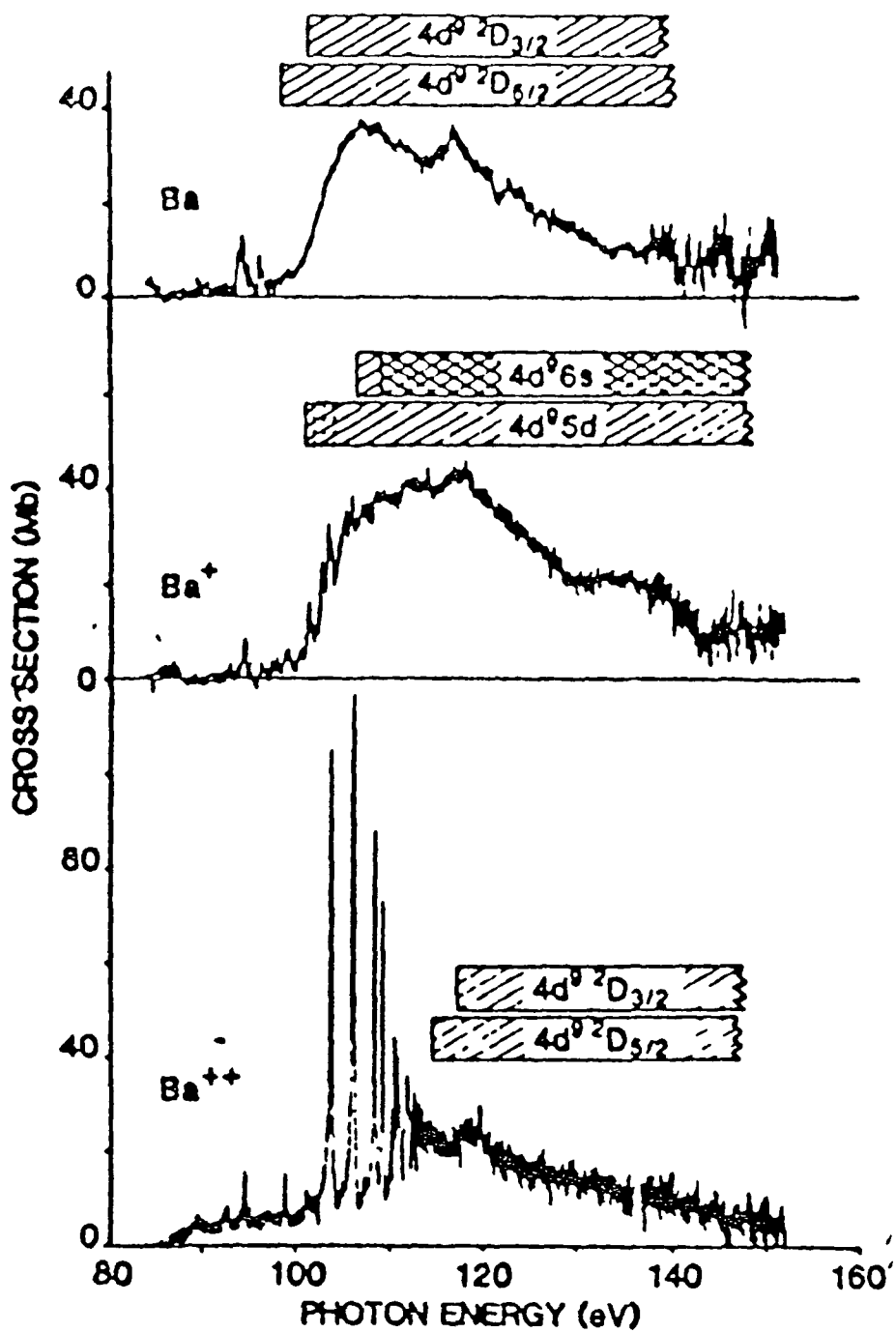


Figure 14 Photoabsorption of the Ba, Ba<sup>+</sup> and Ba<sup>2+</sup> isonuclear sequence using the RLDI technique (Lucatorto et al 1981)

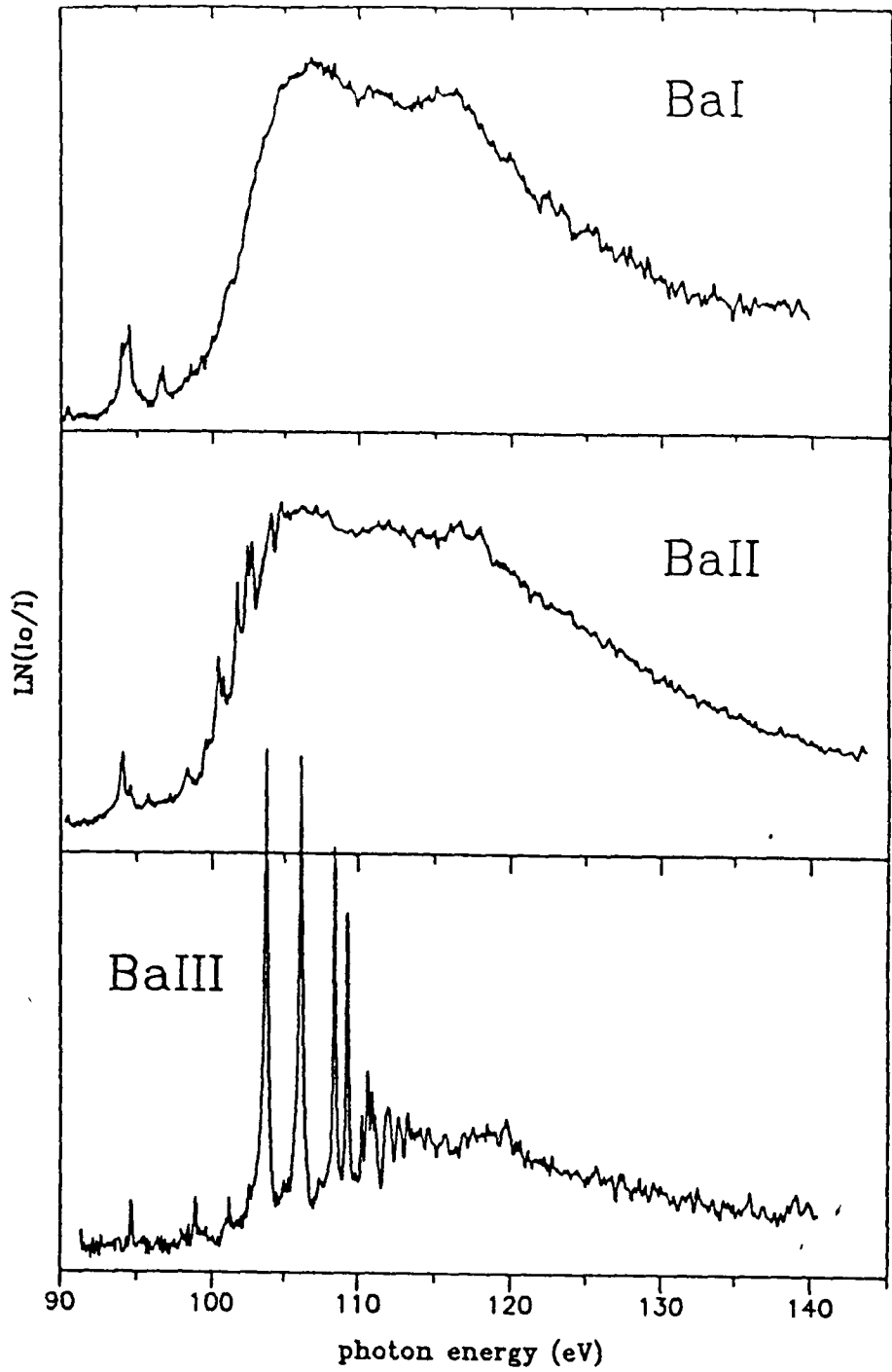


Figure 15. Photoabsorption of the Ba, Ba<sup>+</sup> and Ba<sup>2+</sup> isonuclear sequence using the DLP technique

## Time and space resolved measurements for La ions

Since the DLP technique successfully reproduced the Ba isonuclear sequence, much effort was made in this work to extend the Xe-isoelectronic sequence beyond  $\text{Ba}^{2+}$  to  $\text{La}^{3+}$ . Figure 1.6 shows the photoabsorption study of a lanthanum plasma in time and space. At first, the experimental parameters were optimized in order to obtain the well known  $4d \rightarrow \epsilon f$  giant resonance of neutral lanthanum. Similar to the experience gained in the barium experiment, the photoabsorption spectrum of LaI could be recorded by choosing  $\Delta x = 0.5\text{mm}$ , close to the target surface and a relatively long time delay  $\Delta t = 720\text{ns}$ . A successive study of the photoabsorption behaviour by shortening the time delay to  $60\text{ns}$  gave rise to discrete line structure with a reduction in the continuum background. A very nice  $\text{La}^{3+}$  spectrum was obtained by increasing  $\Delta x$  to  $1\text{mm}$ . A more complete treatment is reserved for Chapter 3.

## Time and space resolved measurements for Ce ions

Figure 1.7 shows a sequence of photoabsorption data of a cerium plasma under different experimental conditions. The spectrum on the top shows the  $4d$  giant resonance of neutral cerium. By shortening the time delay, the spectra are dominated by two strong and broad peaks at  $122\text{eV}$  and  $126\text{eV}$  which are also observable in the  $\text{CeF}_3$  photoabsorption spectrum by Olsen et al (1982). This may lead to the conclusion, that its origin is triple ionized cerium. With further decrease in the time delay down to  $70\text{ns}$ , the spectrum shows one very strong resonance line at  $127\text{eV}$  which may be attributed to the  $4d \rightarrow 4f(^1P)$  transition of  $\text{Ce}^{4+}$ . However a successful study of the  $\text{Ce}^{4+}$  photoabsorption spectrum was not possible due to the limited capability of the laser system operated with a very high Pockels cell voltage and extremely short time delays. The jitter of the ruby laser pulse and its shot to shot instability prevented the production of a substantial amount of  $\text{Ce}^{4+}$  ions separated from the other ion stages in space and



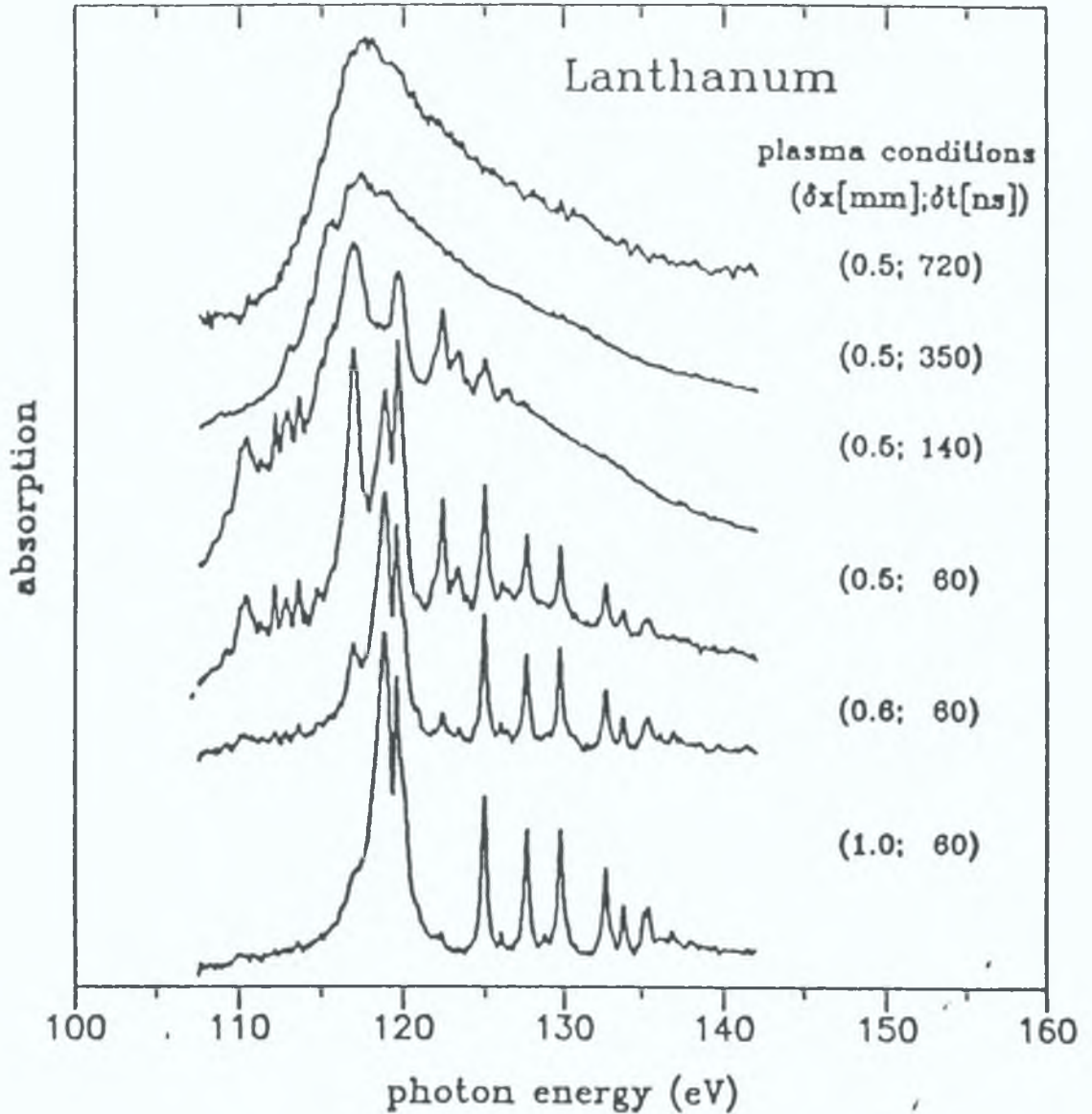


Figure 1.6: Photoabsorption spectra of a lanthanum plasma under different experimental conditions  $\Delta x$  and  $\Delta t$ . The absorption spectrum for neutral lanthanum was obtained by passing the continuum radiation near the La-target surface through the absorbing plasma ( $\Delta x = 0.5\text{mm}$ ) in combination with a long inter laser time delay ( $\Delta t = 720\text{ns}$ ). The  $\text{La}^{3+}$  spectrum was obtained by increasing the distance between La-target and optical axis ( $\Delta x = 1\text{mm}$ ) and shortening the time delay between the two laser pulses ( $\Delta t = 60\text{ns}$ ).

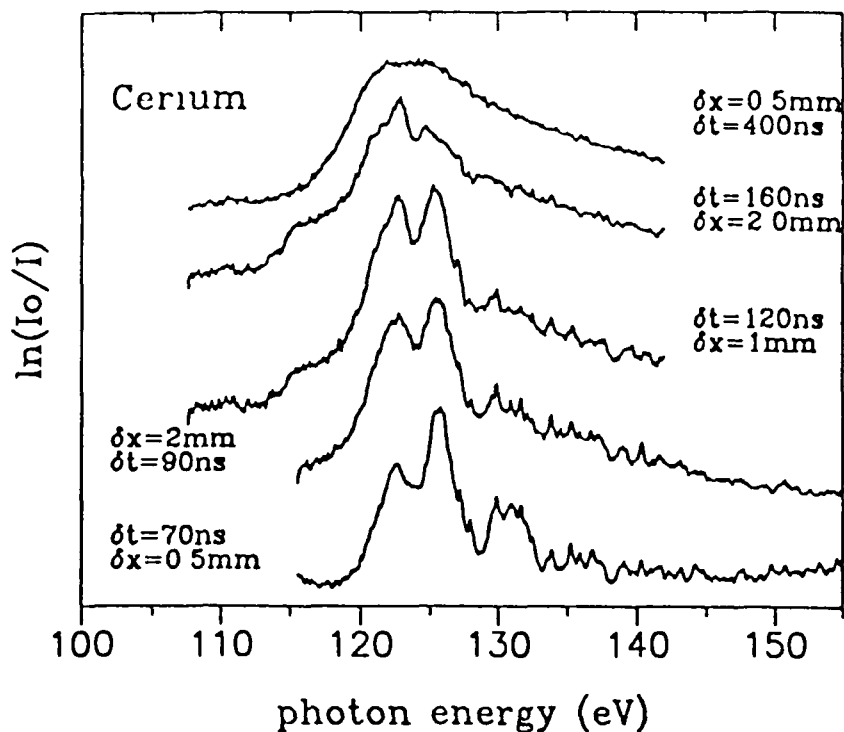


Figure 1.7 Photoabsorption spectra of a cerium plasma under different experimental conditions  $\Delta x$  and  $\Delta t$

time

### Time and space resolved measurements for Eu ions

The  $4d \rightarrow 4f$  giant resonance in europium has been studied with great interest over the last recent years (Amusia et al 1989b, Pan et al 1987, Zangwill 1987, Becker et al 1986, Nagata et al 1990). Europium is special among the lanthanides because of its half filled  $4f$  subshell, which makes it more accessible for theoretical calculations since the  $4f$  subshell can be considered as a closed subshell with all  $4f$  electrons having the same spin projection forming a ground state with the highest possible absolute spin value ( ${}^8S_{1/2}$ ). Therefore all seven  $4f$  electrons behave like spectators in the  $4d \rightarrow 4f$  excitation process, which drastically reduces the coupling possibilities among the  $4f^8$  electrons.

The photoabsorption behaviour of the europium plasma was studied in detail in this work. It was of particular interest to investigate the change in the cross section data by opening the  $6s$  and the (half filled)  $4f$  subshell. Figure 1.8

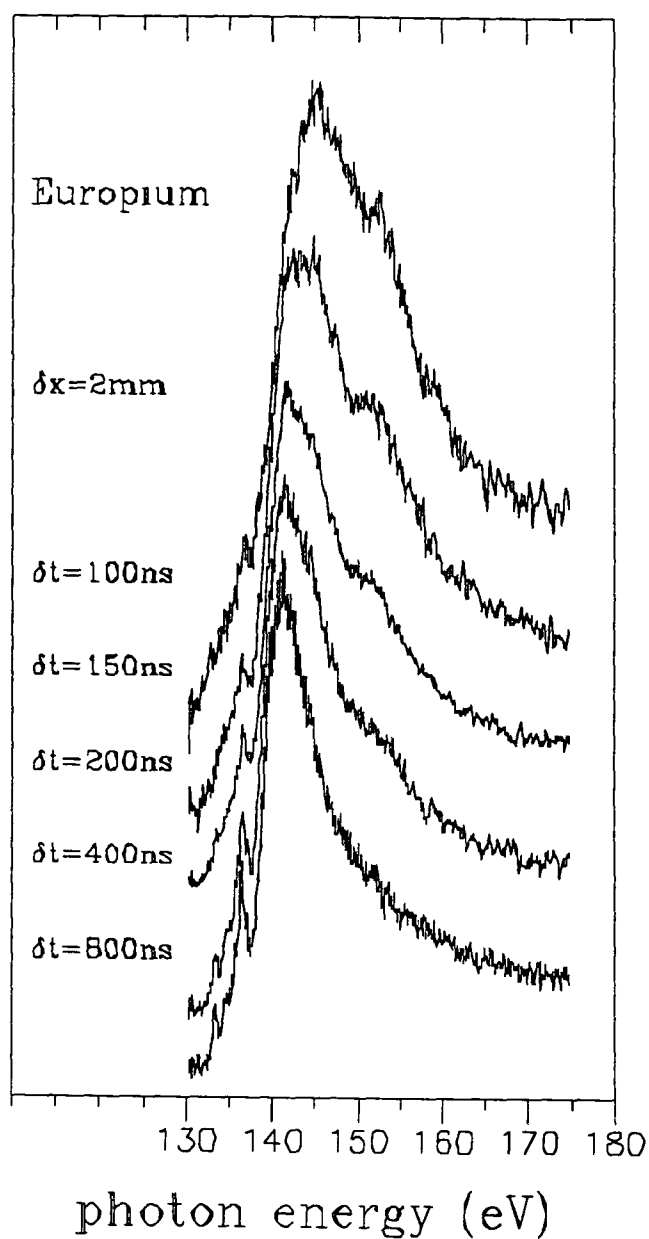
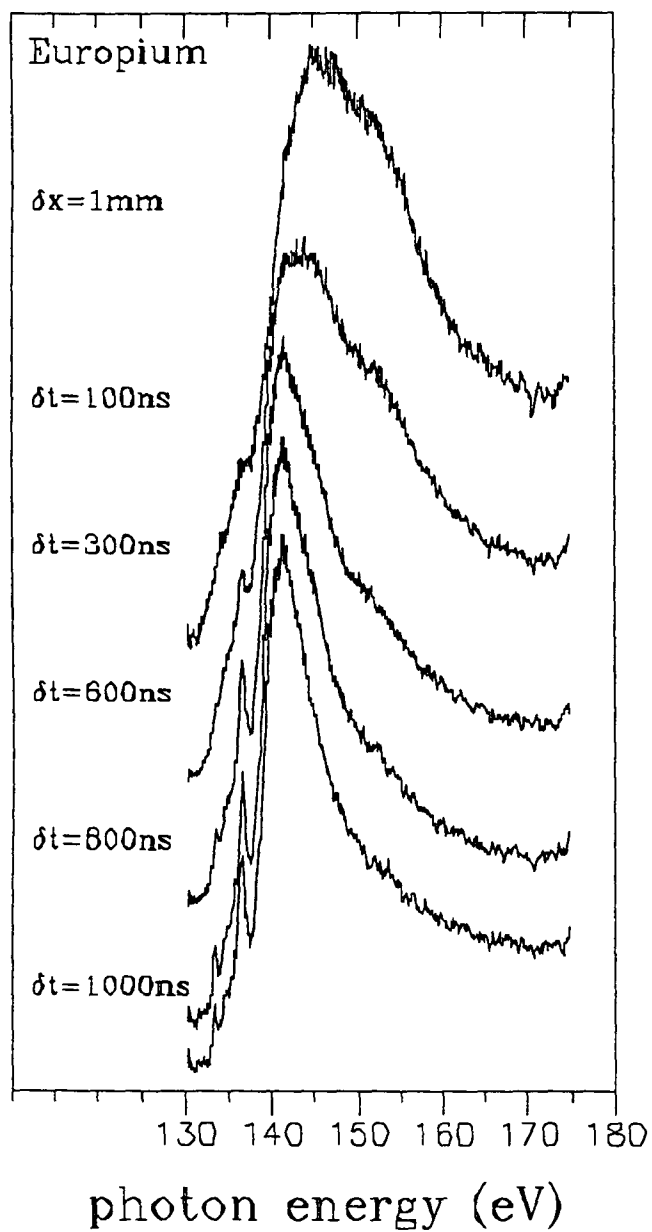


Figure 18 Time resolved photoabsorption study of a europium plasma with different target positions  $\Delta x$

shows two time resolved photoabsorption sequences at different target positions. In both cases, the photoabsorption spectra were optimized on neutral europium which is well known (Mansfield & Connerade 1976). Then, the time delay was successively shortened in order to catch the ion species. All three sequences show consistently a broadening in the absorption feature towards higher photon energy and a second peak at 153eV when decreasing the time delay. This may be understood in comparison with the lanthanum results, where with increasing ionization degree additional rydberg lines appeared on the high energy side of the spectrum. In europium, where the term structure is much more complex, the resonances overlap and appear as a single broad feature.

Figure 1.9 shows the spectra of EuI produced with the ruby laser and in a second experiment with use of the dye laser. Both spectra are virtually identical. Additionally the total photoion yield of Eu is shown (Koble 1991) for comparison with the DLP-data. The disagreement on the high energy side may be explained due to a systematic error in detecting the photoions with use of the TOF spectrometer.

## **Time and space resolved measurements for gold**

Figure 2.0 shows the photoabsorption spectra of a gold plasma for three different experimental conditions. In order to cover the energy range from 40 to 110eV seventeen separate MCP positions were necessary. The spectra of each MCP setting, which overlapped with the successive one, were matched together in order to obtain the overall cross sections shown in Figure 1.10. By moving the detector along the Rowland circle, several cross checks were carried out in the  $4f$  excitation region in order to insure, that the plasma conditions remained the same over the whole energy range.

The first spectrum on top with  $\Delta x = 1\text{mm}$  and  $\Delta t = 600\text{ns}$  represents photoabsorption from AuI which is discussed in detail in Chapter 4. By shortening

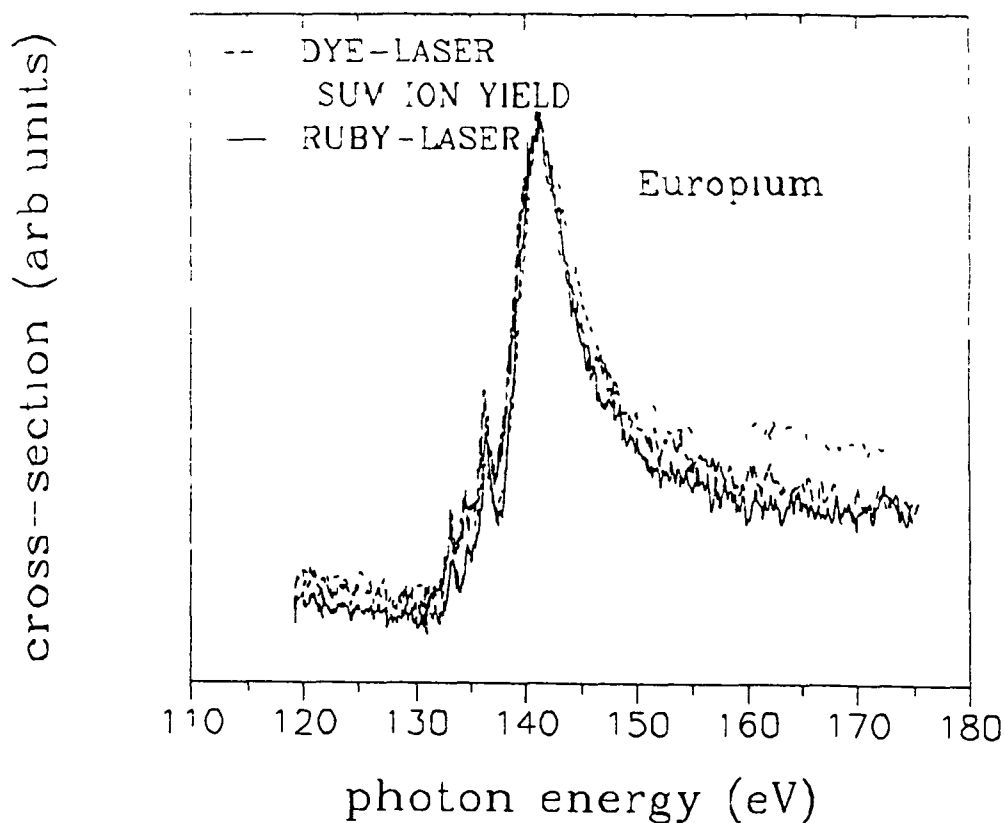


Figure 19 *Photoabsorption study of a Eul in comparison with the total photoion yield*

the time delay to 100ns, absorption from ionized gold was obtained, since the pronounced sharp peak at 80eV has almost disappeared. The structure between 80 and 90eV resembles very much that of Pt (Costello et al 1991) in the  $4f \rightarrow 5d$  excitation region which indicates, that the spectrum shows absorption predominantly of  $Au^+$

A further decrease in the time delay shows photoabsorption of higher ionized Au with a complex rydberg line structure in the energy region between 50 and 65eV

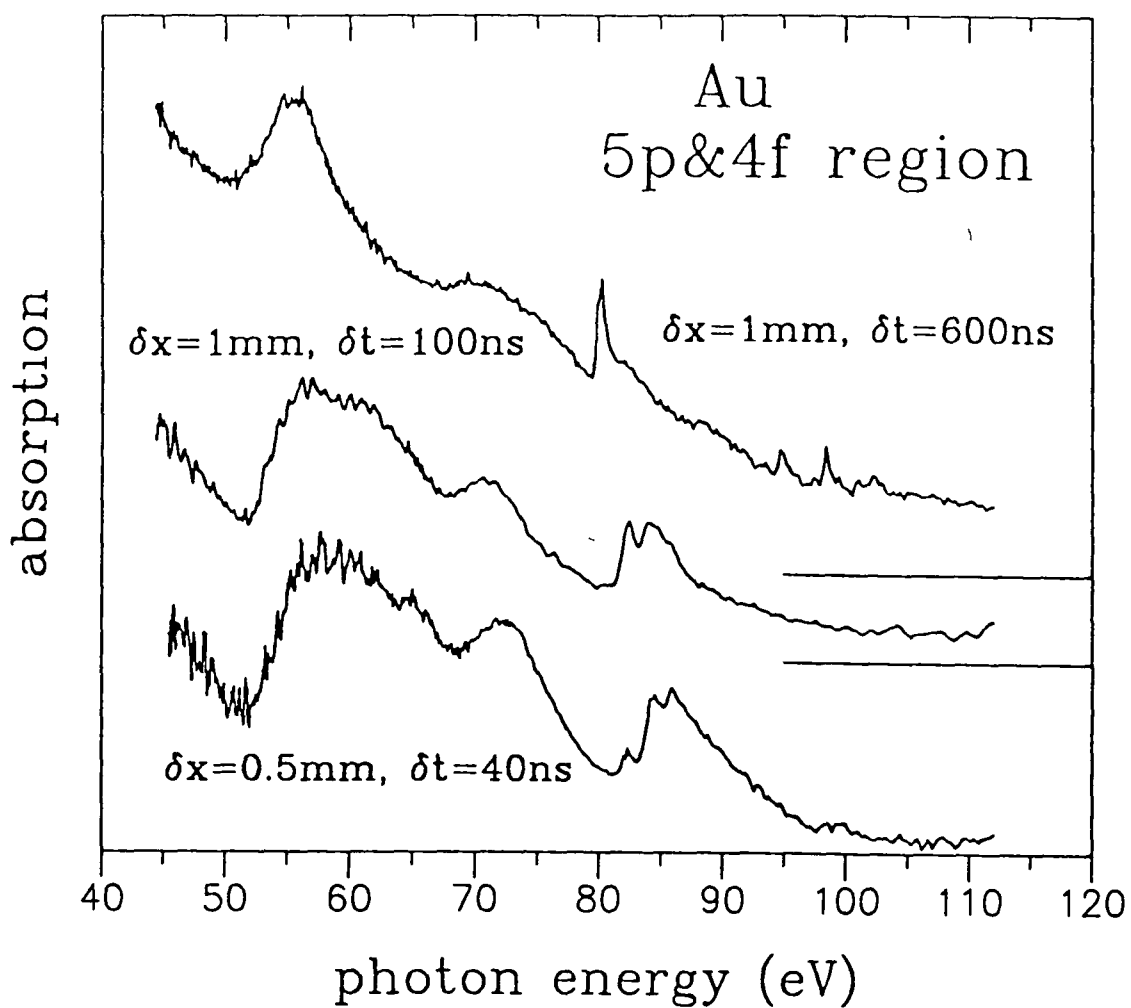


Figure 1 10 *Photoabsorption study of a gold plasma in the 40-110eV energy region under different experimental conditions*

## Chapter 2

# The *ab initio* Theory of Atomic Structure

The following chapter introduces the basic theoretical models and their approaches, which are required for the description of the experimental photoabsorption spectra presented in this work. The discussion is based mainly on the lectures *Rechenmethoden in der Atomphysik* by Peter Zimmermann (Zimmermann 1976) which he gave at the Technical University of Berlin in the year 1989. Secondly I have to mention here explicitly the classic book *The Theory of Atomic Structure and Spectra* by R. D. Cowan (Cowan 1981) which gives the complete theory behind the atomic structure calculation codes *RCN/RCN2/RCC* which were used extensively in this work in order to analyse and model the measured photoabsorption spectra.

Most of the calculational steps are illustrated by some selected intermediate key results, mainly for the  $\text{La}^{3+}$  spectrum, since the complete representation of all atomic parameters would be too voluminous and of no great use for physical insight of the atomic absorption data.

The first section deals with the *independent particle model* in atomic physics which is the starting point for further more sophisticated *many body theories*. In the second section, the *independent particle approximation* is improved by

considering the neglected Coulomb- and the spin orbit interactions between the electrons, which lead to fine structure energy levels within a configuration and which therefore cause deviations from the simple single particle picture. Section 2.3 describes the electron- photon interaction as far as it is of relevance for atomic photoabsorption spectroscopy and the last part of Chapter 2 gives an introduction to the various many body theories which have been applied in this work. A very good review of these theories can be found in the articles by Wenden (1976, 1984) and on a more advanced level in the book *Atomic Photoeffect* written by Amusia (1990). It is convenient to present all equations in the CGS system, where  $(4\pi)^{-1}$  is defined to be equal the permittivity constant  $\epsilon_0$  and the electron charge  $e$  is set to be one.

## 2.1 The Independent Particle Approximation of a Multielectron System

An atom is usually considered as a many electron system, where the constituents interact with each other and with the point like nucleus (the nucleus is considered to have an infinite mass) via electromagnetic forces. A theoretical treatment of an atom/ion with the atomic number  $Z$  and  $N$  electrons requires first the knowledge of a suitable Hamiltonian  $H$  which is used to solve the time independent Schrödinger equation

$$\hat{H}\psi_k = E^k\psi_k \quad (2.1)$$

In most cases it is sufficient enough in a first approximation to take only the electrostatic Coulomb interactions between the electrons and the electron-nucleus into account with a Hamiltonian

$$H = \sum_{i=1}^N \left( \frac{p_i^2}{2m} - \frac{Z}{r_i} \right) + \sum_{i,k(i < k)}^N \frac{1}{r_{ik}} \quad (2.2)$$

The sum of the electron-electron interactions is of the same magnitude as the attractive electron-nucleus Coulomb force and therefore not negligible. It also



prevents a separation of the variables in the Schrödinger equation which makes a solution of eqn (2.1) unequivocally more difficult. A useful approximation is therefore to average the influence of all (N-1) electrons on the  $i^{\text{th}}$  electron together with the attractive Coulomb force  $Z/r_i$ , and to replace it by an *effective spherically symmetrical one electron central field potential*  $V^i(r)$ . The Hamiltonian may then be written as a sum of single particle Hamiltonians

$$H_o = \sum_{i=1}^N \left( \frac{p_i^2}{2m} + V^i(r) \right) \quad (2.3)$$

with a product ansatz for the total eigenstate  $\psi(1, 2, \dots, N) = \phi(1)\phi(2) \dots \phi(N)$ . The extremely complicated Schrödinger equation (2.1) in which the motions of all electrons are coupled via the Coulomb interaction is reduced to a set of N decoupled one particle Schrödinger equations

$$\left[ \frac{\hat{p}_i^2}{2m} + V^i(r) \right] \phi^i(r) = E^i \phi^i(r) \quad (2.4)$$

with the total energy of the atom  $E_o = \sum_i E^i$ . The physical meaning of the *central field model* is, that any given electron  $i$  moves independently of the others in an electrostatic field of the nucleus and the other (N-1) electrons, this field is assumed to be averaged in time over the motions of all electrons and to be spherically symmetric. The approximation is therefore called *the independent particle approximation* (IPA). The solution of the one electron Schrödinger equation is well known to be  $\phi(r) = r^{-1} P_{nl}(r) Y_{lm}(\vartheta, \varphi) \chi_m$ , and the parity of the multielectron function is therefore  $(-1)^{\sum l_i}$ .

It is convenient here to introduce the definition *electron configuration*, which determines the set of quantum numbers characterizing the total wavefunction in the IPA

$$(n_1 l_1)^{w_1} (n_2 l_2)^{w_2} \dots (n_q l_q)^{w_q} \quad (2.5)$$

with  $w_i$  the occupation number of the subshell  $i$ ,  $q$  the subshell number in the atom and  $\sum_{i=1}^q w_i = N$ . The problem with the product ansatz is, that it does

not take the Pauli-principle into account which is of fundamental importance for a Fermion system. The Pauli-principle reflects the physical indistinguishability of the electrons, which requires an antisymmetrized wavefunction  $\psi$  for the  $N$  electron system. It is well known, that the Pauli-principle can be satisfied in form of a determinantal function

$$\psi(1, 2, \dots, N) = \frac{1}{\sqrt{N!}} \begin{vmatrix} \phi_1(1) & \phi_1(2) & \dots & \phi_1(N) \\ \phi_2(1) & \phi_2(2) & \dots & \phi_2(N) \\ \vdots & \vdots & \ddots & \vdots \\ \phi_N(1) & \phi_N(2) & \dots & \phi_N(N) \end{vmatrix} \quad (2.6)$$

which is referred to as a so called *Slater determinant*. Since the central potential  $V(r)$  is unknown, the radial wavefunctions  $P_{nl}(r) = rR_{nl}$  cannot easily be obtained.

One commonly used approach here is the *Hartree-Fock* method, which is based on a variational principle. The philosophy behind this method is to find the best Slater determinant  $\psi$  of single particle radial wavefunctions obtained from a central field potential which minimizes the energy functional

$$E[\psi] = \frac{\langle \psi | \hat{H} | \psi \rangle}{\langle \psi | \psi \rangle} \quad (2.7)$$

The method is frequently called the *restricted Hartree-Fock* method since the single electron orbitals for different quantum numbers  $m_l$  and  $m_s$  are assumed to have the same radial wavefunction  $P_{nl}$  (Froese Fischer 1977).

The performance of the variational principle of the energy functional under conditions, in which the radial wavefunctions  $P_{nl}$  are orthonormal, leads to the *Hartree-Fock* equations [in Cowan 1981, eqn. (7.11)]

$$\left[ -\frac{\hbar^2}{2m} \frac{d^2}{dr^2} + \frac{l_i(l_i + 1)\hbar^2}{2mr^2} - \frac{Z}{r} + \sum_{j=1}^q (w_j - \delta_{ij}) \int_0^\infty \frac{1}{r'} P_{n_j l_j}^2(r') dr' - (w_i - 1)A_i(r) \right] P_{n_i l_i}(r) \\ = \epsilon_i P_{n_i l_i}(r) + \sum_{j(\neq i)=1}^q w_j [\delta_{l_i l_j} \epsilon_{ij} + B_{ij}(r)] P_{n_j l_j}(r) \quad (2.8)$$

for a spherically symmetric atom/ion with

$$A_i(r) = \frac{2l_i + 1}{4l_i + 1} \sum_{k>0} \begin{pmatrix} l_i & k & l_i \\ 0 & 0 & 0 \end{pmatrix}^2 \int_0^\infty \frac{r^k}{r^{k+1}} P_{n_i, l_i}^2(r') dr'$$

$$B_{ij}(r) = \left(\frac{1}{2}\right) \frac{2l_i + 1}{4l_i + 1} \sum_k \begin{pmatrix} l_i & k & l_i \\ 0 & 0 & 0 \end{pmatrix}^2 \int_0^\infty \frac{r^k}{r^{k+1}} P_{n_i, l_i}(r') P_{n_j, l_j}(r') dr'$$

and  $\epsilon_i, \epsilon_{ij}$  the Lagrange multipliers which insure the required orthonormality between the radial functions  $P_{nl}(r)$ .

For an N electron system, we obtain N equations for the  $P_{n_i, l_i}$ , but only q equations are different in the restricted Hartree-Fock method.

If the variational principle is applied to the energy of a term with a specific *LS* symmetry rather than to  $E_{av}$ , then the HF equations are the same as in eqn.(2.8) but with additional terms which are different for the specific terms of interest.

The first three terms in the HF equation correspond to the radial part of the Schrödinger equation for the  $i^{th}$  electron in an effective potential  $V_{eff}$  which is composed of the attractive Coulomb- and the repulsive centrifugal potential. The third term describes the repulsive Coulomb interaction between the electron  $i$  with all the others united in a potential  $V_{Cou}$ , and the terms containing  $A_i$  and  $B_{ij}$  come from the exchange part with its nonequivalent counterparts as  $V_{exc}$  which appears as a pure quantum mechanical effect and has no classical analogy. The sum of all terms can be approximated in a *local potential*

$$V^i(r) = V_{eff}(r) + V_{Cou}(r) + V_{exc}(r) \quad (2.9)$$

in which the  $i^{th}$  electron moves independently.

The HF equation is solved within the self consistent field method (SCF) which resembles an iterative process. An initial guess of the N single electron wavefunctions is used to calculate the Coulomb- and exchange potentials in eqn.(2.8), which are used for their part to calculate the new set of single particle radial-functions  $P_{nl}$ . The procedure is repeated until selfconsistency is achieved, which

means that the potential  $V^i(r)$  created through the charge distribution of all electrons produces wavefunctions, which for their part reproduce the local potential  $V^i(r)$

As a result, the energy eigenvalues of the electrons are functions of the main quantum number  $n$  and the angular quantum number  $l$ , which is in contrast to the case of the hydrogen atom

The atomic structure calculation codes RCN/RCG (Cowan 1984a,b) for example take a general *Herman and Skillman* potential (Herman & Skillman 1963) as a suitable starting atomic potential for the first configuration, the succeeding configurations are calculated with a starting potential from the previous one

Calculations, which use the same orbitals for an atom in its ground state and excited state characterized by a different electron configuration is usually referred to as a *frozen core approximation*. Here the negative of the eigenvalue  $\epsilon_i$  corresponds to the configuration average ionization energy for an electron in subshell  $n_i, l_i$ , which is called *Koopmans' theorem*. This approximation certainly does not quite reflect the reality since an innershell hole causes a new balance between all the electrostatic interactions through relaxation effects. However the HF theory in its frozen core approximation gives, for many species over a wide energy range, satisfactory predictions

In some cases, relaxation effects can play a crucial role in describing photoabsorption processes, as for example in the so called *giant resonance* energy region of the lanthanides (Wendin 1975, Amusia 1977), where the atom responds to the removal of an innershell electron in the form of some minor redistributions of the remaining electron charge, - not quantum number changes, but just readjustments in the form of slightly different radial wavefunctions  $P_{n,l}$ . This is demonstrated for the  $4f(^1P)$  wavefunction in  $\text{La}^{3+}$ , which is calculated first in the fully relaxed and then in the frozen core approximation as shown in Figure 2.1

In summary, the *independent particle picture* of the many electron atom is an approximation in which the overall motion of the electrons are averaged to

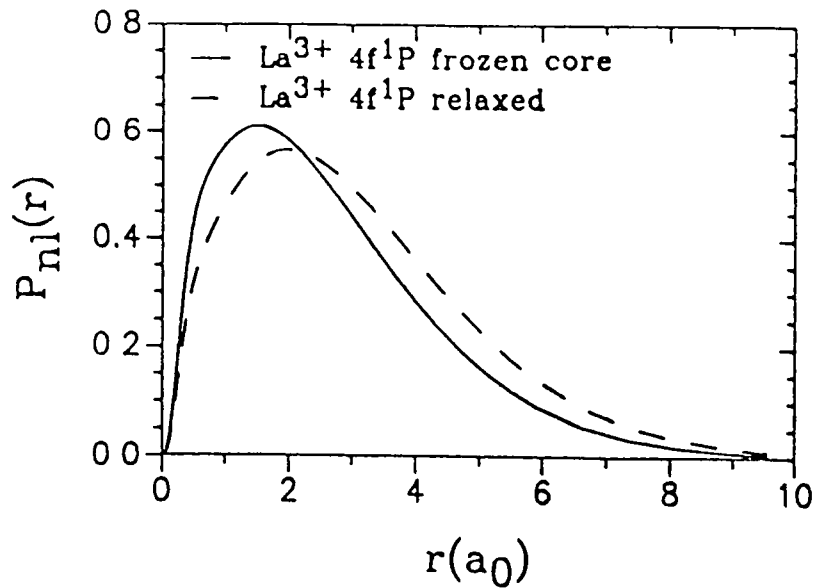


Figure 2.1  $4f(1P)$  orbital of  $La^{3+}$  in a frozen core and fully relaxed calculation. In the relaxed model, the orbital is pulled away from the core due to the fact that the inner shell  $4d$  hole is more completely screened by the other electrons and therefore reduces the attractive  $4d^{-1}4f$  interaction. It follows that the energy position of the  $4f(1P)$  giant resonance line in the relaxed calculation is  $2.5\text{eV}$  closer to the observed one than in the frozen core approximation.

orbitals obtained in a central field potential. The HF theory (in the frozen core approximation) reduces the many body problem to what appears to be a one electron description, that each of the nonequivalent electrons 'sees' a different effective spherically symmetric potential. However, relaxation effects go beyond the IPA, which can be taken into account directly in a HF self consistent field procedure or in a subsequent many body calculation as shown for  $La^{3+}$  in a following chapter. Relaxation effects are not the only collective phenomena, which have to be taken into account in order to describe the *giant dipole resonance* in  $La^{3+}$ . The  $LS$ -term dependence for the states of the  $4d^94f$  configuration which can be optically excited from the ground state give evidence for strong many body polarization effects for the  $^1P_1$  term. I would like to close this section with a brief historical review of how many body theories became established in atomic physics.

Collective models in atoms were already discussed as early as in the 1930s

when Bloch (1933) and Jensen (1937) described the electron distribution as a liquid capable of performing plasma oscillations in order to describe inelastic scattering of electrons by atoms in solids. A subsequent development of many body theories took place mainly in nuclear physics leading to concepts like shell models and collective giant resonances (Brown 1971). However many body methods came back to atomic physics in the 1960s mainly due to the work by Brand & Lundqvist (Brand & Lundqvist 1963, Brand et al 1967) and Amusia & coworkers (Amusia 1965, Amusia 1967, Amusia et al 1971) who treated the dynamics of the atom charge density via response functions and infinite diagrammatic perturbation theory focussing on collective effects in excitation and ionisation spectra. Diagrammatic perturbation theory in the spirit of Brueckner (1955a,b) and Goldstone (1957) was carried out by Kelly (1963, 1964) in calculating first ground state correlation energies in atoms and later photoionisation cross sections.

There was no clear evidence for the need of many body descriptions in atomic spectra until probably around 1960. In fact it was not even really clear what the shapes of photoionization cross section in a straightforward one electron picture would be. Such calculations then showed, that there can be a strong discrepancy between the experimental data and the independent particle model. A spectacular example is the well known  $4d \rightarrow \epsilon f$  photoabsorption spectrum of Xe, where the one electron model completely failed (Cooper 1964).

At the beginning of the 1960s, there was another important theoretical and experimental development concerning effects of many electron interactions in atoms. There was the classic experiment which provided data of the  $2s2p$  and higher double excitation in He (Madden & Codling 1963) following the theory of autoionizing resonances by Fano (1961) which concerns the aspect of correlated motion of two electrons in excited states. These problems subsequently became an ideal test ground for testing many body theories (Wendin 1970a,b and Wendin 1971).

## 2.2 Intra and Inter Configuration Interactions

With the radial wavefunctions  $P_{nl}(r)$  determined by solving the HF equations, their determinantal function  $\psi$  can be written as

$$\psi = (N!)^{-1/2} \det\{R_{nl}\} Y_{l_1 m_1} \chi_{s_1} Y_{l_2 m_2} \chi_{s_2} \dots Y_{l_N m_N} \chi_{s_N} \quad (2 10)$$

The total wavefunction  $\psi$  contains all information about the system's dynamical properties. If the wavefunction is known, all observables can be deduced from the matrix element of the Hamiltonian of interest. Therefore the evaluation of the total averaged energy of an atom is

$$E_{av} = \langle \psi | \hat{H} | \psi \rangle_{av} \quad (2 11)$$

with  $H$  the Hamiltonian of eqn (2 2) and the average is taken over all magnetic quantum numbers  $m_l$ , and  $m_s$ . The configuration average energy  $E_{av} = \sum_i (E_{kin}^i + E_{nuc}^i) + \sum_{i < j} E^{ij}$  is composed as a sum of three different types of energies, the kinetic energy of the  $i^{th}$  electron

$$E_{kin}^i = \int_0^\infty P_{n_i, l_i}(r) \left[ -\frac{\hbar^2}{2m} \frac{d^2}{dr^2} + \frac{l_i(l_i + 1)\hbar^2}{r^2} \right] P_{n_i, l_i}(r) dr \quad (2 12)$$

the electron-nuclear energy

$$E_{nuc}^i = \int_0^\infty -\frac{Z}{r} |P_{n_i, l_i}(r)|^2 dr \quad (2 13)$$

and the electron-electron Coulomb energy between the  $i^{th}$  and the  $j^{th}$  electron

$$E^{ij} = \begin{cases} F^0(ij) - \frac{1}{2} \sum_k \begin{pmatrix} l_i & k & l_j \\ 0 & 0 & 0 \end{pmatrix}^2 G^k(ij), & i \neq j \\ F^0(ii) - \left( \frac{2l_i+1}{4l_i+1} \right) \sum_{k>0} \begin{pmatrix} l_i & k & l_i \\ 0 & 0 & 0 \end{pmatrix}^2 F^k(ii), & i = j \end{cases} \quad (2 14)$$

The terms  $F^k(ij)$  and  $G^k(ij)$  represent the Slater integrals between electron  $i$  and electron  $j$

$$F^k(ij) = \int_0^\infty \int_0^\infty \frac{r_<^k}{r_>^{k+1}} |P_{n_i, l_i}(r_1)|^2 |P_{n_j, l_j}(r_2)|^2 dr_1 dr_2 \quad (2 15)$$

$$G^k(ij) = \int_0^\infty \int_0^\infty \frac{r_<^k}{r_>^{k+1}} P_{n_i, l_i}(r_1) P_{n_j, l_j}(r_2) P_{n_i, l_i}^*(r_2) P_{n_j, l_j}^*(r_1) dr_1 dr_2 \quad (2 16)$$

In the discussion so far, the structure of the multielectron system is described through a set of radial wavefunctions  $P_{nl}$  which constitute the configuration of the atom and which reflect the independent particle model. For a better description of the term structure, additional interactions between the electrons, which **do not** belong to closed subshells have to be taken into account. In most cases it is sufficient to consider the Coulomb- and the spin-orbit interaction among these electrons. The perturbation operator, which leads to the fine structure splitting among the terms of a configurations is then given by

$$\hat{H}^1 = \sum_{i < j} \frac{1}{r_{ij}} + \sum_i \frac{\alpha^2}{2} \left[ \frac{1}{r} \frac{dV_i}{dr} \right] < \hat{l}_i \hat{s}_i > \quad (2 17)$$

with  $\alpha$  the fine structure constant and the summation has to be taken over all electrons belonging to open subshells. The energy corrections in the Hamiltonian  $H^1$  are small in comparison with the configuration average energy  $E_{av}$ , but can lead to a significant redistribution of the term structure.

The corrections are considered in a first order approximation

$$< \psi | \hat{H}^1 | \psi > = < \psi | \hat{H}_{Coul}^1 | \psi > + < \psi | \hat{H}_{SO}^1 | \psi > \quad (2 18)$$

with the Coulomb- and the spin-orbit operator introduced on the right hand side of eqn (2 17) which lead to a mixing between the states described in eqn (2 10). The diagonalisation of the Coulomb energy matrix leads to the *LS* coupling scheme, whereas the spin-orbit operator is diagonal in *jj* coupling. Both terms together couple wavefunctions, which have the same total angular momentum  $J$ .



Therefore we can replace the basis set of uncoupled wavefunctions in eqn (2 10) by a new set of wavefunctions which give only diagonal contributions for one of the perturbation operators  $\hat{H}_{C_{ou}}^1$  and  $\hat{H}_{S_O}^1$ . Since the transformation is a unitary one, it is just a matter of convenience and not of physical significance, which coupling scheme is used. In the subsequent discussion, the LS coupling scheme with the basis functions

$$\psi = (N^1)^{-1/2} \det\{R_{nl}\} |\Sigma_k(l_k)L, \Sigma_k(s_k)S \quad JM \rangle \quad (2 19)$$

is used

### 2.2.1 Coulomb Interaction

Since the Coulomb operator is a two particle operator, the matrix element  $\langle \psi | \hat{H}_{C_{out}}^1 | \psi \rangle$  can be reduced to matrix elements between two particle states  $|n_i l_i n_j l_j LSJM \rangle$  which are diagonal in  $L, S, J$  and  $M$ . The decoupling procedure is rather complicated and lengthy (see Cowan 1981 chapter 12), so I will confine myself to the two particle problem, since it is sufficient for the analyses of the experimental spectra presented in this work.

The matrix element  $\langle n_i l_i n_j l_j LSJM | (r_{ij})^{-1} | n_i l_i n_j l_j LSJM \rangle$  can be evaluated as a sum of the Slater integrals  $F^k$  and  $G^k$  weighted with their appropriate angular coefficients  $f^k$  and  $g^k$

$$E_{C_{out}}^{ij} = \sum_{k>0} f^k(ij) F^k(ij) + \sum_k g^k(ij) G^k(ij) \quad (2 20)$$

The angular coefficients are defined through products of  $3j$  and  $6j$  symbols

$$f^k = (-1)^L (2l_i + 1)(2l_j + 1) \begin{pmatrix} l_i & k & l_i \\ 0 & 0 & 0 \end{pmatrix} \begin{pmatrix} l_j & k & l_j \\ 0 & 0 & 0 \end{pmatrix} \left\{ \begin{matrix} l_i & l_j & L \\ l_j & l_i & k \end{matrix} \right\} \quad (2 21)$$

$$g^k = (-1)^S (2l_i + 1)(2l_j + 1) \begin{pmatrix} l_i & k & l_j \\ 0 & 0 & 0 \end{pmatrix}^2 \left\{ \begin{matrix} l_i & l_j & L \\ l_i & l_j & k \end{matrix} \right\} \quad (2 22)$$

If the properties of the  $3j$  and  $6j$  symbols are taken under consideration, we obtain values for the angular coefficients, which are different from zero for  $f^k \neq$

Table 2 1 Configuration average energies  $E_{av}$  and Slater integrals  $F^k$  and  $G^k$  in units of [eV] calculated for the most important configurations in  $La^{3+}$

	$E_{av}$	$F^2$	$F^4$	$G^1$	$G^3$	$G^5$
$4d^9 4f$	103 39	13 06	8 32	15 51	9 66	6 81
$4d^9 5f$	125 57	0 83	0 39	0 61	0 41	0 30
$4d^9 6f$	130 56	0 43	0 21	0 32	0 21	0 16
$4d^9 7f$	133 21	0 24	0 12	0 18	0 12	0 09
$4d^9 8f$	134 81	0 15	0 08	0 11	0 08	0 06
$4d^9 9f$	135 84	0 10	0 05	0 08	0 05	0 04
$4d^9 10f$	136 55	0 07	0 04	0 05	0 04	0 03
$4d^9 6p$	118 34	0 95		0 20	0 21	
$4d^9 7p$	127 36	0 39		0 08	0 09	

0  $k = 0, 2, 4, \dots, \min(2l_i, 2l_j)$  and  $g^k \neq 0$   $k = |l_i - l_j|, |l_i - l_j| + 2, \dots, l_i + l_j$ . The Slater integral  $F^k$  determines the magnitude of the direct Coulomb interaction between terms with a certain angular momentum  $L$ , the  $f_k$  give the splitting of the configuration into components with different  $L$ , the  $g_k$ 's determine the splitting into the different multiplets  $^{2S+1}L$  and the  $G^k$ 's give the magnitude of the exchange interaction. The calculated values of the Slater integrals with the averaged configuration energy  $E_{av}$  for the  $4d^9 nf, mp$  configurations of  $La^{3+}$  with  $n = 4, \dots, 10$  and  $m = 6, 7$  are listed in Table [2 1].

Table [2 2] presents the values of the angular coefficients  $f^k$  and  $g^k$  for the states of the  $4d^9 4f$  configuration with  $J = 1$  which are observable in a photoabsorption experiment from an initial state with  $J = 0$ . Note, that the  $^1P$  and  $^3P$  levels differ only in the angular coefficient  $g^1$  of the exchange interaction which leads to an extremely large splitting in energy between the  $4d^9 4f(^1P)$  and  $4d^9 4f(^3P)$  states in  $La^{3+}$  since its appropriate Slater integral  $G^1(4d, 4f)$  is very large due to the strong overlap between the  $4d$  and  $4f$  wavefunctions. Moving

Table 2.2 Angular coefficients  $f^k$  and  $g^k$  of the d-f and d-p direct and exchange contributions of the energies  $E_{Coul}^{nj}$  for the terms  $^1P_1$ ,  $^3P_1$  and  $^3D_1$ , which are observable in a photoabsorption experiment of  $La^{3+}$  from the ground-state  $4d^{10}(^1S_0)$ . The monopole coefficient  $f_0$  is common to all terms and its contribution is usually included in the configuration average energy  $E_{av}$ .

	$f^2$	$f^4$	$g^1$	$g^3$	$g^5$
$^3D$	-0.05714	0.14286	-0.04286	-0.01905	-0.02165
$^3P$	-0.22857	-0.09524	-0.04286	-0.01905	-0.02165
$^1P$	-0.22857	-0.09524	1.9571	-0.01905	-0.02165
$^3D$	0.20		-0.0667	-0.04286	
$^3P$	-0.2		-0.0667	-0.04286	
$^1P$	-0.2		1.2667	-0.04286	

to the higher Rydberg states, the  $G^1$  value gets much smaller due to the lower spatial overlap between  $P_{4d}$  and  $P_{nf}$ . The result is, that the energy difference between  $^1P$  and  $^3P$  terms is small, although their angular coefficient  $g^1$  differs by a factor of about 46. This is demonstrated by a striking example in  $La^{3+}$ , where the Coulomb energies (direct and direct+exchange) are listed in Table [2.3] for the  $4d^94f$  and  $4d^98f$  configurations.

### 2.2.2 Spin-Orbit Interaction

The spin-orbit interaction leads to a splitting of the levels, which are degenerate in  $J$ . The appropriate operator is a single particle operator which has already the form of an irreducible tensor operator, so that the matrix element  $\langle n_i, l_i, n_j, l_j, LSJM | \Sigma_i \xi_i(r) \langle \hat{l}_i \hat{s}_i \rangle | n_i, l_i, n_j, l_j, L'S'J'M' \rangle$  can be evaluated straightforwardly for the spin-orbit energy.

Table 2 3 Calculated Coulomb energies  $E_{Coul}^{ij}$  for the terms  $^1P_1$ ,  $^3P_1$  and  $^3D_1$  of the  $4d^94f$  and  $4d^98f$  configurations in  $La^{3+}$

		$E_{Coul}^{ij}$ direct	$E_{Coul}^{ij}$ direct+exchange
$4d^94f$	$^1P$	-3 78eV	30 02eV
	$^3P$	-3 78eV	-1 0eV
	$^3D$	+0 44eV	-1 0eV
$4d^98f$	$^1P$	-0 003eV	0 15eV
	$^3P$	-0 003eV	-0 008eV
	$^3D$	+0 042eV	-0 008eV

$$E_{SO}^{ij} = \delta_{JJ'}\delta_{MM'}(-1)^{S+L'+J} \left\{ \begin{matrix} L & S & J \\ S' & L' & 1 \end{matrix} \right\} \times \sum_{k=i,j} \langle l_i l_j L || \hat{l}_k || l_i l_j L' \rangle \langle \frac{1}{2} \frac{1}{2} S || \hat{s}_k || \frac{1}{2} \frac{1}{2} S' \rangle \zeta_{n_k l_k} \quad (2 23)$$

with  $\xi_i(r) = \frac{\alpha^2}{2} \left[ \frac{1}{r} \frac{dV_i(r)}{dr} \right]$ , the radial factor of the spin-orbit operator and the radial integral  $\zeta_{n_i l_i} = \int_0^\infty \xi_i(r) |P_{n_i l_i}(r)|^2 dr$ , which is commonly referred as the *spin-orbit parameter*

The selection rules, which can be derived from the  $6j$  symbols are  $\Delta L = 0, \pm 1$ ,  $\Delta S = 0, \pm 1$ , with  $L = L' = 0$  and  $S = S' = 0$  forbidden, this means that  $L$  and  $S$  lose their function as "good quantum numbers" For the diagonal elements, the expression (2 23) can be simplified after evaluation of the  $6j$  symbol to  $1/2[J(J+1) - L(L+1) - S(S+1)]\xi(n_i l_i n_j l_j L)$ , with the new spin-orbit parameter as a linear combination of  $\zeta_{n_i l_i}$  and  $\zeta_{n_j l_j}$ . The advantage of this description is, that it is sometimes very easy to see without carrying explicit calculations, which terms have no spin-orbit contribution. For example the prominent  $4d^94f(^1P_1)$  term has no energy contribution due to the spin orbit interaction, since  $J$  is equal  $L$  and total spin  $S$  is zero

However, it is usually easier to calculate the spin orbit matrix elements in the  $jj$  coupling scheme  $\langle n_i l_i j_i n_j l_j J M | \Sigma_i \xi_i(r) (\hat{l}_i \hat{s}_i) | n_i l_i j_i' n_j l_j J' M' \rangle$  with a subsequent unitary transformation into the  $LS$  basis. We obtain the spin-orbit energy within the  $jj$  basis

$$E_{SO}^{ij} = \delta_{JJ'} \delta_{MM'} \delta_{j_i j_i'} \delta_{j_j j_j'} \frac{1}{2} \sum_{k=i,j} [j_k(j_k + 1) - l_k(l_k + 1) - 3/4] \zeta_{n_k l_k} \quad (2.24)$$

With the use of the transformation matrix

$$\langle (l_i s_i) j_i, (l_j s_j) j_j J | (l_i l_j) L (s_i s_j) S J \rangle = [j_i, j_j, L, S]^{1/2} \begin{Bmatrix} l_i & s_i & j_i \\ l_j & s_j & j_j \\ L & S & J \end{Bmatrix} \quad (2.25)$$

the eigenvectors in  $jj$ -coupling can be relatively easily transformed into the  $LS$ -coupling scheme after the evaluation of the  $9j$  symbol.

The spin-orbit integrals  $\zeta_{n,l}$  are calculated for the  $4d^9 n f, m p$  configurations of  $\text{La}^{3+}$  and listed in Table [2.4]. The spin-orbit energies can then be very easily evaluated from eqn (2.24) when the  $jj$ -coupling scheme is used. As an example, the spin-orbit energies for the  $4d^9 4f$  states with  $J = 1$  in  $\text{La}^{3+}$  are calculated within the  $jj$  basis and listed in Table [2.5]. In order to obtain the spin-orbit energies within the  $LS$  basis, the appropriate transformation matrix  $jj \rightarrow LS$  is required from eqn (2.25)

	$\begin{pmatrix} 5 & 7 \\ 2 & 2 \end{pmatrix}$	$\begin{pmatrix} 5 & 5 \\ 2 & 2 \end{pmatrix}$	$\begin{pmatrix} 3 & 5 \\ 2 & 2 \end{pmatrix}$
$^3D$	-0.37796	-0.67612	0.63246
$^3P$	-0.53452	0.71714	0.44721
$^1P$	0.75593	0.16903	0.63246

With the help of the transformation matrix, the spin-orbit energy matrix in the  $LS$  coupling scheme can be very easily obtained from the  $jj$ -energy (diagonal) matrix via a unitary matrix transformation. Results are listed in Table [2.6] again for the  $4d^9 4f$  and  $4d^9 8f$  configurations as representative examples.

In the case of gold, where we explain the resonant photoabsorption part due to the  $5p \rightarrow 5d$  and  $4f \rightarrow 5d$  transitions between the initial configuration  $5d^9 6s^2$

Table 2 4 Calculated spin-orbit radial integrals  $\zeta_{4d}$  and  $\zeta_{nf}/\zeta_{mp}$  for the  $4d^9nf, mp$  configurations of  $La^{3+}$

	$\zeta_{4d}$	$\zeta_{nf}/\zeta_{mp}$
$4d^94f$	1 12	0 08
$4d^95f$	1 14	0 00
$4d^96f$	1 14	0 00
$4d^97f$	1 14	0 00
$4d^98f$	1 14	0 00
$4d^99f$	1 14	0 00
$4d^910f$	1 14	0 00
$4d^96p$	1 14	0 29
$4d^97p$	1 14	0 13

and the final configurations  $5p^55d^{10}6s^2$  and  $4f^{13}5d^{10}6s^2$ , the term structure within these configurations is solely determined by the spin-orbit interaction of the single particle hole state. Therefore the  $jj$ -coupling scheme is appropriate for the description of the fine structure components. The spin-orbit interaction of the  $5d^{-1}$  hole, which has a calculated spin-orbit parameter  $\zeta_{5d} = 0.64eV$ , splits the  $5d^96s^2$  configuration into two states  $^2D_{5/2}$  and  $^2D_{3/2}$  separated in energy by about 1.28eV following eqn (2.24). Electrons from both states can be optically excited

Table 2 5  $Spm$ -orbit energies for the  $4d^94f$  states with  $J = 1$  of  $La^{3+}$  calculated in the  $jj$  coupling scheme. The energy difference between the 2nd and 3rd row gives approximately the spin-orbit splitting of the 4d subshell as 2.8eV

$\langle 4d_{5/2}4f_{7/2}   \xi(r)(\hat{l}\hat{s})   4d_{5/2}4f_{7/2} \rangle = -1.00eV$
$\langle 4d_{5/2}4f_{5/2}   \xi(r)(\hat{l}\hat{s})   4d_{5/2}4f_{5/2} \rangle = -1.28eV$
$\langle 4d_{3/2}4f_{5/2}   \xi(r)(\hat{l}\hat{s})   4d_{3/2}4f_{5/2} \rangle = 1.52eV$

Table 2 6 Spin-orbit energies for the  $4d^94f$  and  $4d^98f$  states with  $J = 1$  of  $La^{3+}$  calculated in the LS coupling scheme

	$4d^94f$	$4d^98f$
$\langle^1 P \xi(r)(\hat{l}\hat{s}) ^1 P \rangle =$	0 00eV	0 00eV
$\langle^1 P \xi(r)(\hat{l}\hat{s}) ^3 P \rangle =$	0 68eV	0 81eV
$\langle^1 P \xi(r)(\hat{l}\hat{s}) ^3 D \rangle =$	1 04eV	1 14eV
$\langle^3 P \xi(r)(\hat{l}\hat{s}) ^3 P \rangle =$	-0 64eV	-0 57eV
$\langle^3 D \xi(r)(\hat{l}\hat{s}) ^3 D \rangle =$	-0 12eV	0 00eV
$\langle^3 D \xi(r)(\hat{l}\hat{s}) ^3 P \rangle =$	0 85eV	0 81eV

into states with a  $5p^{-1}$  or  $4f^{-1}$  hole. The large  $\zeta_{5p} = 10.7\text{ eV}$  value is responsible for the big energy gap between the  $^2P_{3/2}$  and  $^2P_{1/2}$  states of the  $5p^{-1}5d^{10}6s^2$  configuration which is calculated to be 16.1 eV. Considering the case of the  $4f^{-1}$  hole configuration, the  $^2F_{5/2}$  lies 3.7 eV below the  $^2F_{7/2}$  with the calculated spin-orbit parameter  $\zeta_{4f} = 1.05\text{ eV}$ . The calculations so far describe the Coulomb and spin-orbit interaction within a configuration in which one or two particles (electrons or holes) are involved like the  $4d^{-1} - 4f^1$  Coulomb interaction in  $La^{3+}$  or the  $5d^{-1}$  spin-orbit interaction in the case of gold. However, in the general case of an atom with more than two open subshells, the application of the theory can be generalized (see Cowan 1981, chapter 12) and we obtain a fine structure energy splitting within a configuration

$$E_{fs}^1 = \sum_{i=1}^q \left[ \sum_{k>0} f^k(\nu_i) F^k(\nu_i) + d_i \zeta_{n_i, l_i} \right] + \sum_{i=1}^{q-1} \sum_{j=i+1}^q \left[ \sum_{k>0} (f^k(\nu_j) F^k(\nu_j) + g^k(\nu_j) G^k(\nu_j)) \right] \quad (2.26)$$

with  $f^k, g^k$  and  $d_i$  the angular coefficient calculated in the same coupling scheme

### 2.2.3 Relativistic Corrections

For heavier elements, a proper treatment for a quantitative description of the many-electron term structure would be within a relativistic Dirac-Hartree-Fock (DHF) theory (Grant 1970, Desclaux 1975). However the equations which have to be solved in the relativistic theory, are considerably more complex which makes the calculations of the energy-level structure much more difficult. In the nonrelativistic HF approach discussed in this work, the major relativistic effects like the *Darwin-* and *mass velocity terms* are taken into account as first order perturbation corrections. The influence of these corrections is restricted to the configuration average energy and therefore do not affect the fine structure splitting. The corrections are

$$E_D^i = -\delta_{l,0} \frac{\alpha^2}{4} \int_0^\infty P_{n,l,i}(r) \frac{dV^i(r)}{dr} r \frac{d}{dr} \left( \frac{P_{n,l,i}(r)}{r} \right) dr \quad (2.27)$$

$$E_{mv}^i = -\frac{\alpha^2}{4} \int_0^\infty P_{n,l,i}(r) (\epsilon_i - V^i(r))^2 P_{n,l,i}(r) dr \quad (2.28)$$

with  $\epsilon_i$  the eigenvalue of the  $i^{\text{th}}$  electron. For the  $4d^{10} \rightarrow 4d^9 4f$  transitions in  $\text{La}^{3+}$ , these relativistic corrections were calculated to be of the order of 0.8 eV.

### 2.2.4 Intermediate Coupling

In many cases, when neither the spin-orbit nor the Coulomb interaction is small when compared with the other, the eigenvalues of the Hamiltonian operator are not even approximately similar to diagonal elements of the energy matrix. The procedure then is to diagonalize the energy matrix for the states with a certain  $J$  in order to obtain the eigenvalues, which is usually achieved through a numerical procedure.

Although, by use of the intermediate coupling scheme, the quantum numbers  $L$  and  $S$  lose their physical meaning as a preservational quantity of the total system, nevertheless, the levels are often still labeled in the Russell Saunders notation  $^{2S+1}L_J$ , where the appropriate wavefunctions are presented as a linear



Table 2.7 Mixing coefficients for the  $4d^9 4f$  and  $4d^9 8f$  states of  $\text{La}^{3+}$  in the intermediate coupling scheme

	$4d^9 4f(^1P)$	$4d^9 4f(^3P)$	$4d^9 4f(^3D)$
$4d^9 4f(^1P)'$	0.999	0.023	0.039
$4d^9 4f(^3P)'$	-0.016	0.994	-0.167
$4d^9 4f(^3D)'$	-0.043	0.166	0.985
	$4d^9 8f(^1P)$	$4d^9 8f(^3P)$	$4d^9 8f(^3D)$
$4d^9 8f(^1P)'$	0.633	0.447	0.632
$4d^9 8f(^1P)'$	0.756	-0.535	-0.378
$4d^9 8f(^3P)'$	0.169	0.717	-0.676

combination of the 'pure' eigenstates in the  $LS$  coupling scheme. The coefficients are obtained by diagonalization of the energy matrix and taking the orthonormality conditions for the eigenstates into account. The mixing coefficients are given for the  $4d^9 4f$  and  $4d^9 8f$  configurations in Table [2.7]. The new eigenstates are marked with ( $'$ ), in order to distinguish the intermediate eigenstates from the pure  $LS$  coupled ones. It is clearly recognizable from these tables, that the states of the  $4d^9 4f$  configuration are nearly pure  $LS$  coupled because the Coulomb interaction for the  $4f$  electron with its appropriate  $4d^{-1}$  hole is extremely strong. However, for the higher Rydberg states, where the electron-hole orbitals are largely separated in space, the spin-orbit interaction comes to its best advantage, which leads to an enormous mixing between the  $LS$  eigenstates.

## 2.2.5 Interconfiguration Interactions

The perturbation operator  $\hat{H}^1$  of eqn (2.17) does not only lead to a fine structure splitting within a configuration, it can also mix states belonging to different configurations. The admixture between states  $\phi_1$  and  $\phi_2$  belonging to different configurations can be expressed in a second order perturbation expansion  $a = \langle$

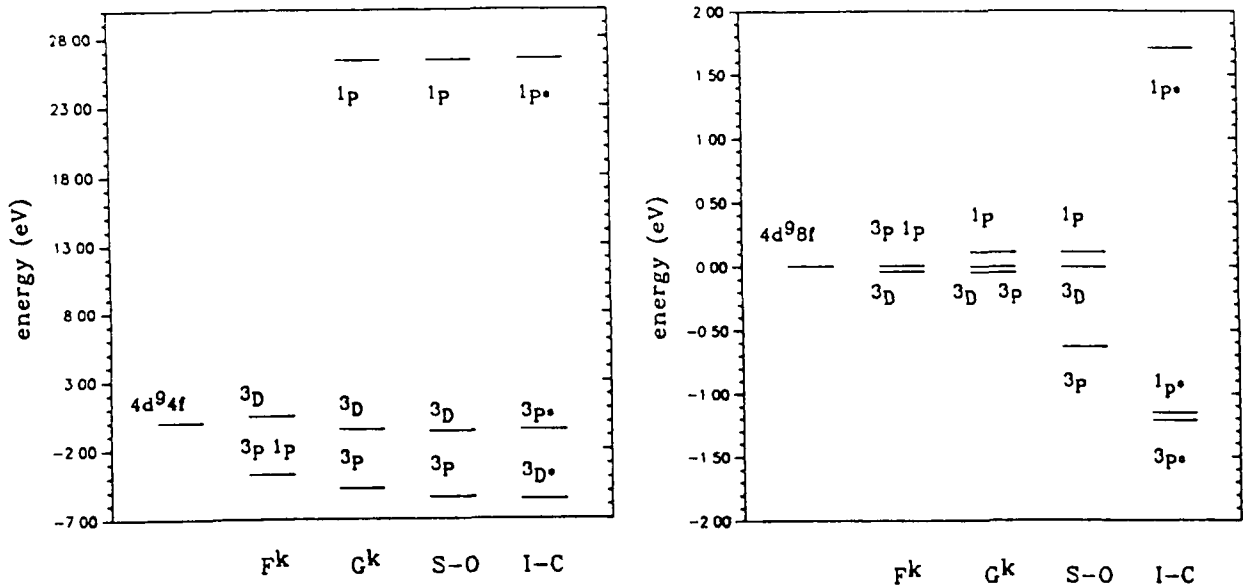


Figure 2.2 Schematic drawing of the development of an energy-level structure of the  $4d^9 4f$  and  $4d^9 8f$  configuration of  $La^{3+}$  using the LS coupling notation. Starting with the spherically averaged central field energy (configuration average energy) and then taking successively the Coulomb interaction energies (first the direct and then additionally the exchange interaction) into account followed by the spin-orbit energy and then finally all Coulomb and spin-orbit contributions in an intermediate coupling scheme using the LS notation. It is illustrated, that in the  $4d^9 4f$  configuration, the exchange interaction determines the term structure, whereas in the  $4d^9 8f$  configuration it is the spin-orbit interaction, especially the non diagonal elements that are large (see Table [2.6]) and lead to a deviation of the LS term structure which resembles more an energy-level structure one would obtain under pure  $jj$  coupling conditions.

$\phi_1|\hat{H}^1|\phi_2 > / (E_1 - E_2)$  with an appropriate energy shift  $\Delta E = | < \phi_1|\hat{H}^1|\phi_2 > |^2 / (E_1 - E_2)$  which can be significant, if the CI matrix element  $< \phi_1|\hat{H}^1|\phi_2 >$  is of the same magnitude as the difference in energy  $(E_1 - E_2)$ . The selection rules, which determine what states can be mixed by the operator, are the same as for intra configuration interactions,  $\hat{H}^1$  connects only states which have the same total angular momentum  $J$ . In most cases it is sufficient to consider only the Coulomb operator as a perturbation which mixes states with the same quantum numbers  $L, S, J$  and  $M$ .

Instead of carrying out extended perturbation calculations, the states which contribute to a mixing can be directly included in a CI energy matrix which is then diagonalized in order to obtain the mixing coefficients and the eigenvalues.

The CI matrix elements of the Coulomb operator can be evaluated in analogy to eqn.(2.20) as weighted Slater integrals

$$< \phi_1|\hat{H}^1|\phi_2 > = \sum_k (r_d^k R_d^k + r_e^k R_e^k) \quad (2.29)$$

with

$$R_d^k(i^{(1)}j^{(1)}k^{(2)}l^{(2)}) = \int_0^\infty \int_0^\infty \frac{r_1^k}{r_1^{k+1}} P_{n_i l_i}^{(1)}(r_1) P_{n_j l_j}^{(1)}(r_2) P_{n_k l_k}^{(2)}(r_1) P_{n_l l_l}^{(2)}(r_2) dr_1 dr_2$$

$$R_e^k(i^{(1)}j^{(1)}k^{(2)}l^{(2)}) \equiv R_d^k(i^{(1)}j^{(1)}l^{(2)}k^{(2)}) \quad (2.30)$$

where index (1) and (2) represent the configuration number. The angular coefficients  $r_d^k$  and  $d_e^k$  can be obtained in analogy to the single configuration direct  $g^k$  and exchange  $f^k$  coefficients from eqn.(2.21) and (2.22).

Interconfiguration interactions play an important role in calculating the  $\text{La}^{3+}$  spectrum. Large mixing among the  $4d^9(4, \epsilon)f$  configurations in the  $^1P$  channel is observed. The attempt to identify the dominant resonance line in the experimental spectrum as the  $4f(^1P)$  fails completely in the single configuration approximation. Instead, an extended  $4d^9(n, \epsilon)f$  intrachannel CI-HF calculation

shifts the predicted  $4f(^1P)$  from 129.7 eV down to 120.9 eV (experimental value 118.9 eV) with an oscillator strength and autoionizing width, which are comparable with the experimental data. The energy integrals  $R_d^k$  and  $R_e^k$  for these configurations are given in Table [2.8], which shows that the  $4d^94f - 4d^9nf$  interactions are extremely large among all possible interconfiguration interactions. The angular coefficients  $r_d^k$  and  $r_e^k$  have the same values as the  $f^k$ 's and  $g^k$ 's in Table [2.2].

The interaction energies can be calculated with use of eqn (2.29) from the energy integrals and their appropriate angular coefficients. The  $4d^94f(^1P) - 4d^9nf(^1P)$  interaction energies are listed in Table [2.9] and are of considerable size, about 1-5 eV. A more detailed investigation of these effects which is a key point in the understanding of the giant resonance phenomenon will be provided in Chapter 3.

## 2.3 Electromagnetic Dipole Transitions

The theory of atomic photoabsorption is based on first order time dependent perturbation theory, in which the probability per unit time for a transition taking place between two states  $|i\rangle$  and  $|f\rangle$  due to a weak time dependent electromagnetic interaction can be expressed by *Fermi's golden rule*

$$P_{i \rightarrow f} = \frac{2\pi}{\hbar} |\langle \psi_i | H^{em} | \psi_f \rangle|^2 \rho(E)|_{E_f} \quad (2.31)$$

with  $\rho(E)$  the density of final states, which is to be replaced by the Dirac delta function  $\delta(E - E_f)$  for a discrete transition and by unity for continuum transitions if the continuum functions are normalized in energy. In almost all photoabsorption experiments, the light intensity is low enough to provide calculational results with sufficient accuracy in this approximation.

In the so called *dipole approximation in length form*, the matrix element

Table 2 8 Energy integrals in  $[1000\text{cm}^{-1}]$  for the  $4d^9nf - 4d^9mf$  interconfiguration Coulomb interactions in  $\text{La}^{3+}$

	$R_d^2$	$R_d^4$	$R_e^1$	$R_e^3$	$R_e^5$
$4d^94f - 4d^95f$	19 41	13 23	24 48	15 73	11 23
$4d^94f - 4d^96f$	13 72	9 46	17 47	11 31	8 09
$4d^94f - 4d^97f$	10 27	7 12	13 15	8 54	6 12
$4d^94f - 4d^98f$	8 05	5 61	10 34	6 74	4 83
$4d^94f - 4d^99f$	6 54	4 56	8 41	5 49	3 94
$4d^94f - 4d^910f$	5 45	3 81	7 02	4 58	3 29
$4d^95f - 4d^96f$	4 37	2 26	3 55	2 38	1 73
$4d^95f - 4d^97f$	3 20	1 71	2 68	1 81	1 31
$4d^95f - 4d^98f$	2 48	1 36	2 11	1 43	1 04
$4d^95f - 4d^99f$	2 00	1 11	1 72	1 17	0 84
$4d^95f - 4d^910f$	1 67	0 93	1 44	0 97	0 71
$4d^96f - 4d^97f$	2 50	1 30	1 93	1 31	0 96
$4d^96f - 4d^98f$	1 94	1 02	1 52	1 04	0 76
$4d^96f - 4d^99f$	1 57	0 82	1 24	0 85	0 61
$4d^96f - 4d^910f$	1 30	0 64	1 03	0 71	0 52
$4d^97f - 4d^98f$	1 52	0 77	1 15	0 79	0 58
$4d^97f - 4d^99f$	1 23	0 63	0 93	0 64	0 47
$4d^97f - 4d^910f$	1 02	0 53	0 78	0 53	0 39
$4d^98f - 4d^99f$	0 99	0 50	0 74	0 51	0 37
$4d^98f - 4d^910f$	0 82	0 42	0 62	0 43	0 31
$4d^99f - 4d^910f$	0 68	0 34	0 50	0 34	0 26

Table 2.9 Calculated energy values for the  $4d^9 4f(1P) - 4d^9 m f(1P)$  interconfiguration Coulomb interactions in  $La^{3+}$

$\langle 4d^9 4f(1P)   \hat{H}_{Coul}^1   4d^9 5f(1P) \rangle =$	5.2 eV
$\langle 4d^9 4f(1P)   \hat{H}_{Coul}^1   4d^9 6f(1P) \rangle =$	3.7 eV
$\langle 4d^9 4f(1P)   \hat{H}_{Coul}^1   4d^9 7f(1P) \rangle =$	2.8 eV
$\langle 4d^9 4f(1P)   \hat{H}_{Coul}^1   4d^9 8f(1P) \rangle =$	2.2 eV
$\langle 4d^9 4f(1P)   \hat{H}_{Coul}^1   4d^9 9f(1P) \rangle =$	1.8 eV
$\langle 4d^9 4f(1P)   \hat{H}_{Coul}^1   4d^9 10f(1P) \rangle =$	1.5 eV

$\langle \psi_i | H^{em} | \psi_f \rangle$  can be evaluated by use of the Wigner-Eckart theorem

$$\langle \psi_i | H^{em} | \psi_f \rangle = (E_f - E_i) \frac{1}{3} \sum_q (-1)^{J-M} \begin{pmatrix} J_f & 1 & J_i \\ -M_f & q & M_i \end{pmatrix} \langle \gamma_i J_i || r^{(1)} || \gamma_f J_f \rangle \quad (2.32)$$

where  $\psi_i$  is represented by the quantum numbers  $\gamma_i, J_i$  and  $M_i$  and  $\psi_f$  through the quantum numbers  $\gamma_f, J_f$  and  $M_f$ . The  $3j$  symbol provides immediately the dipole selection rules with  $\Delta J = 0, \pm 1$ ,  $\Delta M = 0, \pm 1$  and  $J_i = J_f \neq 0$ .

For a monochromatic non polarized photon beam, the absorption cross section  $\sigma_{abs}$  is defined as the averaged transition probability of eqn (2.32) over all sublevels  $M_i$  of the initial state  $|\gamma_i J_i M_i\rangle$  to all sublevels  $|\gamma_f J_f M_f\rangle$  of the final continuum states, normalized to the number of incident photons per unit time and per unit area

$$\sigma_{abs}(\hbar\omega) = \frac{4\pi^2\alpha}{3} \hbar\omega \frac{1}{2J_i + 1} |D_{i,f}|^2 \quad (2.33)$$

with  $\alpha$  the fine structure constant and  $|D_{i,f}|^2 = |\langle \gamma_i J_i || r^{(1)} || \gamma_f J_f \rangle|^2$  the square product of the absolute value of the reduced dipole matrix element normalized per unit energy

Discrete transitions are usually characterized by the oscillator strength  $f_{abs}$  for an absorption process or  $f_{em}$  for an emission process, which are related to the reduced dipole matrix element  $D_{i,f}$  with  $f_{i,f} = \frac{1}{3} \frac{1}{2J_i + 1} \frac{2m}{\hbar^2} \hbar\omega (D_{i,f})^2$ . The oscillator

strength is dimensionless and has the physical significance of the effective number of classical electron harmonic oscillators, which would absorb radiation of the energy  $\Delta E$  as strongly does the atom. For strong spectral lines,  $f$  is of the order of one. In order to characterize a transition between two states with a symmetrical quantity, the  $gf$  value is frequently used,  $g$  is the statistical weight of the initial state and we obtain  $gf = (2J_i + 1)f$ . Finally a very useful oscillator strength sum rule defines its distribution within a transition array

$$f(|l_i^{w_i}, \gamma J M \rangle \rightarrow \sum_{n' l' \gamma' J'} |l_i^{w_i-1} n' l' \gamma' J' \rangle) = w_i \quad (2.34)$$

Provided that relativistic effects are negligible, the total oscillator strength which includes all possible discrete and continuum transitions from subshell  $(n_i, l_i)$  is equal to its occupation number  $w_i$ .

The characteristic quantity for calculating the oscillator strength or the photoabsorption cross section is the reduced dipole matrix element  $D_{i,f}$  between the initial state  $|\gamma_i J_i \rangle$  and final state  $|\gamma_f J_f \rangle$ . These states are usually expanded in terms of a suitable set of basis functions  $|\beta J \rangle$  with

$$|\gamma J \rangle = \sum_{\beta} y_{\beta J}^{\gamma} |\beta J \rangle \quad (2.35)$$

The basis expansion in the atomic structure calculation codes RCN/RCG (Cowan 1981, Cowan 1984a,b) are obtained by diagonalizing the energy matrix for the states with a certain parity and quantum number  $J$ . In theory, a complete set of basis functions is required in order to obtain the correct result, although in practice a judiciously selected number of basis functions are very often sufficient in order to obtain satisfactory results. I would like to point out here again, that a multiconfiguration basis takes electron correlations into account which goes beyond the independent particle description. The dipole matrix may then be written as

$$D_{i,f} = \sum_{\beta} \sum_{\beta'} y_{\beta J}^{\gamma} \langle \beta J || r^{(1)} || \beta' J' \rangle y_{\beta' J'}^{\gamma'} \quad (2.36)$$

which can be generalized to a unitary matrix transformation

$$\mathbf{D}_{JJ'} = \tilde{\mathbf{Y}}\mathbf{D}_{\beta\beta'}\mathbf{Y}' \quad (2.37)$$

where the trace of the matrix is invariant. Thus the  $D_{JJ'}$  matrix for the actual atom is just the  $D_{\beta\beta'}$  matrix for pure  $LS$  coupling representation transformed into the actual intermediate coupling representation in a configuration interaction expansion.

The dipole matrix element in  $LS$  coupling  $D_{LS} = \langle LSJ || r^{(1)} || L'S'J' \rangle$  can be evaluated by (Cowan 1981, chapter 14.11)

$$D_{LS} = \delta_{SS'}(-1)^{L+S+J'+1}[J, J']^{1/2} \begin{Bmatrix} L & S & J \\ J' & 1 & L' \end{Bmatrix} D_1 D_2 D_7 \langle n_i l_i || r^{(1)} || n_f l_f \rangle \quad (2.38)$$

The various  $D_m$  subfactors encountered in different steps of the calculations in order to reduce the multielectron transition rate to the dipole matrix element of the *jumping* electron  $d_{if} = \langle n_i l_i || r^{(1)} || n_f l_f \rangle$  (Cowan 1981) which in turn can be reduced to a radial integral with

$$d_{if} = (-1)^{l_i} [l_i, l_f]^{1/2} \begin{pmatrix} l_i & 1 & l_f \\ 0 & 0 & 0 \end{pmatrix} \int_0^\infty P_{n_i l_i}(r) r P_{n_f l_f}(r) dr \quad (2.39)$$

There are several selection rules which can be deduced from the  $3j$  and  $6j$  symbols of eqn (2.38) and eqn (2.39) in addition to the selection rule for the total angular momentum  $J$  (eqn (2.32)) with  $\Delta S = 0$ ,  $\Delta L = 0, \pm 1$ ,  $L = L' \neq 0$  and  $l_i - l_f = \pm 1$ . The electric dipole transition involves a change of parity  $\Delta l = \pm 1$ . Furthermore under pure  $LS$  coupling conditions, transitions can only occur between states with the same multiplicity ( $\Delta S = 0$ ).

In the application to the  $La^{3+}$  problem, we consider the transitions from the ground state  $4d^{10}(^1S_0)$  to all states of the  $4d^9 4f$  configuration in the single configuration approximation. The Coulomb and the spin-orbit interaction split the  $4d^9 4f$  configuration into 20 fine structure components of singlet and triplet terms with different  $J$  values as shown in Table [2.10]. The selection rules reduce



Table 2.10: *Fine structure components of the  $4d^9 4f$  configuration in the  $LS$  coupling notation.*

j	
0	$^3P_0$
1	$^3P_1$ $^3D_1$ $^1P_1$
2	$^3F_2$ $^3D_2$ $^3P_2$ $^1D_2$
3	$^3G_3$ $^3F_3$ $^3D_3$ $^3F_3$
4	$^3H_4$ $^3G_4$ $^3F_4$ $^1G_4$
5	$^3H_5$ $^3G_5$ $^1H_5$
6	$^3H_6$

the number of terms to the three  $^3P_1$ ,  $^3D_1$  and  $^1P_1$  states, which are observable in a photoabsorption spectrum described in the dipole approximation. However, these states are closely  $LS$  coupled as shown in Table [2.7], which means, that only the  $4d^{10}(^1S_0) \rightarrow 4d^9 4f(^1P_1)$  transition line is expected to be observable in the photoabsorption spectrum. Since the  $^1P_1$  is mixed with the other two  $J = 1$  states via the spin-orbit operator, weak intercombination lines to these states are observed. With increasing main quantum number  $n$ , the spin-orbit interaction becomes more dominant. This results in a redistribution of oscillator strength to spin-orbit split transitions with intensities which depart greatly from the  $LS$  coupled states. Under pure  $jj$  coupling conditions, the oscillator strength distribution between the spin-orbit split subshells is proportional to the ratio of their statistical weights  $(2J+1)$ .

A redistribution of oscillator strength does not occur only within a single configuration. The Coulomb part of the perturbation operator  $\hat{H}^1$  in eqn.(2.18) causes a strong mixing between the  $^1P_1$  states of the  $4d^9 n f$  intrachannel configurations, which has a significant influence on the intensity distribution among the Rydberg transition lines. The predicted  $f$  value for the  $4d^{10}(^1S_0) \rightarrow 4d^9 4f(^1P_1)$  in

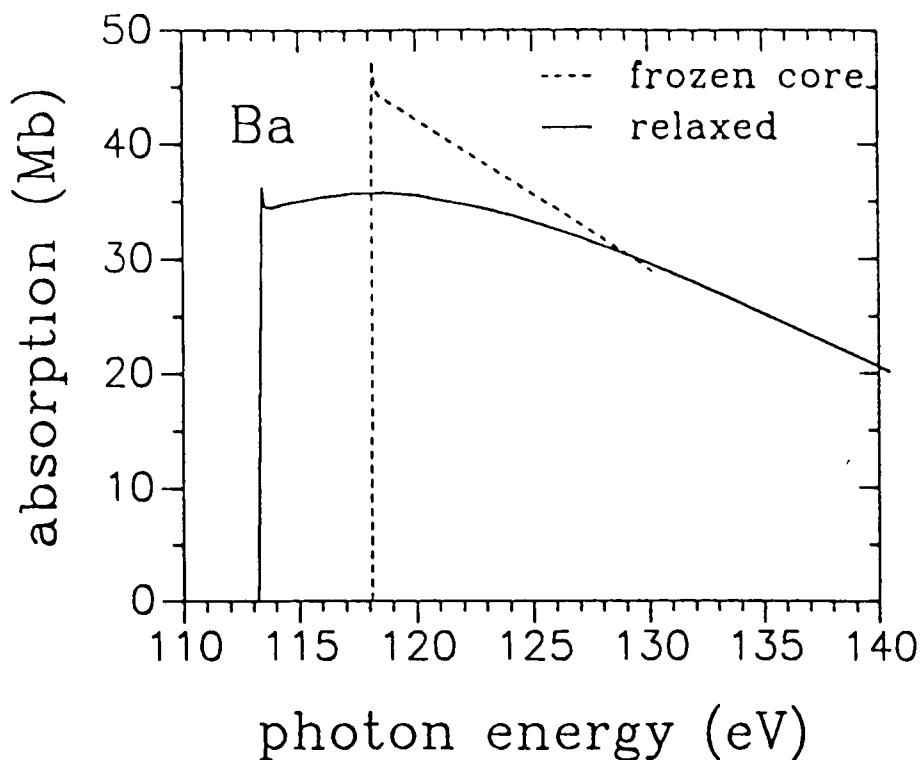


Figure 2.3 Photoabsorption cross section of Ba  $4d \rightarrow \epsilon f(^1P)$  with use of relaxed and frozen core orbitals

a single configuration calculation is 11.6. Intrachannel CI-HF calculations reduce the  $f$  value to less than half of its magnitude in favour of the transitions into the higher Rydberg states which gain in strength. Therefore not only the energy positions of transition lines, but also the transition strengths provide valuable information about electron correlations in atoms and ions.

As already discussed, the consideration of relaxation effects can bring a substantial improvement for the description of photoabsorption spectra. These effects do not only improve the prediction of transition energies or the threshold behaviour, they also determine the shape of photoionization cross sections as demonstrated with a simple  $4d \rightarrow \epsilon f(^1P)$  cross section calculation for atomic Ba using eqn (2.33). The calculations were carried out once with the use of relaxed orbitals and ones within the frozen core approximation. Relaxation effects do not only shift the  $4d$  threshold, the photoabsorption maximum is pushed beyond the threshold as shown in Figure 2.3.

### 2.3.1 Resonant Photoabsorption

In the photoabsorption energy region well above the ionization energy of the atom/ion, several excitation channels are usually open which may lead to pronounced interference effects in the absorption strength due to interconfiguration mixing via the perturbation Hamiltonian  $H^1$  of eqn (2.18) which is disregarded in the independent particle model. Interference effects provide information about electron correlations in a many electron system and are therefore of great interest in the investigation many body behaviour.

As an example, we consider the simplest case described by Fano (Fano 1961), in which transitions are considered from the ground state  $\Phi_g$  to both, a discrete state  $\varphi$  and a continuum  $\psi(E)$ . The configuration mixing of these two excited states, which are assumed to coincide in energy, gives rise to the so called *autoionizing* phenomenon. The discrete state mixes with the continuum via the perturbation operator  $\hat{H}^1$  which requires an ansatz for the solution of the total wavefunction  $\Psi(E)$  as a linear combination of the unperturbed discrete state  $\varphi$  and continuum functions  $\psi(E)$ .

$$\Psi(E) = a(E)\varphi + \int b(E, E')\psi(E')dE' \quad (2.40)$$

The exact coincidence of the energies  $\langle \varphi | \hat{H} | \varphi \rangle = E_0$  and  $\langle \psi(E) | \hat{H} | \psi(E) \rangle = E$  makes ordinary perturbation theory inadequate, so that the proper treatment required here to describe the autoionizing process is to diagonalize the energy matrix  $\langle \Psi(E) | \hat{H} | \Psi(E) \rangle$  in order to obtain the coefficients  $a(E)$  and  $b(E)$  and the new energy eigenvalue of the total wavefunction  $\Psi$  as the eigenstate of the system which is considered in this case. The diagonalization procedure is sufficiently simple to perform analytically which is also shown in Cowan's book (Cowan 1981 chapter 8.11). As a result, the discrete state acquires some properties of the continuum.

$$\phi(E) = \varphi + \mathcal{P} \int \frac{V(E')\psi(E')}{E - E'} dE' \quad (2.41)$$

However, the admixture is small unless the discrete resonance state  $\varphi$  is located near the ionization limit  $V(E)$  represents the configuration interaction matrix element  $\langle \psi(E) | \hat{H} | \varphi \rangle$  which describes the coupling strength between the two states

The new energy eigenvalue of the system is shifted due to the configuration mixing from  $E_0$  to  $E_0 + F(E)$  with  $F(E) = \mathcal{P} \int \frac{V^2(E')}{E-E'} dE'$  but the contribution of  $F(E)$  is usually very small due to the fact, that the principal integral vanishes if the integration is carried out symmetrically with respect to the singularity. Therefore the contribution of  $F(E)$  is usually neglected and the new energy eigenvalue corresponds to the energy value of the discrete unperturbed state  $\varphi$

Furthermore we obtain for the reduced dipole matrix (also called line strength)

$$\langle \Phi_g || r^{(1)} || \Psi(E) \rangle = a(E) \langle \Psi_g || r^{(1)} || \phi(E) \rangle + \frac{a(E)}{V(E)} (E - E_0) \langle \Phi_g || r^{(1)} || \psi(E) \rangle \quad (2.42)$$

with  $a(E) = V(E) ((E - E_0)^2 + \pi^2 V^4(E))^{-1/2}$ . According to eqn (2.33) where the absorption cross section is proportional to the square of the reduced dipole matrix, we obtain a *Beutler-Fano* photoabsorption profile

$$\sigma_{abs} = \frac{4\pi^2\alpha}{3} \hbar\omega \frac{1}{2J_i + 1} |\langle \Phi_g || r^{(1)} || \psi(E) \rangle|^2 \frac{(q + (E - E_0)/\Gamma)^2}{1 + ((E - E_0)/\Gamma)^2} \quad (2.43)$$

with the HWHM  $\Gamma = \pi V^2(E)$  and the *asymmetry* or *shape* parameter  $q = \frac{\langle \Phi_g || r^{(1)} || \varphi \rangle}{\pi V(E) \langle \Phi_g || r^{(1)} || \psi(E) \rangle}$ . The shape parameter  $q$  depends on the ratio of the reduced dipole matrix elements and on the coupling strength  $\langle \varphi | \hat{H} | \psi(E) \rangle = V(E)$

It should be pointed out here, that  $q$  and  $\Gamma$  are energy dependent parameters although they are usually considered to be constant over the resonance energy region of interest. Therefore resonance lines are very often parameterized through constant values of  $q$  and  $\Gamma$  in order to describe the electron correlations. One characteristic quantity is for example the autoionizing transition probability rate  $A^a$  of the discrete state  $\varphi$  into the continuum  $\psi$  with  $A^a[s^{-1}] = \tau^{-1} = 2\hbar^{-1}\Gamma$ .  $\tau$  represents the half life time of the discrete state  $\varphi$  before it decays into the continuum  $\psi$

The general form of eqn (2.43) can be illustrated for three different cases

- $|q| \rightarrow \infty$  Photoabsorption is only possible into the discrete state. The resonance line has the shape of an Lorentzian profile with  $\sigma_{abs} \propto f \times \Gamma \times \pi^{-1}/((E - E_0)^2 + \Gamma^2)$  which is symmetrical with respect to the resonance energy  $E_0$ .
- $q = 0$  In this case we obtain a window resonance profile with  $\sigma_{abs} \propto f \times ((E - E_0)/\Gamma)^2/(1 + ((E - E_0)/\Gamma)^2)$ . The dipole matrix element of the transition into the discrete state is zero and absorption is possible only into the continuum.
- $|q| \ll \infty$  We obtain an asymmetric profile due to the interference effect between the discrete and the continuum transition.

Figure 2.4 shows typical absorption profiles for all three cases. The amplitude is chosen differently in each case in order to allow an optimal display of all three curves simultaneously.

In summary, the photoabsorption cross section into a continuum, which interacts with the discrete excited state becomes resonantly enhanced via an admixture of the discrete state  $\varphi$  to the continuum  $\psi(E)$  with the fractional contribution  $a(E)$ . The result shows, that the contribution is spread out over a finite energy range  $2\Gamma$  which is determined by the coupling strength between the discrete state and the continuum which is represented by the configuration interaction matrix element  $V(E)$ .

In practice it is mostly sufficient to consider the Coulomb operator as the perturbation operator which causes autoionization processes. This is also comprehensible since in an illustrative picture of configuration interaction, the redistribution of the electron density is caused by the electron interactions represented by the Coulomb operator. It follows immediately from Chapter 2.2.1 that autoionizing transitions occur only into continuum states with the same quantum numbers  $L, S, J$  and  $M$ .

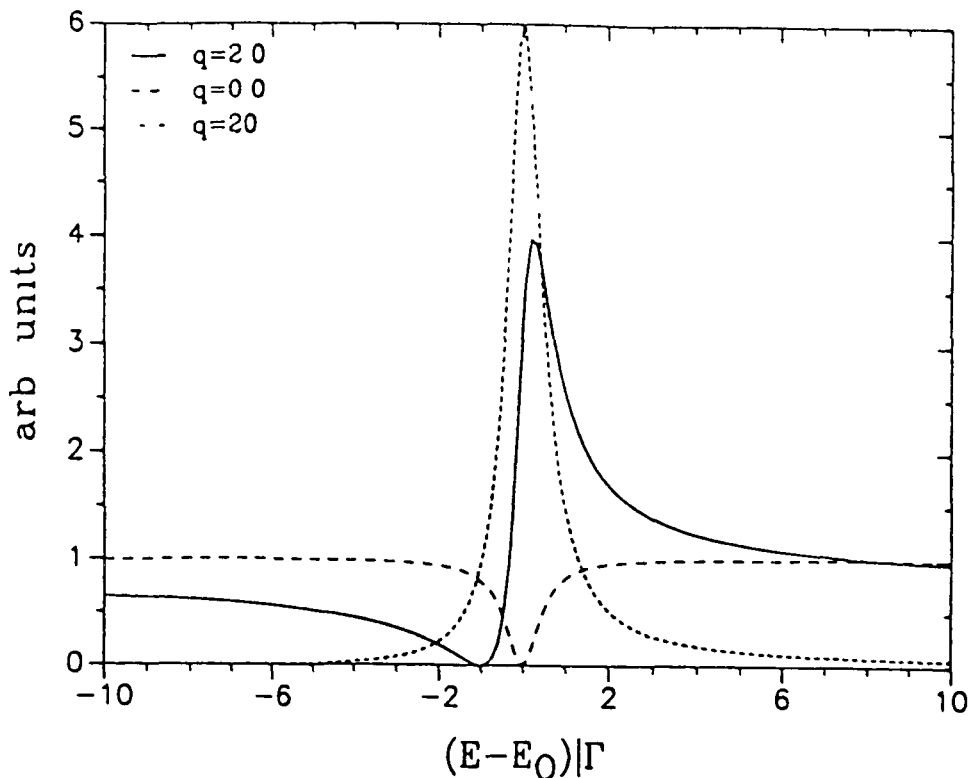


Figure 2.4 Fano profiles for different  $q$  values The amplitude is chosen differently in each case in order to allow an optimal display of all three curves simultaneously

In a CI-HF calculation the diagonalization of the energy matrix may lead to a considerable mixing between the states Hence discrete and continuum eigenstates are usually presented as a linear combination of the set of basis functions  $|b\rangle$  used in the multiconfiguration-HF approach

$$|\varphi\rangle = \sum_b |b\rangle \langle b|\varphi\rangle \quad (2.44)$$

$$|\psi(E)\rangle = \sum_{b'} |b'\rangle \langle b'|\psi(E)\rangle$$

The autoionizing rate  $A^a = 2\hbar^{-1}\pi |\langle \varphi|r^{-1}|\psi(E)\rangle|^2$  can then be expressed in the basis  $|b\rangle$

$$A^a = \frac{2\pi}{\hbar} \left| \sum_b \sum_{b'} \langle \varphi|b\rangle \langle b|r^{-1}|b'\rangle \langle b'|\psi(E)\rangle \right|^2 \quad (2.45)$$

with  $\langle b|r^{-1}|b'\rangle$  the Coulomb interaction between the basis states, which can be evaluated as a sum of weighted Slater integrals as discussed in Chapter 2.2.5.

Eqn (2.45) shows clearly, that strong CI have a large influence on the autoionization rate This is particularly well demonstrated for  $\text{La}^{3+}$ , where the  $4d^9 6p(1P)$

line has a negligible autoionization width ( $< 0.001\text{eV}$ ) in a single configuration approximation. This contradicts the experimental data, which shows a width of about  $0.2\text{eV}$ . The strong CI with the  $4d^9 4f(^1P)$  giant resonance causes the width of the  $6p(^1P)$  line to be broadened to about  $0.05\text{eV}$ . The remaining discrepancy between the experimental data and theory may be explained due to the neglect of the Auger width and limited experimental instrumental resolution, which is estimated to be  $0.15\text{eV}$ .

As an example of a resonance interacting with a single continuum, the double excitation  $1s^2(^1S_0) \rightarrow 2s2p(^1P_1)$  in  $Li^+$  is calculated within the Fano theory of resonant photoabsorption. The results are compared with experimental data by Carroll & Kennedy (1977), Kiernan (1994) and with recently published theoretical data by Sanchez & Martin (1990). At first glance, one might think that the theoretical treatment of a two electron system is relatively simple, but the fact that in this case both electrons are located in excited orbits, leads to highly correlated motions which means a strong deviation from a pure central field model. Therefore a proper treatment requires extended CI calculations with typically a couple of hundred configurations (Sanchez & Martin used 130 configurations in their calculation). In the following calculations, only 27 configurations were used and therefore the results can only be considered as an estimation particularly for the  $q$  value. It is worthwhile to mention here again, that the Fano parameters are actually energy dependent parameters and therefore not only difficult to calculate but also difficult to deduce from the experimental data specially if the parameters vary greatly with energy.

However, since the dipole operator is a single particle operator, double excitations (or shake up's) can only be treated within CI with single excited states. The following calculation included  $1snp$  configurations with  $n = 2, 3, \dots, 8$ ,  $2smp$  with  $m = 2, 3, \dots, 8$  and the  $1s\epsilon p$  continua with  $\epsilon$  in the energy range between  $5.2-5.5\text{ Ry}$ . The double excited  $2s2p(^1P_1)$  state can only decay into the  $1s\epsilon p(^1P_1)$  continuum, which can be reached directly from the ground state via dipole exci-

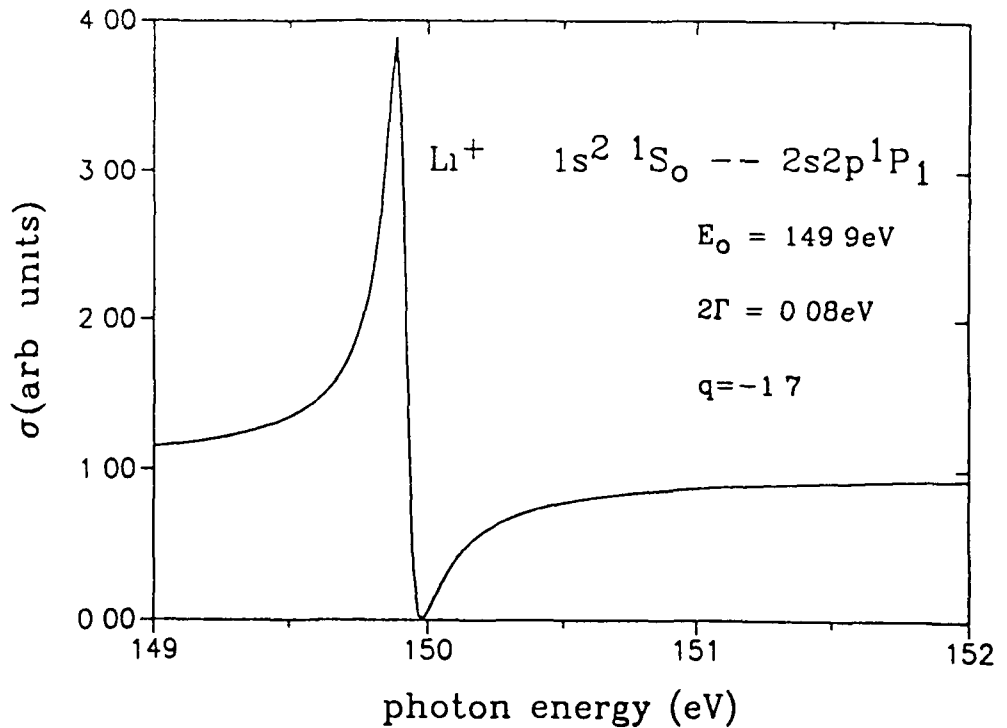


Figure 2.5 *Beutler-Fano photoabsorption profile for the  $1s^2(^1S_0) \rightarrow 2s2p(^1P_1)$  double excitation in  $Li^+$*

tation Both channels interfere to give a pronounced Beutler-Fano profile The results are presented in Figure 2.5 and Table [2.11]

## 2.4 Many-Body Effects

The independent particle model described in a previous subchapter, assumes that once the electrons are placed in their single particle atomic orbitals, they move and respond thereafter independently This is certainly not true in a many electron system One improvement of the IPA was the previously discussed orbital relaxation effects Another improvement can be made by considering the optical response of the electron cloud in an atom under the influence of an external field Independent particles respond by polarizing in accordance to an impressed electric field to create a net dipole moment This effect is well known in the static approximation as the *Stark effect* where the perturbation theory in second order leads to an admixture of excited states in order to constitute a nonspherical elec-



Table 2.11 Fano parameters of the  $1s^2(^1S_0) \rightarrow 2s2p(^1P_1)$  resonance line in  $Li^+$

	this work	Carroll & Kennedy	Kiernan	Sanchez & Martin
$E_0[eV]$	149.91	150.29	150.28	150.295
FWHM $2\Gamma[eV]$	0.08	0.075	0.09	0.0622
$q$	-1.7	-1.5	-1.8	-2.2
$A^a[10^{13}s^{-1}]$	12.55			
$V(E)[Ry]$	0.031			
$d^{dis}[ea_0]$	0.0037			
$d^{cont}[ea_0]$	-0.022			

tron distribution. Now taking the residual Coulomb interactions into account, the polarized electron cloud establishes its own electric field. The electrons rearrange in order to accommodate the total force acting on them. Therefore the electrons must redistribute themselves in response to the sum of the external and internal fields. The internal field screens or antiscreens the external field which depends mainly on the driving frequency of the external field and on how the electrons can respond to the perturbation, more precisely the spatial overlap between the occupied and unoccupied electron orbitals and their energy difference. As a result, the oscillator strength is very often shifted towards higher energies than those predicted from the IP model. This is the most characteristic feature in the optical response theory (Wendin 1984).

In the following discussion I shall be concerned with two classes of many body effects

- *dynamical polarization*, as already introduced qualitatively
- *self energy*. The typical many-body theories RPAE and TDLDA commonly use frozen core orbitals. The self energy calculated within the MBPT manifests itself most commonly in a dynamical relaxation (which is to a certain extent equivalent to the orbital relaxation discussed within the HF theory)

and subsequent decay of the hole (Auger decay) produced in photoabsorption

Polarization type many body effects are incorporated in the Random Phase Approximation with Exchange (RPAE) and the Time Dependent Local Density Approximation (TDLDA) which are closely related and which are introduced briefly in the next two subsections. The self energy which is calculated within the Many Body Perturbation Theory (MBPT) for the  $4d^{-1}$  hole state in  $La^{3+}$  is also discussed in a more qualitative manner as far as it is of relevance for the results presented in this work.

### 2.4.1 RPAE

The polarization of the atomic charge density in response to a time dependent external field is described by a time dependent wavefunction (Amusia 1990)

$$\psi(t) = e^{-E_0 t} \det\{\phi_i(r, t)\} \quad (2.46)$$

with the single particle orbitals

$$\phi_i(r, t) = \phi_i(r) + \left( \sum_{m>F} x_{mi} \phi_m(r) \right) e^{-i\omega t} + \left( \sum_{m>F} y_{mi} \phi_m(r) \right) e^{i\omega t} \quad (2.47)$$

which is used in a time dependent variational procedure with a Hamiltonian describing the atom and the external field. The minimization of the time dependent energy functional keeping only terms linear in  $x_{mi}$  and  $y_{mi}$  yields after a few intermediate steps to the linearized Time Dependent Hartree-Fock (TDHF) equations (Amusia 1990) represented by

$$(E_m - E_i - \hbar\omega)y_{mi} + \sum_{\substack{n>F \\ j \leq F}} [\langle ni | \hat{V} | jm \rangle y_{nj} + \langle nj | \hat{V} | mn \rangle x_{nj}] + \langle i | \hat{r} | m \rangle = 0 \quad (2.48)$$

(only one equation is shown here, the second one can be obtained by replacing  $y_{mi}$  through  $x_{mi}$ , taking the complex conjugate Coulomb matrix element and

using a negative frequency) The  $x_{m_i}$  and  $y_{m_i}$  are coefficients, which are obtained by solving the TDHF equation. If one defines now the RPAE amplitude as the matrix element of a frequency dependent effective dipole operator  $\langle i|\hat{R}(\omega)|m \rangle = (E_i - E_m - \hbar\omega)y_{m_i}$  and  $\langle m|\hat{R}(\omega)|i \rangle = -(E_i - E_m + \hbar\omega)x_{m_i}$  eqn (2.48) can be written as (Amusia 90)

$$\langle m|\hat{R}(\omega)|i \rangle = \langle m|\hat{r}|i \rangle + \sum_{\substack{n>F \\ j<F}} \left[ \frac{\langle n|\hat{R}(\omega)|j \rangle \langle m_j|\hat{V}|in \rangle}{E_j - E_n + \hbar\omega + i\delta} + \frac{\langle j|\hat{R}(\omega)|n \rangle \langle mn|\hat{V}|ij \rangle}{E_j - E_n - \hbar\omega - i\delta} \right] \quad (2.49)$$

with  $\langle mn|\hat{V}|ij \rangle$  the Coulomb (direct and exchange) CI integral and  $\langle n|\hat{R}(\omega)|j \rangle$  the RPAE amplitude for any intermediate transition  $j \rightarrow n$  including  $m \rightarrow i$ . The positive infinitesimal  $\delta$  insures, that the response of the electron system to the external perturbation is causal. Comparing  $\langle m|\hat{R}(\omega)|i \rangle$  with  $\langle m|\hat{r}|i \rangle$ , it becomes obvious, that the first matrix element can be treated as an effective field matrix element (in length form) that leads to an electron transition from state  $|m \rangle$  to state  $|i \rangle$ . Physically one can imagine, that the atom gets deformed and polarized by the external electromagnetic field, so that the actual field acting upon the single electrons differs from the external one and is considerably determined by the polarizability of the atomic electron shells. If we replace now the dipole operator in eqn (2.33) by the effective one, we obtain the photoabsorption cross section  $\sigma^{RPAE}$  which takes the dynamical many body polarizability of the atom in response to the external field into account.

The second important quantity is the effective interelectron interaction  $\Gamma(\omega)$  which can be obtained in analogy to the effective field (Amusia 90)

$$\langle ml|\hat{\Gamma}(\omega)|ik \rangle = \langle ml|\hat{V}|ik \rangle + \sum_{\substack{n>F \\ j<F}} \left[ \frac{\langle nl|\hat{\Gamma}(\omega)|jk \rangle \langle m_j|\hat{V}|in \rangle}{E_j - E_n + \hbar\omega + i\delta} + \frac{\langle jk|\hat{\Gamma}(\omega)|nl \rangle \langle mn|\hat{V}|ij \rangle}{E_j - E_n - \hbar\omega - i\delta} \right] \quad (2.50)$$

The correlational term determines the difference between the effective and the Coulomb interelectronic interaction caused by the polarization of the atomic electron cloud. The effective interelectron interaction is an important quantity e.g. for calculating the life time of discrete transitions due to autoionization (see chapter 2.3.1). Eqn (2.49) and eqn (2.50) can be solved iteratively and therefore the RPAE is also called a *self consistent field generalization of the linear response formalism* (Wendin 1976).

The 4d photoabsorption spectrum of  $\text{La}^{3+}$  was calculated with the RPAE method where the partial cross sections of the 5 interacting transitions  $5p \rightarrow \epsilon(s, d)$ ,  $5s \rightarrow \epsilon p$  and  $4d \rightarrow \epsilon(p, f)$  were obtained. All cross sections exhibit in the  $4d \rightarrow 4f$  excitation region a strong giant resonance. The sum of all partial cross sections represents the total ion yield which is in this case equivalent to the photoabsorption yield measured in this work.

## 2.4.2 TDLDA

The Hartree-Fock equation has to be solved in an iterative procedure since its exchange potential is of a nonlocal nature. However ground state properties of an atom can be well described within the density functional theory, with use of a local potential in the so called *Local Density Approximation* (LDA). The LDA has its applications in many areas of physics such as solid-state, fluid or molecular physics in order to describe the electronic ground state energy with its appropriate electron density and chemical potentials.

The foundation of the density functional formalism was laid by Hohenberg & Kohn (1964) who showed that in a many electron system which can be described as an inhomogenous electron gas, the ground state energy is a functional of the electron density  $E_0[n]$  and attains its minimum when the density achieves its exact ground state value (the so called Hohenberg Kohn theorems I and II). In other words, the electron density is treated as the fundamental quantity in the

density functional theory Although the exact functional is unknown, Kohn & Sham (1965) showed, that the energy functional can be written in the form

$$E_o[n] = T[n] + \int_V v(\mathbf{r})n(\mathbf{r})d\mathbf{r}^3 + \int_V \int_{V'} \frac{n(\mathbf{r})n(\mathbf{r}')}{|\mathbf{r} - \mathbf{r}'|} d\mathbf{r}^3 d\mathbf{r}'^3 + E_{xc}[n] \quad (2.51)$$

where the only unknown quantity is the exchange-correlation energy functional  $E_{xc}[n]$   $T[n]$  is the exact kinetic energy functional for the noninteracting electrons,  $v(\mathbf{r})$  denotes the Coulomb potential from the nucleus and the third term represents the classical electrostatic Coulomb interaction between the electrons

Furthermore Kohn & Sham (Sham 1965) described the exchange energy functional  $E_{xc}[n]$  in the so called *Local Density Approximation* (LDA)

$$E_{xc}[n] = \int n(\mathbf{r})\epsilon_{xc}[n](\mathbf{r})d\mathbf{r}^3 \quad (2.52)$$

where  $\epsilon_{xc}[n](\mathbf{r})$  is the averaged approximated exchange-correlation energy per particle The variational derivation of the energy functional leads to the *Kohn-Sham* equation (Scherz 1990)

$$[-\Delta + v(\mathbf{r}) + v_H[n](\mathbf{r}) + v_{xc}[n](\mathbf{r})]\psi_i(\mathbf{r}) = \epsilon_i\psi_i(\mathbf{r}) \quad (2.53)$$

with  $v_{xc}[n](\mathbf{r}) = \epsilon_{xc}[n](\mathbf{r}) + \frac{d\epsilon_{xc}[n]}{dn}n(\mathbf{r})$  The Kohn-Sham equation has to be solved in order to obtain the LDA orbitals from which the electron density can be deduced The (R)TDLDA results presented in this work were calculated with use of the *Gunnarsson-Lundqvist exchange-correlation potential* (Gunnarsson & Lundqvist 1976)  $v_{xc} = -\frac{1.222}{r_s} - 0.0666 \ln\left[1 + \frac{11.4}{r_s}\right]$  with  $r_s$  the radius of the Wigner-Seitz sphere

The correlation part of  $v_{xc}[n]$  is obtained by undertaking a careful analysis of the homogenous electron gas using a linear combination of Slater determinants as a wavefunction of the total electron system

The photoabsorption cross section in the Local Density Approximation as an independent particle model can be obtained from *Fermi's golden rule* (eqn (2.31)) using LDA orbitals instead of HF wavefunctions

The Time Dependent Local Density Approximation (TDLDA) is a time dependent generalization of the density functional formalism within the Local Density Approximation which is amenable to calculating the dynamical response to an external field (Zangwill & Soven 1980, Zangwill 1983, Zangwill & Liberman 1984, Zangwill 1987). The general idea is, that an external field (considered here in length form) induces a frequency dependent perturbation in the electron density  $\delta n(\mathbf{r}, \omega)$  which may be written in a linear approximation as

$$\delta n(\mathbf{r}, \omega) = \int \chi(\mathbf{r}, \mathbf{r}', \omega) \mathbf{r}' d\mathbf{r}'^3. \quad (2.54)$$

The induced density  $\delta n$  and the external field are related via a position and frequency dependent complex susceptibility  $\chi(\mathbf{r}, \mathbf{r}', \omega)$  given in (Zangwill & Soven 1980). Furthermore the density in eqn.(2.54) reflects the response to the external field alone. However as the electrons redistribute themselves in the atom, they interact with each other via the repulsive Coulomb force and produce an internal field via the induced Coulomb potential

$$\delta V_c(\mathbf{r}, \omega) = e \int \frac{\delta n(\mathbf{r}', \omega)}{|\mathbf{r} - \mathbf{r}'|} d\mathbf{r}'^3 \quad (2.55)$$

and an induced exchange-correlation potential

$$\delta V_{xc}(\mathbf{r}, \omega) = \left. \frac{\partial V_{xc}}{\partial n} \right|_{n=n_0} \delta n(\mathbf{r}, \omega). \quad (2.56)$$

The internal field can be superimposed on the external one to give an effective driving field. The new effective field variable  $R(\omega)$  then replaces the external one  $r$  in eqn.(2.54) in order to calculate the new deviation in the electron density. The procedure is repeated until self consistency is achieved.

The TDLDA cross section may then be obtained from eqn.(2.31) by replacing the dipole operator  $\hat{r}$  by  $\hat{R}(\omega)$  and by using LDA orbitals as single particle states.

In summary RPAE and TDLDA incorporate polarization effects as a mean field theory in the sense, that the dynamical many-body polarization is built into a frequency dependent effective driving field which replaces the external one in

the dipole transition matrix. In fact, it can be shown, that the RPAE and the TDLDA amplitude are equivalent if one replaces the single particle HF orbitals by their counterparts in the LDA, and if one disregards the difference in the expression for the exchange potential (Zangwill 1981)

### 2.4.3 Self Energy

In this section, I would like to address another class of many electron correlations which can have a large influence on the photoabsorption behaviour for elements like the Ba, La and lanthanides. As already discussed to some extent the consideration of orbital relaxation may play an important role in the calculation of transition energies, thresholds and photoabsorption cross sections. The physics of the problem may be presented in the following manner taking the 4d photoabsorption of  $\text{La}^{3+}$  as an example. The  $4d^{-1}$  hole created in photoabsorption relaxes by attracting the surrounding electrons with a subsequent Auger decay into a lower ion stage. The resulting rearrangement in the electron charge distribution screens the  $4d^{-1}$  hole from the outgoing continuum electron, which therefore experiences a different potential from that in the frozen core approximation. Relaxation effects are to some extent directly taken into account in the HF self consistent field procedure of the Cowan codes in calculating electron orbitals and their appropriate potentials of  $4d^{-1}$  hole configuration in a separate run which leads to the result, that the  $4d^{-1}$  hole and the 4d particle orbital are not equivalent. However the RPAE and the TDLDA models use usually frozen core orbitals. In order to take here relaxation effects into account, one constructs the relaxed  $4d^{-1}$  orbital in a multiconfiguration expansion with configurations describing different hole states. In the case of  $\text{La}^{3+}$  the following configurations were considered (Ivanov 1994)  $4d^{-1}5p^{-1}np,\epsilon p$ ,  $4d^{-1}5s^{-1}ns,\epsilon s$  and  $4d^{-2}nd,\epsilon d$  which represent monopole excitations or simpler *shake up*'s since the transferred angular momentum  $\Delta l = 0$ . Furthermore multipole contributions may be included

as e.g. the dipole excitations with the transferred angular momentum  $\Delta l = 1$   $5p^{-2}n(s, d), \epsilon(s, d), 5p^{-1}5s^{-1}np, \epsilon p$  and  $4d^{-2}n(p, f), \epsilon(p, f)$ . From the many body point of view, the relaxed  $4d^{-1}$  orbital is constructed via mixing with other more complicated hole states. One then can imagine that the initially created  $4d^{-1}$  hole spends a part of its time (during the relaxation process) in other particle hole states until it finally decays.

The quantity which characterizes the interaction part of the  $4d^{-1}$  quasi hole is the so called *self energy*  $\Sigma_{4d}(E) = \langle 4d | \Sigma(E) | 4d \rangle$ . It describes the deviation from the energy of an IPA hole state which occurs when the residual Coulomb interaction between the hole and its neighbors is restored. The analytical expression for the self energy is calculated in second order Brillouin-Wigner perturbation theory as a *Many Body Perturbation Theory* (MBPT) and is given for the  $4d^{-1}$  hole in Chapter 3.2.3 which presents the RPAE/MBPT results for  $\text{La}^{3+}$ . The real part of  $\Sigma_{4d}$  gives the energy shift due to dynamical relaxation, the imaginary part, which is present if continuum states are included, gives the life time of the hole due to Auger decay.

In order to investigate the 4d photoabsorption spectrum of  $\text{La}^{3+}$  from a many-body point of view, a combination of RPAE and MBPT was used (Ivanov et al 1993). The self energy  $\Sigma_{4d}$  was calculated in order to obtain the energy shift and the life time due to relaxation and Auger decay. The  $4d \rightarrow nf, mp$  transition amplitudes and widths were calculated within the RPAE, the transition energies corrected by the amount of  $\text{Re}\Sigma_{4d}$  and  $\text{Im}\Sigma_{4d}$  added to the autoionizing width. Radiative transitions, which may give in principle an additional contribution to the  $4d^{-1}$  life time have not been considered here since their contributions to the total width is negligible small. The combined calculations take therefore the following many electron correlations into account: *dynamical polarization* of the electron cloud as a response to the external perturbation and *dynamical relaxation* (Auger decay included) in form of rearrangement processes in the electronic shell structure after creating a  $4d^{-1}$  hole. It will be shown, that these type of many-



body effects are strongly present in the photoabsorption behaviour of  $\text{La}^{3+}$  and gold

## Chapter 3

### Near Threshold 4d

### Photoabsorption in Xenon-like

### Lanthanum

Photoabsorption of the inner 4d shell for  $\text{La}^{3+}$  was studied using the dual laser plasma technique. A dramatic strong and broad  $4d^9 4f(^1P)$  giant dipole resonance was observed. The  $4d^{10} \rightarrow 4d^9 nf, np$  transitions have been analysed using a Hartree-Fock configuration interaction technique and the Many Body Perturbation Theory with particular attention given to the strong term dependence for the predicted dominant  $4d^9 4f(^1P)$  term which gives evidence of strong polarization effects. The experimental results fit very well into the picture of the partial 4f ( $^1P$ ) orbital collapse phenomenon for the Xe-like ions. Relativistic Time Dependent Local Density Approximation calculations have been performed for  $\text{Ba}^{2+}$  and  $\text{La}^{3+}$  and compared with the corresponding experimental data.

### 3.1 4d-Photoabsorption of Xe, Ba, La and the Rare Earths

The study of the inner shell excitation mechanism of atoms with atomic number  $Z = 54 - 70$ , in the photon energy region between  $100 - 200\text{eV}$ , has been of great interest for over two decades now, since their photoabsorption spectra show spectacular strong, broad and asymmetric profiles, the so called *giant resonances* (Radke 1979a,b, Mansfield & Connerade 1984, Connerade & Pantelouris 1984) In following their photoabsorption behaviour along the periodic table, one realizes that the dominant resonance lies above the 4d threshold for the lighter elements ( $Z < 60$ ), moves gradually towards threshold with increasing  $Z$ , passes and sinks below the the 4d limits with  $Z \geq 64$ , where the shape of the main resonance shows the characteristic asymmetry of a Beutler-Fano profile (Sonntag & Zimmermann 1992)

The excitation process therefore was described by the transition of a 4d electron into the  $4d^9(4, \epsilon)f$  states which compete with each other along the sequence and where the dominant process was found to be the continuum transition for the lighter elements and the discrete transitions for the heavier ones The competition can be explained in terms of the different localisation of the excited 4f orbital along the sequence resulting from the attractive electrostatic and repulsive centrifugal forces of the many electron system Hartree-Fock calculations for Xe showed, that the effective local potential for the excited  $(4, \epsilon)f$  orbital consists of two wells, an inner well separated from an outer one by a potential barrier (Cooper 1964) The outer well is broad and shallow in contrast to the inner one which is narrow and deep The centrifugal barrier keeps the low energy  $(4, \epsilon)f$  orbitals above the outer well far outside the core, whereas the 4d wavefunction is located in the inner well region. The resulting small overlap between both orbitals causes the bulk of oscillator strength to be transferred into the higher energy continuum states  $4d^{10} \rightarrow 4d^9\epsilon f$ , which explains the delayed onset of absorption beyond the

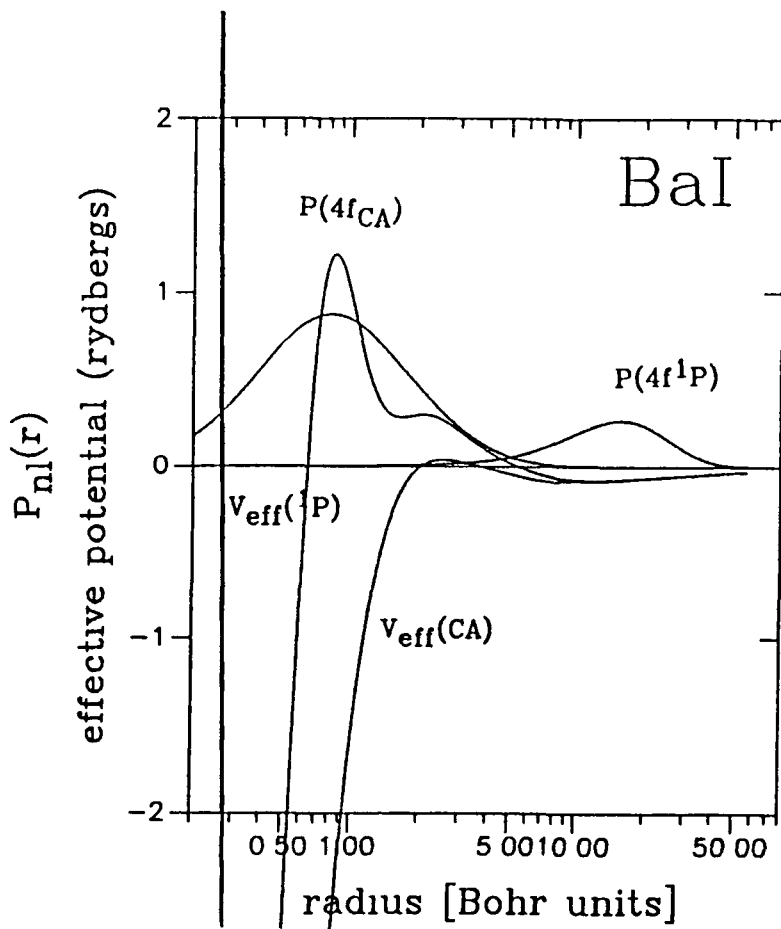


Figure 3.1. Plot of the configuration average (CA)HF  $4f$  and the LS term dependent  $4f(^1P)$  local single electron potentials and radial wavefunctions for the  $4d^9 4f$  configuration in Ba. In the CA model, the  $4f$  wavefunction is collapsed into the inner well of its appropriate potential, whereas in the term dependent model, the potential of the  $4f(^1P)$  shows a pronounced potential barrier between the inner- and outer well and the radial wavefunction is located in the outer well far outside the core (see also Griffin et al 1987)

#### 4d-thresholds

For Ba, where the shape of the absorption profile is similar to that of Xe, the explanation is different. HF calculations of the  $4f$  orbital and its appropriate effective potential were carried out in the same manner as applied for Xe which show that the  $4f$  wavefunction is *collapsed* into the inner well of the double valley potential (see Figure 3.1). The dramatic increased spatial overlap with the  $4d$  ground state orbital results in the  $4d$ - $4f$  electrostatic interaction being the dominant interaction. It follows, that the  $4d^9 4f$  configuration is almost purely LS

coupled and the oscillator strength of the optically allowed  $4d^{10}(^1S) \rightarrow 4d^9 4f(^1P)$  transition is therefore much larger than the intercombination transitions into the triplet states  $^3D, ^3P$ . Due to the same strong electrostatic exchange effects, the  $^1P$  state is pushed up far above the 4d thresholds, whereas the triplets are located below the limits. Ederer et al (1975) therefore associated the *giant resonance* in Ba with the  $4f(^1P)$  level, supported by a model, which was proposed by Dehmer et al (1971) to explain the *giant resonance* in the solid rare earths spectra, in which the discrete excitation  $4d \rightarrow 4f$  is followed by an autoionization process into its own continuum.

Hansen et al (1975) came to somewhat different conclusions based on *LS* term-Dependent Hartree-Fock (*LSD*-HF) calculations. He showed, that in the *LSD* approach, the  $4d^9 4f(^1P)$  level is actually located below the 4d thresholds. Similar calculations by Fliflet et al (1975) showed, that the corresponding transition has almost no oscillator strength. This can be explained by calculating the effective central potential and the radial 4f wavefunction of the  $4d^9 4f(^1P)$  term, which shows, that in the *LS* term-Dependent model, the 4f wavefunction looks significantly different from the one obtained in a center of gravity Hartree-Fock (c-g HF) calculation, and is located above the outer well of the double valley potential as shown in Figure 3.1 (see also Griffin & Pindzola 1983). The interpretation of the photoabsorption spectrum of Ba therefore is similar to the case of Xe, that the *giant resonance* actually represents the transition into the  $4d^9 \epsilon f(^1P)$  continuum. Detailed calculations for the 4d photoionization in Ba by Wendin (1973) and Ba and La by Amusia et al (1975, 1976, 1980, 1989, Amusia & Sheftel 1976) based on the RPAE method came into close agreement with the experimental data.

The change in shape of the absorption profile as one follows the rare earth sequence along the periodic table (see Figure 3.3) may therefore be explained due to the term dependence of the orbital *collapse*. The center of gravity 4f orbital of the  $4d^9 4f^{n+1}$  configuration is already collapsed abruptly between Xe and Ba, but

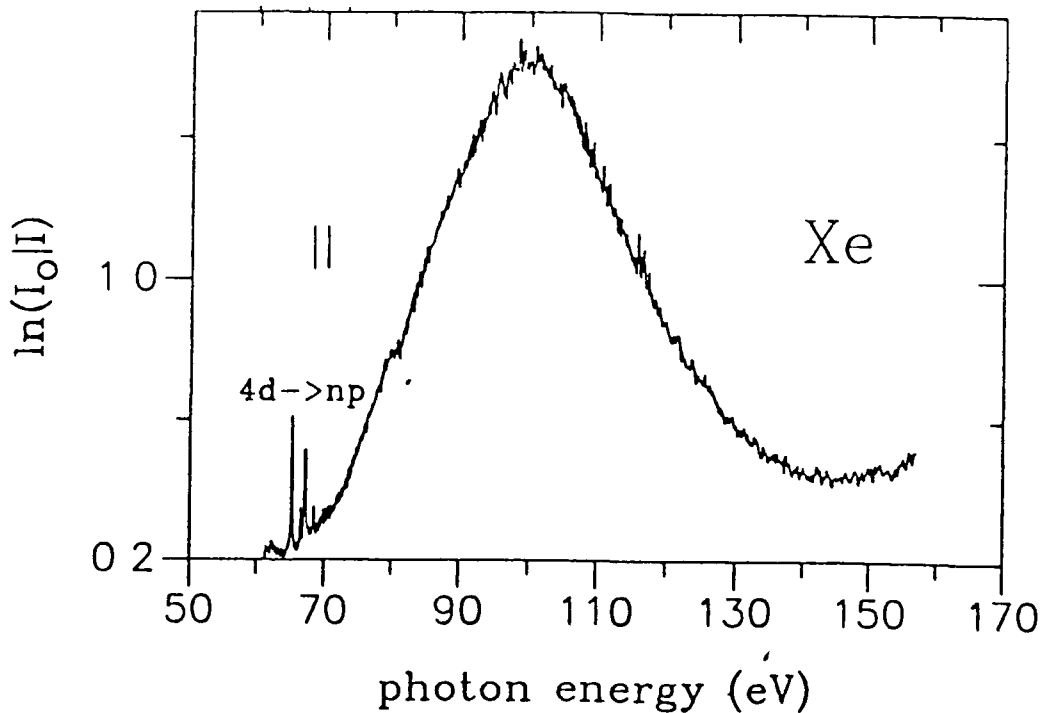


Figure 3.2 Photoabsorption spectrum of Xe in the 4d excitation region recorded with the dual laser plasma (DLP) facility

the wavefunction collapse of the states, which can be optically excited from the ground state under  $LS$  coupling conditions, is of a different kind and may not be completed before the 4f shell is filled. However, a quantitative analysis for these elements is rather difficult due to the high degree of complexity in the angular momentum coupling properties of the  $4f^n$  electrons.

The *giant resonance* phenomenon in the 4d excitation region again strongly attracted theoretical interest (Connerade & Mansfield 1982, Nuroh et al 1982, Connerade 1983, Cheng & Froese Fischer 1983, Cheng & Johnson 1983, Clark 1984), when Lucatorto et al (1981) presented their classic spectra of the measured Ba, Ba<sup>+</sup> and Ba<sup>2+</sup> photoabsorption cross sections. While the shape of the Ba<sup>+</sup> spectrum is rather similar to that of Ba, the Ba<sup>2+</sup> spectrum exhibits pronounced line structure with four almost equally strong resonance lines in the discrete energy region below the 4d thresholds. This was very surprising since following the discussion of the orbital *collapse* theory described for the neutral rare earth elements, one would expect, that only the  $4f(1P)$  orbital of the  $4d^9 4f$  configuration

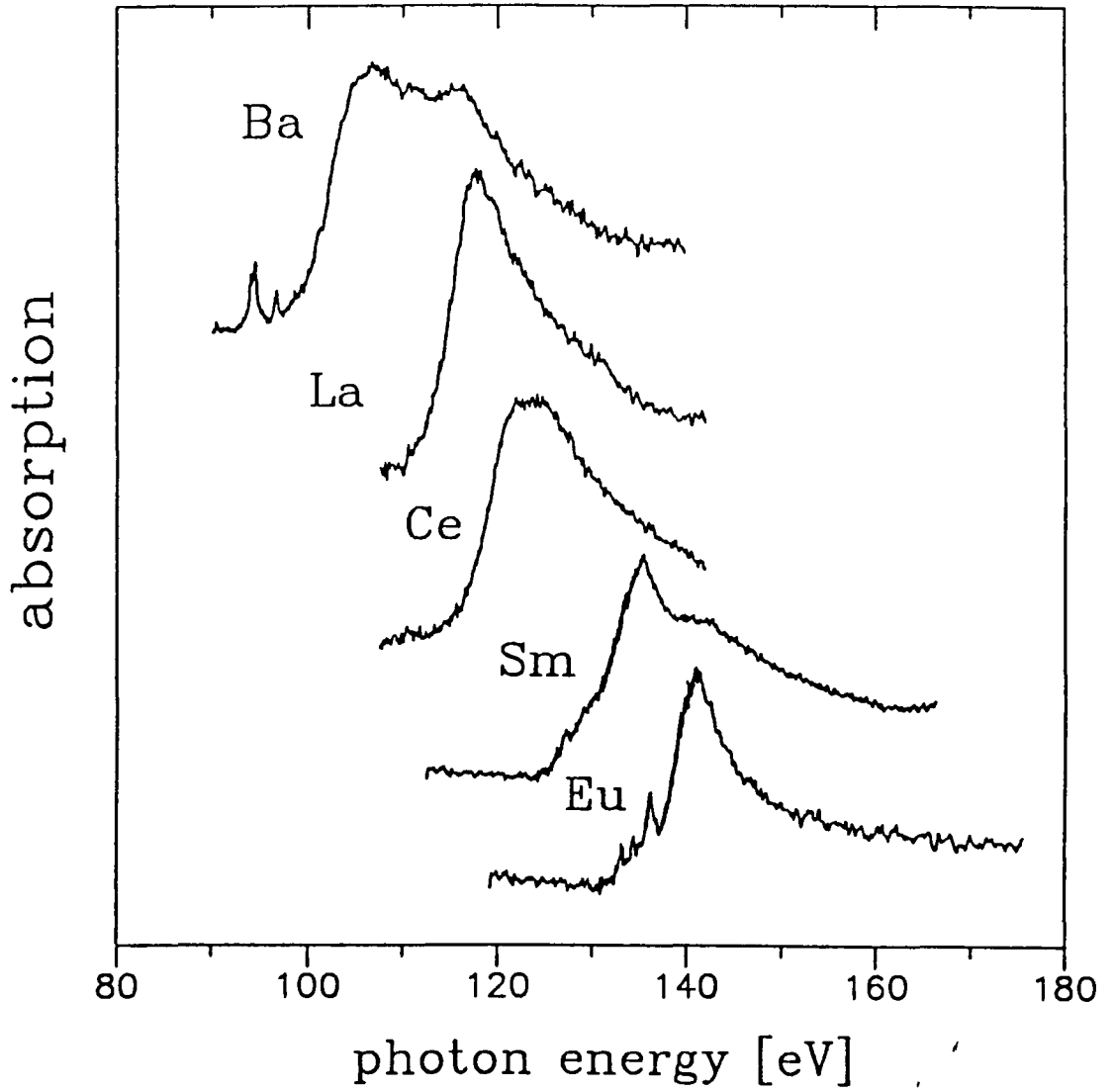


Figure 33 Photoabsorption spectrum of Ba, La, Ce, Sm and Eu in the 4d excitation region using the dual laser plasma (DLP) technique

is *collapsed* while the wavefunctions of the higher Rydberg members remain in the outer region of the centrifugal barrier. As a result, only one line was expected to be observed. But detailed calculations by Connerade & Mansfield (1982) employing term dependent Hartree-Fock wavefunctions showed only an enhanced overlap between the 4d and  $nf$  ( $^1P$ )( $n \geq 5$ ) orbitals for  $Ba^{2+}$  which they described as a *second kind of wavefunction collapse*. Based on Hartree-Slater calculations, which included configuration mixing, they concluded that the prominent discrete lines are associated with the  $4d \rightarrow 5f, 6f,$  transitions, while the  $4f(^1P)$  state was found to lie above the 4d thresholds.

Further theoretical investigations based on other atomic models came to different conclusions. Clark (1984) used the MCHF code to analyse the discrete transition sequence successfully and Nuroh et al (1982) utilized the Time Dependent Local Density Approximation (TDLDA) to study the Ba,  $Ba^+$  and  $Ba^{2+}$  isonuclear sequence. Cheng & Froese Fischer (1983) and Cheng & Johnson (1983) analysed the  $Ba^{2+}$  spectrum when they studied the term dependence of the orbital collapse of the excited  $nf$  wavefunctions of Xe like Cs, Ba, La and Ce ions, where the calculations are not complicated by the change of the electronic configuration. Although a straight forward interpretation is rather difficult, Clark (1984) and Cheng & Froese Fischer (1983) independently identified the four strongest observed lines as the  $4d \rightarrow nf(^1P)$  transitions with  $n = 4, 5, 6$  and  $7$ . Cheng & Froese Fischer (1983) also showed, that the  $4d^9 4f(^1P)$  resonance line becomes unequivocally the strongest line among the Rydberg members in following the Xe isoelectronic sequence from  $Ba^{2+}$  to  $La^{3+}$ .

Stimulated by the theoretical interest and the lack of experimental photoabsorption data for Xe like ions, the photoabsorption behaviour of a laser produced lanthanum plasma was investigated photographically (Hansen et al 1989). The 1.5J output pulse of a Q-switched ruby laser was optically divided and focussed onto suitable targets to produce a backlighting XUV plasma light source and an absorbing lanthanum plasma. The plasma conditions of the absorbing lanthanum



column could be varied by changing the focusing conditions of the laser pulse on the target. The recorded spectrum clearly showed absorption lines which were successfully identified as belonging to the  $\text{La}^{3+}$  ion, however the predicted dominant  $4d^9 4f(^1P)$  resonance line was not observed. This was explained by the assumption, that its autoionizing width is so large and spread out over a too extensive wavelength range to make it visible on a photographic plate with a limited dynamic range.

In order to clarify the discrepancy between theory and experiment we reinvestigated the photoabsorption spectrum of a laser produced lanthanum plasma using the recently installed Dual Laser Plasma (DLP) facility with photoelectric detection.

### 3.2 4d-Photoabsorption in $\text{La}^{3+}$

The photoabsorption spectrum of  $\text{La}^{3+}$  in the 4d excitation region is shown in Figure 3.4. Most striking is the strong resonance line at the photon energy of 118.9 eV which must be associated with the predicted dominant  $4d^9 4f(^1P)$  term, and the reduction of the continuum absorption background. The calculated triplet state  $4d^9 4f(^3D)$  (Hansen et al 1989) is also clearly recognizable at 102.1 eV, while the  $4d^9 4f(^3P)$  term was not observed due to the signal to noise ratio in the spectra. The higher Rydberg states  $4d^9 n f$  with  $n = 5, 6, \dots, 9$  are in good agreement with the previous results (Hansen et al 1989). For a better understanding of the measured spectrum, intrachannel CI-HF, MBPT/RPAE and TDLDA/RTDLDA calculations have been performed for  $\text{La}^{3+}$ . Each of them incorporates a different model and technique for the description of the *giant resonance* and the results are discussed and compared with the experimental data in the following subsections.

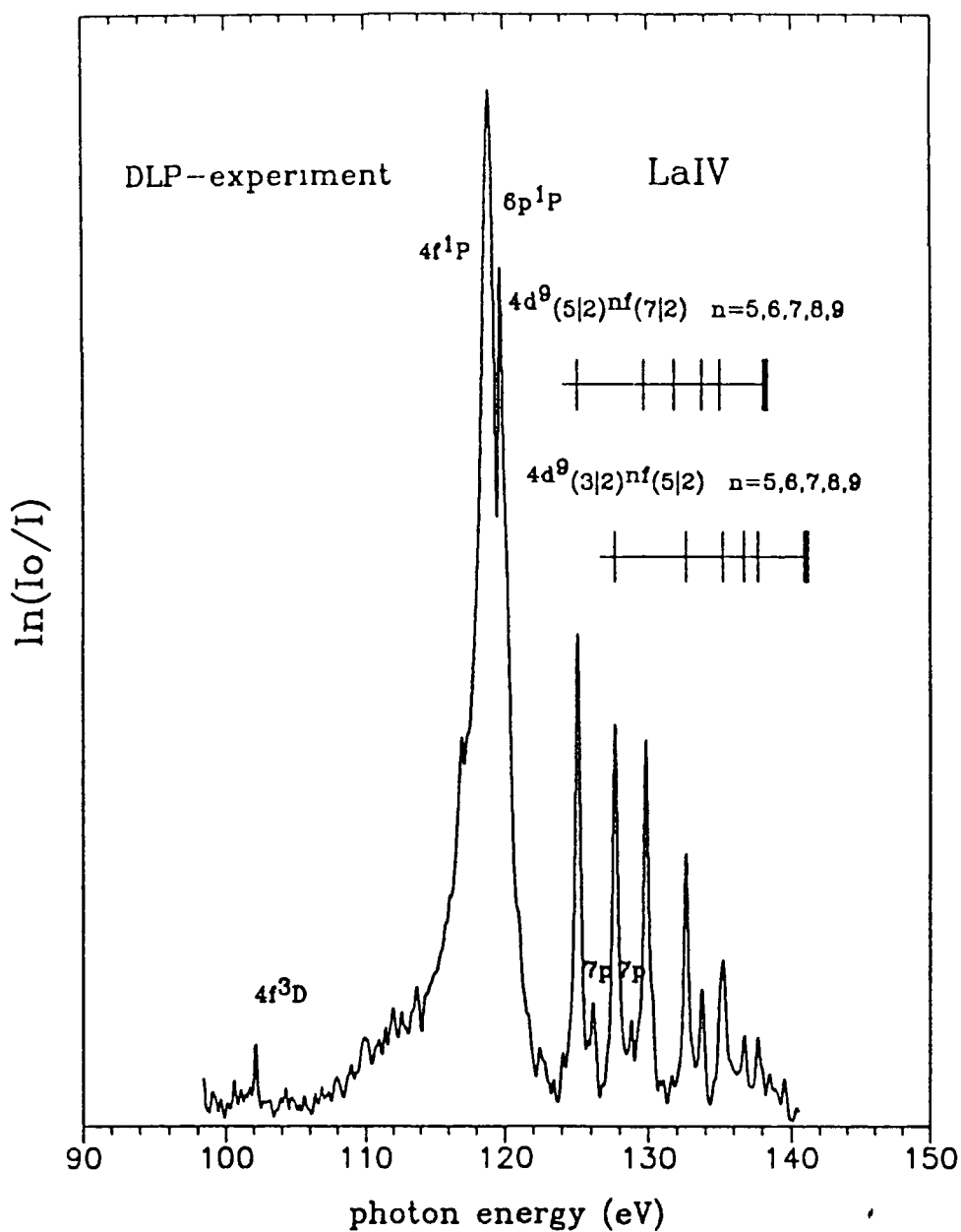


Figure 3.4 Photoabsorption spectrum of  $La^{3+}$  in the 4d excitation region using the Dual Laser Plasma (DLP) technique. The thresholds  $4d^9_{(5/2),(3/2)}$  deduced from the experimental data are  $138.2 \pm 0.2$  eV and  $141.1 \pm 0.2$  eV.

### 3.2.1 Configuration Interaction Hartree-Fock Calculations

In order to interpret the spectra, Hartree-Fock calculations were carried out using the Cowan codes written by Cowan (1968, 1981), in which relativistic corrections of the mass-velocity and the Darwin term were taken into account as well as some correlation corrections to the configuration average energy. From the *RCN* code, the corrected configuration average energies, the Slater integrals and the spin-orbit parameters were obtained, which were used for diagonalization of the CI-energy matrix and the construction of the eigenvector components using the *RCG* programme. The *RCN* code also provided the radial integrals between different configurations of discrete and continuum states of the same parity in order to perform configuration interaction (CI) calculations and calculations of autoionization rates using Fano's perturbation approach as described by Cowan (1981).

The results of the single configuration *ab initio* calculations gave satisfactory agreement with respect to the energy position of the observed lines except for the  $4d^9 4f(^1P)$  term, which is predicted about 11eV too high (see Table 3.2). As in the case of neutral Ba and La, the  $^1P$  term of the *collapsed* 4f orbital in  $\text{La}^{3+}$  is strongly influenced by the electrostatic exchange integral  $G^1(4d, 4f)$  via its relatively large Slater Condon coefficient  $g^1$  (Hansen 1972a), which makes center of gravity Hartree-Fock (c-g HF) calculations unsuitable (Clark 1987). The calculated values for these parameters are listed in Table 2.1 and Table 2.2. We therefore performed LSD-HF calculations for the  $4f(^1P)$  and the  $4f(^3D)$  with the suite of the Cowan codes (1968, 1981) in which the procedure is to minimize the energy of the term in question instead of the center of gravity (c-g) of the configuration. In the case of the  $4f(^1P)$  state, the Coulomb interaction  $4d^{-1}4f$  is so strong between the  $4d^{-1}$  hole and the 4f electron, that its appropriate energy, which is given in first order perturbation theory as the weighted sum over Slater integrals (see eqn.(2.20)), is completely insufficient approximated on the basis of

Table 3.1: *Hartree-Fock parameters for the  $4d^9 4f^1 5s^2 5p^6 ({}^1P_1)$  term in  $La^{3+}$  (values in eV).*

$E_{av}$	$\xi_{4d}$	$\xi_{4f}$	$F^2$	$F^4$	$G^1$	$G^3$	$G^5$
115.63	1.142	0.012	3.85	2.032	3.481	2.087	1.449

atomic orbitals which are obtained in a (c-g)HF calculation. Therefore in the *LSD* approach, the variation of the Coulomb energy (eqn.(2.20)) with respect to the radial wavefunctions  $P_{n_i, l_i}$  for a specific term is taken into account in the energy functional given in eqn.(2.7). As a result, we obtain a *LSD*-HF equation identical to eqn.(2.8) except for the presence of the additional direct term (Cowan 1981, chapter 16-8)

$$\frac{1}{w_i} \sum_k \sum_{j \neq i} f^k(l_i l_j) \int_0^\infty \frac{r^k}{r^{k+1}} P_{n_j, l_j}^2(r_2) dr_2 \quad (3.1)$$

within the brackets on the left side of eqn.(2.8), (note that  $f^k(l_i l_i) = 0$  in the case of  $La^{3+}$ ), and the additional exchange term

$$\frac{-P_{n_j, l_j}}{w_i} \sum_k \sum_{j \neq i} g^k(l_i l_j) \int_0^\infty \frac{r^k}{r^{k+1}} P_{n_j, l_j}(r_2) P_{n_i, l_i}(r_2) dr_2 \quad (3.2)$$

on the right hand side.

This results in different local single electron potentials  $V_{LSD}^i(r)$  for the triplet and singlet states as illustrated for the appropriate wavefunctions  $4f({}^3D_1)$  and  $4f({}^1P_1)$  in the upper part of Figure 3.6. Relaxation effects were included in computing the HF orbitals, this proves essential when comparison is made with many-body type calculations presented later. The predicted energy of the  $4d^9 4f({}^1P)$  term using the *LSD*-HF technique is in much better agreement with the experimental value. The fact, that the Slater integrals are smaller in this case, indicates that the *LSD* approach is more appropriate. The calculated Slater integrals are given in Table 3.1.

The energy value obtained for the  $4f(^1P_1)$  is 121.3 eV which can be compared with the previous results of 123.8 eV by Hansen (1972a) and 121.2 eV by Starace (1974). In general, there is good agreement between the different results, although all are still a few eV too high. While Hansen's calculational approach is similar to ours, Starace's results are based on the Random Phase Approximation (RPA) method, in which he included for the initial and the final state all configurations of multiple 4d excitations involving  $(4, \epsilon)f$  electrons. This type of correlation is not considered in the following discussion, where we performed  $4d \rightarrow (n, \epsilon)f$  intrachannel configuration interaction Hartree-Fock (CI-HF) calculations including the 6p and 7p states. Large mixing among the members of the  $^1P$  channel is observed (see Table 2.8) by calculating the non diagonal  $(n, \epsilon)f(^1P) - (n', \epsilon')f(^1P)$  matrix elements. Hansen (1972b) showed by using the Brillouin theorem (Brillouin 1932), that in a LSD-HF approach, the electrostatic intrachannel interactions for the members of the  $^1P$  channel are automatically included. In general, it is well known, that many-body calculations, which go beyond the HF model and describe the correlations between electrons in their mutual Coulomb field can be performed either in a variational or in a perturbation procedure as already discussed to some extent in describing relaxation effects as a true many-body phenomenon. In order to explain this in a more illustrative picture, the term dependence of the excited 4f state can be interpreted as a departure from the original spherical symmetry of the electron distribution. This is caused by rearrangement processes of the remaining 4d electrons in response to the excitation which leads to a new dipole symmetry. The consequent polarization can be taken into account either in a self consistent field procedure where the  $4d^{-1} - 4f$  Coulomb interaction is included (LSD approach) or in a c-g HF calculation including extended  $4d^9(n, \epsilon)f$  configuration interactions (see Figure 3.5). The latter calculational approach was taken by Hansen et al (1989) where  $4d \rightarrow (n, \epsilon)f$  intrachannel configuration interaction Hartree-Fock (CI-HF) calculations including the 6p and 7p states were performed. Their *ab initio* results are

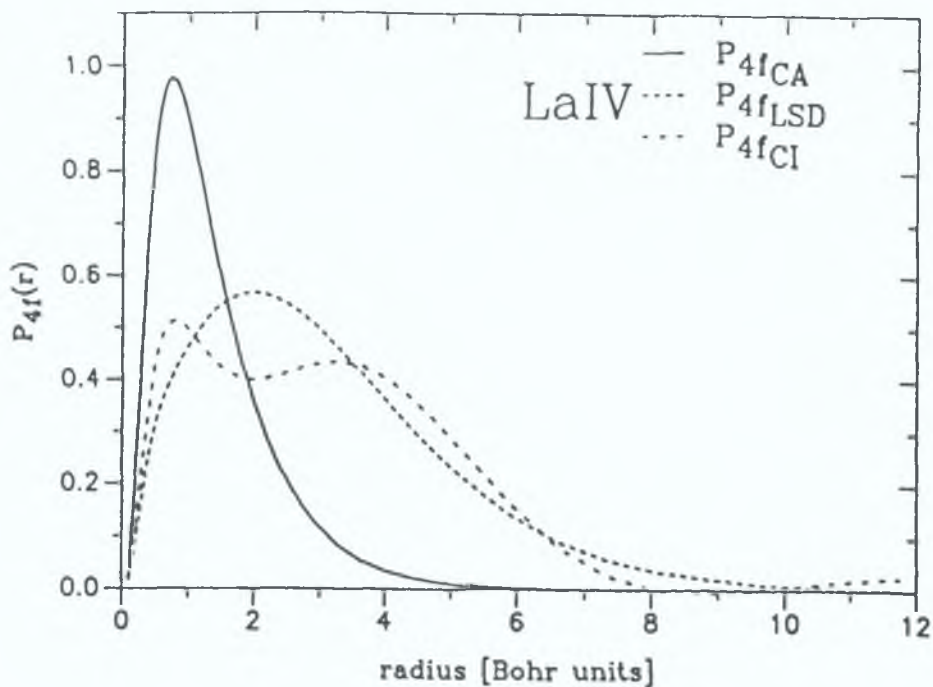


Figure 3.5: The LS term dependence for the  $4f(^1P)$  of  $\text{La}^{3+}$  is approximated by using configuration average (CA) radial wavefunction and performing configuration interaction calculations including the  $4d^9(n, \epsilon)f$  Rydberg states. The  $P_{4fCI}$  is obtained from an expansion of CA wavefunctions of the form  $P_{4fCI} = 0.7P_{4fCA} - 0.6P_{5fCA} - 0.2P_{6fCA} - 0.1P_{7fCA} - 0.1P_{8fCA}$ , where the coefficients are the mixing coefficients of the  $4d^9(n, \epsilon)f$  configuration interaction calculation. The comparison with the  $P_{4fLSD}$  wavefunction shows a close agreement having in mind that the contributions from the continuum orbitals are neglected in the construction of  $P_{4fCI}$ .

in fairly good agreement with the new experimental data but cannot explain the observed splitting of the main peak, although the calculations indicated, that the position of the second line coincides with the  $4d^9_{3/2}6p_{1/2}$  term at 119.70eV, but its associated gf value is predicted to be far too small.

A complete intrachannel CI calculation on the c-g HF basis includes all  $4d^9(n, \epsilon)f$  configurations to infinite order. Using a similar approach to Hansen (Hansen et al 1989), 26 configurations of discrete and continuum states were included in the following calculation. The continuum was discretized as described

by Cowan (1981). The *ab initio* results are in fairly good agreement with the calculations performed by Hansen et al (1989). Furthermore, because only a limited number of configurations were taken into account in the CI-HF calculations, and e.g. correlations of multiply excited 4d electrons were not considered (see Starace 1974) the quite common scaling procedure was used (Sugar 1972) to substitute the neglected effects for the  $4d^9 4f(^1P)$  term. In the following CI calculations, the  $G^k$  Slater integrals were scaled by a factor of 0.82 in order to shift the  $4f(^1P)$  term down to its observed position from 120.9 eV to 118.9 eV. Since only the  $4f(^1P)$  term is largely influenced by the  $G^1$  integral, the scaling has negligible effects on the energy positions of the other terms. The new position of the  $4d^9 4f(^1P)$  state is now much closer to the  $4d_{3/2}^9 6p_{1/2}$  state, which effects the mixing of these states after the diagonalization of the CI energy matrix. In general, CI mixing of two states is large if the CI matrix element is large compared to their energy distance. Due to the enhanced mixing of the  $4d^9 4f(^1P)$  and  $4d_{3/2}^9 6p_{1/2}$  states, the latter one gains distinctly in oscillator strength and autoionization width. As a result we obtained an  $f$  value of 5.0 for the  $4d^9 4f(^1P)$  and 0.22 for the  $4d_{3/2}^9 6p_{1/2}$  state. The results of the new calculation enabled to assign the observed transition lines to members of the Rydberg series converging to their appropriate  $4d_{(5/2),(3/2)}^9$  limits as shown in Figure 3.4. The autoionizing widths of the resonance lines have been estimated using the  $R^k$  integrals connecting the eigenvector components of the diagonalized energy matrix to the  $5s^2 5p^{-1} \epsilon(s, d)$  and  $5s^1 5p^6 \epsilon p$  continua (as described in Chapter 2.3.1). The results of the calculated energies, oscillator strengths  $gf$  and autoionizing FWHM widths  $2\Gamma$  are presented in Table 3.2.  $jj$ -coupling notation is used in Table 3.2 except for the  $4d^9 4f$  configuration, where the  $LS$  coupling scheme is more appropriate.

According to Fano's theory of autoionization (Fano 1961), where the case of a single discrete state interacting with several different continuum states is considered, the absorption profile can be described by  $\sigma_a(q + \epsilon)^2 / (1 + \epsilon^2) + \sigma_b$ .  $\sigma_a$  describes the excitation into the part of the continuum which interacts with

Table 3 2 Calculated single configuration (SC) (*ab initio*) and configuration interaction Hartree-Fock (CI-HF) energies ( $G^k$  scaled down to 82%), weighted oscillator strengths ( $gf$ ) and autoionisation widths ( $2\Gamma$ ) for the  $4d^{10} \rightarrow 4d^9nf, mp$  transitions with  $n = 4, 5, \dots, 9$  and  $m = 6, 7$  in  $La^{3+}$  and comparison with the experimental energy values  $JJ$ -coupling notation is used except for the  $4d^94f$  configuration, where the  $LS$  coupling scheme is more appropriate Only the strongest lines, which are observable in the spectrum are listed Note the difference of the total oscillator strength of the discrete  $4d \rightarrow nf, mp$  transition array in the SC and CI calculation

label	experimental energy (eV)	SC-HF energy (eV)	$f_{SC}$	CI-HF energy (eV)	$f_{CI}$	$2\Gamma$ (eV)
$4d^94f(^3D)$	102.10	102.80	0.02	102.90	0.027	0.017
$4d^9_{5/2}6p_{3/2}$		117.27	0.05	117.31	0.002	0.005
$4d^94f(^1P)$	118.95	129.72	11.6	118.90	5.03	1.2
$4d^9_{3/2}6p_{1/2}$	119.70	119.82	0.04	119.80	0.22	0.05
$4d^9_{5/2}5f_{7/2}$	125.09	124.94	0.07	125.55	0.73	0.22
$4d^9_{5/2}7p_{3/2}$	126.16	126.31	0.02	126.27	0.034	0.002
$4d^9_{3/2}5f_{5/2}$	127.69	127.72	0.10	128.07	0.60	0.19
$4d^9_{3/2}7p_{1/2}$	128.84	129.01	0.01	128.96	0.02	0.001
$4d^9_{5/2}6f_{7/2}$	129.73	129.68	0.04	130.14	0.64	0.27
$4d^9_{5/2}7f_{7/2}$	131.81	132.20	0.02	132.10	0.01	0.001
$4d^9_{3/2}6f_{5/2}$	132.61	132.51	0.04	132.84	0.41	0.14
$4d^9_{5/2}8f_{7/2}$	133.74	133.82	0.01	133.89	0.21	0.12
$4d^9_{5/2}9f_{7/2}$	134.80	134.80	0.01	134.74	0.02	0.007
$4d^9_{3/2}7f_{5/2}$	135.40	135.50	0.02	135.14	0.14	0.03
$4d^9_{3/2}8f_{5/2}$	136.74	136.62	0.01	136.61	0.19	0.07
$4d^9_{3/2}9f_{5/2}$	137.71	137.63	0.01	137.63	0.06	0.14
$\Sigma f$			12.07		8.36	



the resonance while  $\sigma_b$  represents the excitation into the resonance unaffected part of the continua,  $\epsilon = 2(E - E_0)/2\Gamma$  is the difference in photon energy from resonance energy  $E_0$  in units of the FWHM  $2\Gamma$  and  $q$  is the asymmetry parameter proportional to the ratio of the reduced dipole matrix elements of the initial state to the final discrete state and of the initial state to the final continuum state. The FWHM of the resonance is proportional to the sum of the autoionization rates  $A_k^a$  into the different continua  $k$ , which represent the configuration interaction matrix elements  $R^k$  of the resonance with the continuum state. The photoabsorption spectrum shows that  $q$  is probably very large due to the rather symmetrical shape of the resonance lines, and that the continuous background  $\sigma_b$  is negligible. Therefore the shape of the resonances can be simplified by applying approximate Lorentzian profiles  $f \times \Gamma \times \pi^{-1} / ((E - E_0)^2 + \Gamma^2)$  (see Chapter 2.3.1). Figure 3.6 shows the calculated spectrum using the parameters presented in Table 3.2. In order to take various broadening effects and the limited instrumental resolution into account, the spectrum is convolved with a Gaussian profile of 0.15 eV width, which corresponds to the measured FWHM of the  $4f(^3D)$  line. Good agreement is achieved for the  $4d^9nf$  Rydberg states and the  $4d^96p$  lines, while the  $4d^97p$  lines seem to be underestimated.

The  $4d_{(5/2),(3/2)}^9$  thresholds were estimated from the recorded spectrum, by fitting the Ritz formula  $E = I_p - R\xi^2 / (n - \delta)^2$  to each Rydberg series, with  $R$  the corrected Rydberg constant,  $I_p$  the threshold energy and  $\xi$  the charge of the core, assuming the quantum defect  $\delta$  is constant. The obtained values of  $138.2 \pm 0.2$  eV and  $141.1 \pm 0.2$  eV agree well with the calculated values of 138.05 eV and 140.9 eV.

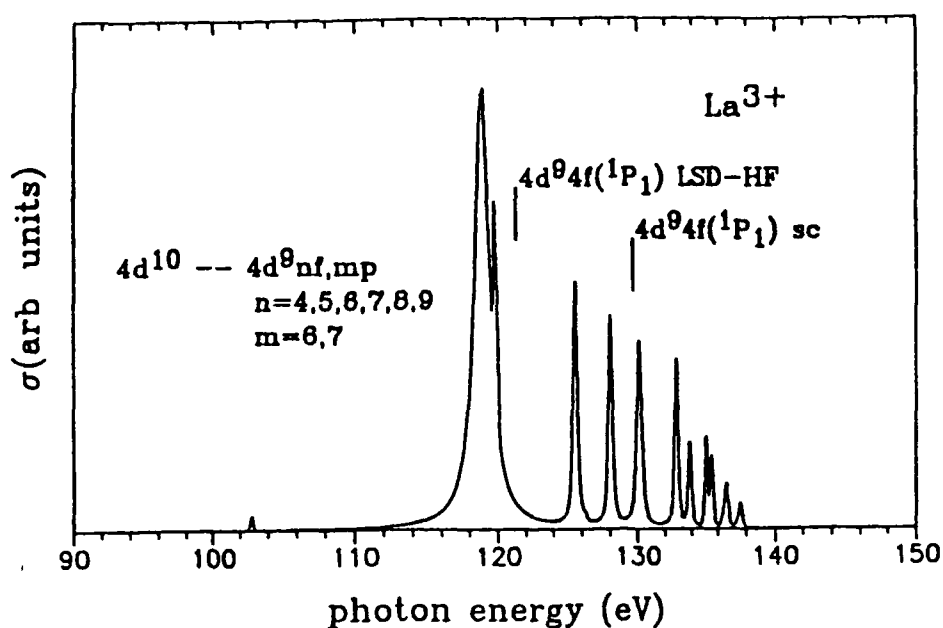
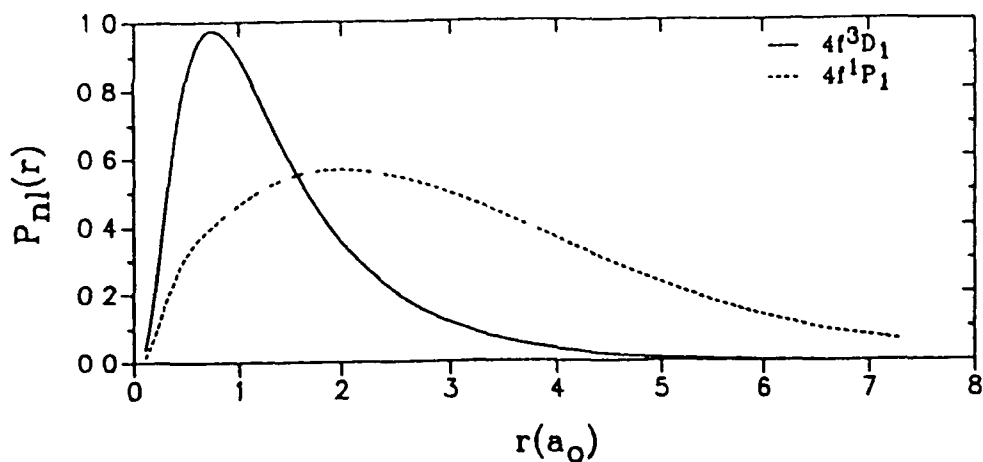


Figure 18 Upper part:  $4f(^3D_1)$  and  $4f(^1P_1)$  wavefunctions of  $\text{La}^{3+}$ . The large difference illustrates the strong term dependence for the  $^1P$  state. Lower part: Calculated photoabsorption spectrum in the 4d excitation region for  $\text{La}^{3+}$  with the CI-HF method. The spectrum is convolved with a Gaussian profile of 0.15 eV width for comparison with the experimental data. The vertical bars represent the energies of the  $4d^9 4f(^1P)$  term calculated via single configuration center of gravity (sc) Hartree-Fock and LS term dependent Hartree-Fock method.

### 3.2.2 Random Phase Approximation Calculations in Combination with the Many-Body Perturbation Theory

In the discussion so far, the many electron response to the external field is accounted by an effective one electron wave function  $4f(^1P)$  which is used in the calculations of the transition and electrostatic interaction matrix elements. An alternative approach is to consider that the external field polarizes the electron charge cloud of the atom which gives rise to an induced field. Both external and induced field superimpose to produce an effective driving field to which the electrons respond independently. In this sense, when the external field is rather weak, the random phase approximation with exchange (RPAE) can be regarded as a time dependent effective mean field theory. Ivanov et al (1993) have calculated the  $\text{La}^{3+}$  spectrum using the RPAE in conjunction with the many body perturbation theory (MBPT) over the whole photon energy region of interest. The MBPT starts from the HF approximation (HFA) as a zero one, where the 4d subshell energy was obtained to be -146.49eV and the  $4d \rightarrow 4f$  transition energy 125.75eV. The 4d spin orbit splitting was calculated within first order perturbation theory to be 2.85eV. The following obtained energies are  $E_{4d_{5/2}} = -145.35\text{eV}$  and  $E_{4d_{3/2}} = -148.20\text{eV}$ . The transition energies were improved by calculating the self energy part  $\sum_{4d}(E)$  of the single electron Green function for the 4d electron within second order perturbation theory (Amusia 1990)

$$\langle 4d | \sum(E) | 4d \rangle = \sum \frac{1}{(2l+1)(2L+1)} \times \left[ \sum_{\substack{\nu_2 > F \\ \nu_1, \nu_3 < F}} - \sum_{\substack{\nu_2 < F \\ \nu_1, \nu_3 > F}} \right] \frac{\langle 4d, \nu_2 || U_L || \nu_3, \nu_1 \rangle \langle \nu_3, \nu_1 || V_L || 4d, \nu_2 \rangle}{E + E_3 + E_1 - E_2 + i\delta(1 - 2n_{\nu_3})} \quad \delta \rightarrow 0 \quad (3.3)$$

where  $\nu_j$  is the set of quantum numbers  $(n_j, l_j, m_j, \mu_j)$  and E is the corresponding energy of this state,  $\langle \nu_1, \nu_2 || U_L || \nu_3, \nu_4 \rangle$  and  $\langle \nu_1, \nu_2 || V_L || \nu_3, \nu_4 \rangle$  are the reduced

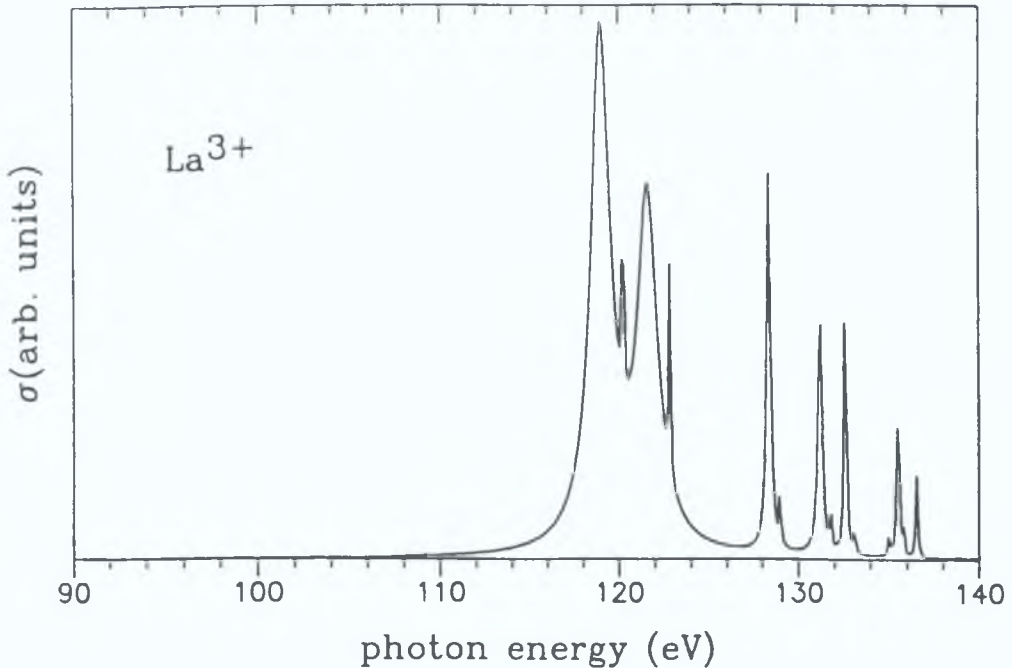


Figure 3.7: Photoabsorption spectrum in the 4d excitation region of  $\text{La}^{3+}$  calculated with the MBPT/RPAE method by Ivanov et al. (1993).

Coulomb matrix elements with the transferred angular momentum  $L$ , taking into account the corresponding direct and combined (direct + exchange) interactions. The sum  $\nu > F (< F)$  is performed on all excited (engaged) states beyond (under) the Fermi level. The  $n_\nu$  is a step-function ( $n = 0$ , if  $\nu > F$  and  $n = 1$ , if  $\nu < F$ ). In case of the 4d electron,  $(2l + 1) = 5$  and the transitions with the transferred momenta  $L = 0, 1, 2, 3$  were taken into account in the 4d self-energy calculation.

The new energy of the 4d subshell, corrected due to the many-electron interaction is obtained by solving the equation  $E_{4d} = E_{4d}^{HF} + \text{Re}\langle 4d | \sum (E_{4d}) | 4d \rangle$  selfconsistently. As a result, the  $E_{4d}$  energy shift is calculated to be 4.56eV and the corrected 4d subshell energy -141.9eV. The imaginary part of  $\langle | \sum (E_{4d}) | \rangle$  determines the width of the 4d hole state due to Auger decay:  $\gamma_A = 0.059$  eV.

The energies of the dipole transitions from the 4d subshell and other calculated parameters are given in Table 3.3. The oscillator strengths of the discrete transitions are calculated within the RPAE, where the five dipole channels  $5p \rightarrow \epsilon(s, d)$ ;  $5s \rightarrow \epsilon p$  and  $4d \rightarrow (n, \epsilon)(p, f)$  are taken into account. The main

Table 3 3 Excitation energies, widths and oscillator strengths for the dipole transitions from the 4d shell in ground state  $La^{3+}$  calculated with the MBPT/RPAE method (Ivanov et al 1993) Note, that the total oscillator strength of the RPAE calculation agrees remarkably well with the value obtained in the CI-HF approach

transition	excitation energy (eV)	total width (eV)	oscillator strengths
4d(5/2) - 4f(5/2)	118 74	1 21	3 82
- 4f(7/2)	118 87	1 21	
4d(5/2) - 6p(3/2)	120 24	0 07	0 185
4d(3/2) - 4f(5/2)	121 59	1 21	2 547
4d(3/2) - 6p(1/2)	122 50	0 07	0 123
- 6p(3/2)	123 10	0 07	
4d(5/2) - 5f(5/2)	128 33	0 25	0 56
- 5f(7/2)	128 37	0 25	
4d(5/2) - 7p(3/2)	129 04	0 059	0 029
4d(3/2) - 5f(5/2)	131 18	0 25	0 373
- 7p(1/2)	131 66	0 059	0 02
- 7p(3/2)	131 89	0 059	
4d(5/2) - 6f(5/2,7/2)	132 62	0 14	0 224
- 8p(3/2)	133 11	0 059	0 0124
4d(5/2) - 7f(5/2,7/2)	135 04	0 10	0 011
- 9p(3/2)	135 36	0 059	0 0067
4d(3/2) - 6f(5/2)	135 47	0 14	0 15
- 8p(1/2)	135 84	0 059	0 0083
- 8p(3/2)		0 059	
4d(5/2) - 8f(5/2,7/2)	136 54	0.08	0 06
- 10p(3/2)	136 73	0 059	0 004
total strength			8 13

contribution comes from the  $4d \rightarrow 4f$  transition, which reveals itself as a giant autoionizing resonance with a FWHM  $2\Gamma = 1.15\text{eV}$  and an oscillator strength of 6.37. The results of the corrected energies, oscillator strengths and width (Auger and autoionization) for the  $4d \rightarrow nf, mp$  transitions with  $n = 4, 5, 8$  and  $m = 6, 7, 8, 9$  are represented in Figure 3.7. The comparison with the experimental data confirms the assignment of the two strong resonance lines at 118.95eV and 119.70eV due to  $4d_{5/2} \rightarrow 4f, 6p$  transitions. The predicted series  $4d_{3/2} \rightarrow 4f, 6p$  between 121-123eV (see Figure 3.7) is not observed in the experiment (Figure 3.4). This must be connected with a redistribution of oscillator strengths due to strong coupling between the  $4d_{5/2,3/2} \rightarrow 4f$  transitions via the effective mean field, which is considered to be important for overlapping resonances with large width, but has not been taken into account here. In analogy to the classical model of the driven motion of two coupled harmonic oscillators, strong meanfield coupling causes the spin-orbit split subshells to oscillate in two modes in phase acting like a single subshell with a large oscillator strength and a large energy shift ( $\omega = \omega_0 + \tilde{\omega}$ ), out of phase leading to near cancellation of the induced fields with a weak oscillator strength and a negligible energy shift ( $\omega = \omega_0$ ) which is quite nicely demonstrated in a following RTDLDA calculation. However, for the higher transition series, where the widths are significantly smaller, spin orbit splitting becomes dominant and we obtain spin-orbit split transitions  $4d_{5/2} \rightarrow nf$  and  $4d_{3/2} \rightarrow nf$  with relative intensities in the ratio of the statistical weights 6:4 if relativistic effects are negligible. This can be tested from the experimental data in Figure 3.6, where the intensities of the transition lines of interest are estimated by taking the integral over the observed feature which should yield to a value proportional to the oscillator strength under the assumption, that the limited instrumental resolution which causes the resonance lines to be broadened, can be disregarded. This is certainly justified for the strong and broad 5f and 6f features, so that for the  $4d \rightarrow 5f$  transitions, the experimental ratio of its appropriate spin-orbit transition strength is 1.34 (CI-HF 1.22) and for the  $4d \rightarrow 6f$

transitions, the ratio is estimated to be of the order of 1.28 (CI-HF 1.56), which agrees remarkably well with the calculated cross section branching ratios of the  $4d_{5/2}$  and  $4d_{3/2}$  subshells for  $\text{La}^{3+}$  of about 1.3 by Cheng & Johnson (1983) using the relativistic random phase approximation (RRPA). Therefore, the experimental spectrum indicates, that the 4d subshell is actually influenced by relativistic effects which go beyond a first order description to the Schrödinger equation on the basis of the Dirac-Hartree-Fock theory. However at the same time the experimental data also show, that these effects are small and nonrelativistic theories are applicable for the description of the 4d excitation spectrum of  $\text{La}^{3+}$ .

### 3.2.3 Time Dependent Local Density Approximation Calculations

The *giant resonance* of the rare earth spectra has also been interpreted as a *collective resonance*, where the excitation energy is shared among all electrons in an atomic shell (Wendin 1982). The Time Dependent Local Density Approximation (TDLDA) calculations for the Ba isonuclear sequence by Nuroh et al (1982) incorporate this collective type of excitation as a many body theory.

Zangwill & Soven (1980) and Zangwill (1983) applied the TDLDA successfully to calculate the photoabsorption spectra for the elements Ar, Kr, Xe and Ba which are characterized by a spherically symmetric shell structure. In the case of Ba the *giant resonance* was interpreted as a heavily damped collective oscillation of the entire 4d subshell in response to the effective driving field.

We employed the TDLDA code *GOLIATH* written by Zangwill & Liberman (1984) to calculate the photoabsorption cross section for  $\text{La}^{3+}$  in the energy region which was investigated experimentally. The result is shown in Figure 3.8. The spectrum is dominated by a strong symmetric resonance at 117eV, which can be associated with the  $4d \rightarrow 4f$  transition, followed by three higher Rydberg members converging to the 4d threshold at 131.5eV.

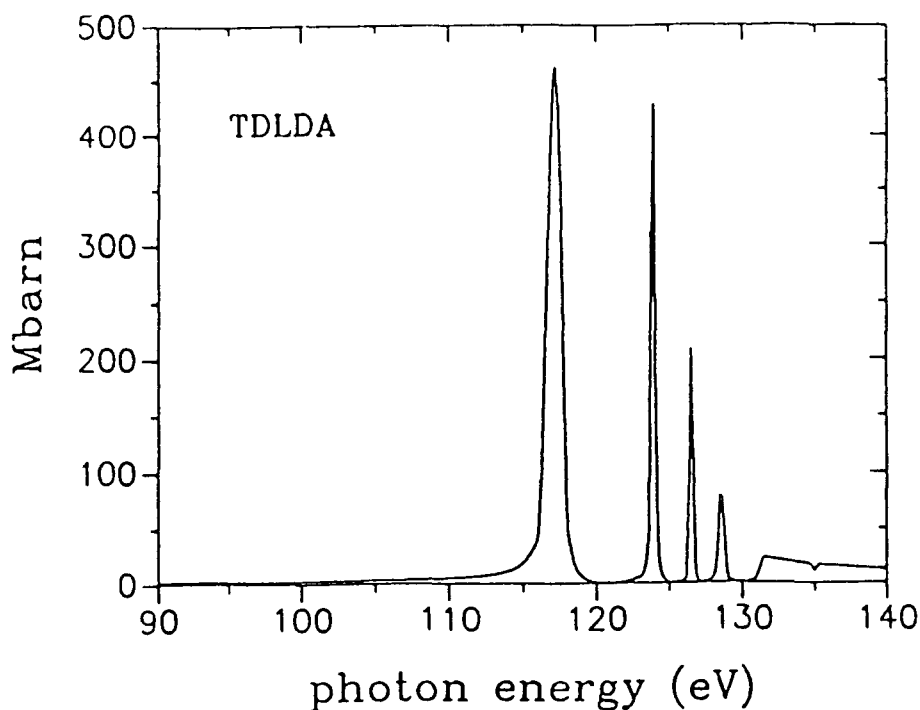


Figure 3.8 Photoabsorption cross sections in the 4d excitation region of  $\text{La}^{3+}$  calculated with the TDLDA method

The comparison with the calculated  $\text{Ba}^{2+}$  spectrum by Nuroh et al (1982) shows clearly a transfer of oscillator strength from the continuum into the Rydberg states, especially into the 4f resonance, when progressing along the Xe isoelectronic sequence. This is consistent with the experimental data of  $\text{Ba}^{2+}$  and  $\text{La}^{3+}$  shown in Figure 3.10.

In order to investigate the influence of relativistic effects, the code *DAVID*, a relativistic analogue of *GOLIATH* written by Liberman & Zangwill (1984) was used to calculate the  $\text{Ba}^{2+}$  and  $\text{La}^{3+}$  isoelectronic sequence. The spectra are shown in Figure 3.9. Here the LDA - Dirac equation is solved to obtain the electron orbitals. Each subshell is split into two shells with  $j = l + s$  and  $j = l - s$ . In contrast to the nonrelativistic model, the two 4d shells  $4d_{5/2}$  and  $4d_{3/2}$  which are coupled via the effective mean field can oscillate in two modes of collective motion, in phase acting essentially like a single shell or out of phase resulting in a resonance with a weaker oscillator strength (Wendm 1982). Thus, the spectra obtained from the relativistic code exhibits additional comparatively weak features. The importance of relativistic effects is clearly demonstrated from the



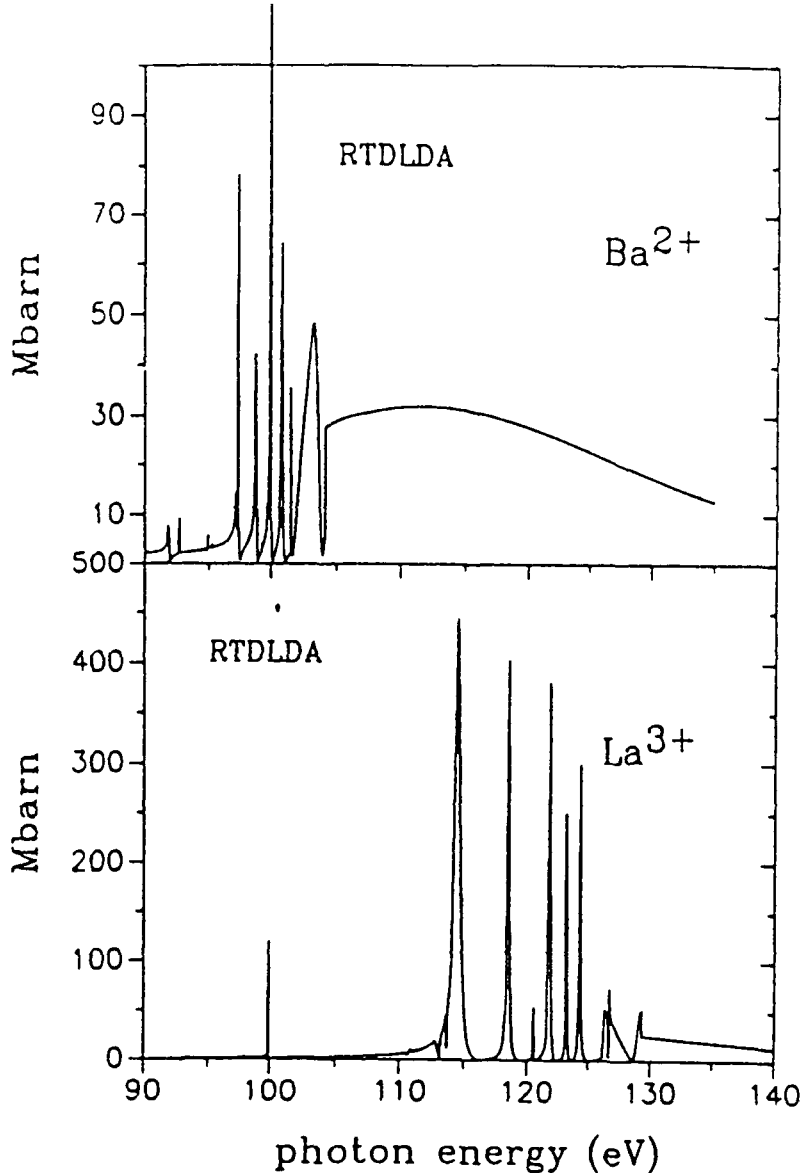


Figure 39 Photoabsorption cross sections in the 4d excitation region of  $Ba^{2+}$  and  $La^{3+}$  calculated with the relativistic (R)TDLDA method

experimental spectra in which a number of such weak features are identifiable. In the case of  $La^{3+}$ , the weak line in the energy region of 100 eV corresponds in the  $LS$ -term picture to the  $4d^9 4f(^3D)$  term, its relative strength and its energy distance to the main resonance line of 15 eV are in fairly good agreement with the experimental data. Other weak features like the weak transition line at 120 eV might be associated with the  $4d_{5/2}^9 7p_{3/2}$  state. The absolute values of the calculated  $4d_{5/2}^9$  and  $4d_{3/2}^9$  thresholds at 126.2 eV and 129.0 eV are far off the observed ones, although the difference of 2.8 eV is consistent with the other calculated and observed values for the spin orbit splitting of the 4d subshell.

In summary, we may conclude, that the TDLDA model provides a reasonable

qualitative description of the  $\text{La}^{3+}$  photoabsorption spectrum. Relativistic calculations (RTDLDA) certainly improved the result qualitatively, additional lines are predicted which are also observed in the experiment, whereas the agreement between the calculated and observed energies of the resonance lines is worse than in the nonrelativistic model. Nevertheless the general trend of the photoabsorption behaviour for Xe like Ba and La ions is well reproduced in the TDLDA/RTDLDA model.

### 3.2.4 $\text{Ba}^{2+}$ and $\text{La}^{3+}$ in Isoelectronic Comparison

Figure 3.10 shows the relative photoabsorption cross section data for the  $\text{Ba}^{2+}$  and  $\text{La}^{3+}$  isoelectronic pair. The direct comparison shows a striking change in the photoabsorption behaviour. Most impressive in following the sequence from  $\text{Ba}^{2+}$  to  $\text{La}^{3+}$  is the increase of oscillator strength for the  $4f(^1P)$  giving a broad and strong resonance and the reduction in the continuum background, the higher Rydberg transition lines also gain in strength. These observations are consistent with the calculational analysis of the  $4d^{10} \rightarrow 4d^9(n, \epsilon)f$  transition array based on the CI-HF theory, which predicts for the discrete transition array with  $n = 4, 5, \dots, 9$  a total strength of 2.2 for  $\text{Ba}^{2+}$  and 8.3 for  $\text{La}^{3+}$  and which leads to the conclusion based on the oscillator sum rule of eqn (2.34), that in  $\text{Ba}^{2+}$  the bulk of oscillator strength of about 80% is manifested in continuum absorption, whereas in  $\text{La}^{3+}$  the contribution of continuum strengths is reduced down to 15%. Cheng & Froese Fischer (1983) showed by studying the Xe-isoelectronic sequence with use of a term dependent Hartree-Fock technique, that the appearance of the intense absorption lines in  $\text{Ba}^{2+}$  is due to the term dependence of the 4f orbital collapse in the  $4d \rightarrow f^1P$  channel. Furthermore they showed, that the collapse is of gradual nature which occurs between  $\text{Ba}^{2+}$  and  $\text{Ce}^{4+}$ . After the 4f orbital is completely collapsed for high degrees of ionization along the isoelectronic sequence, the bulk of oscillator strength is concentrated at the  $4d^9 4f(^1P)$  level, so that the only

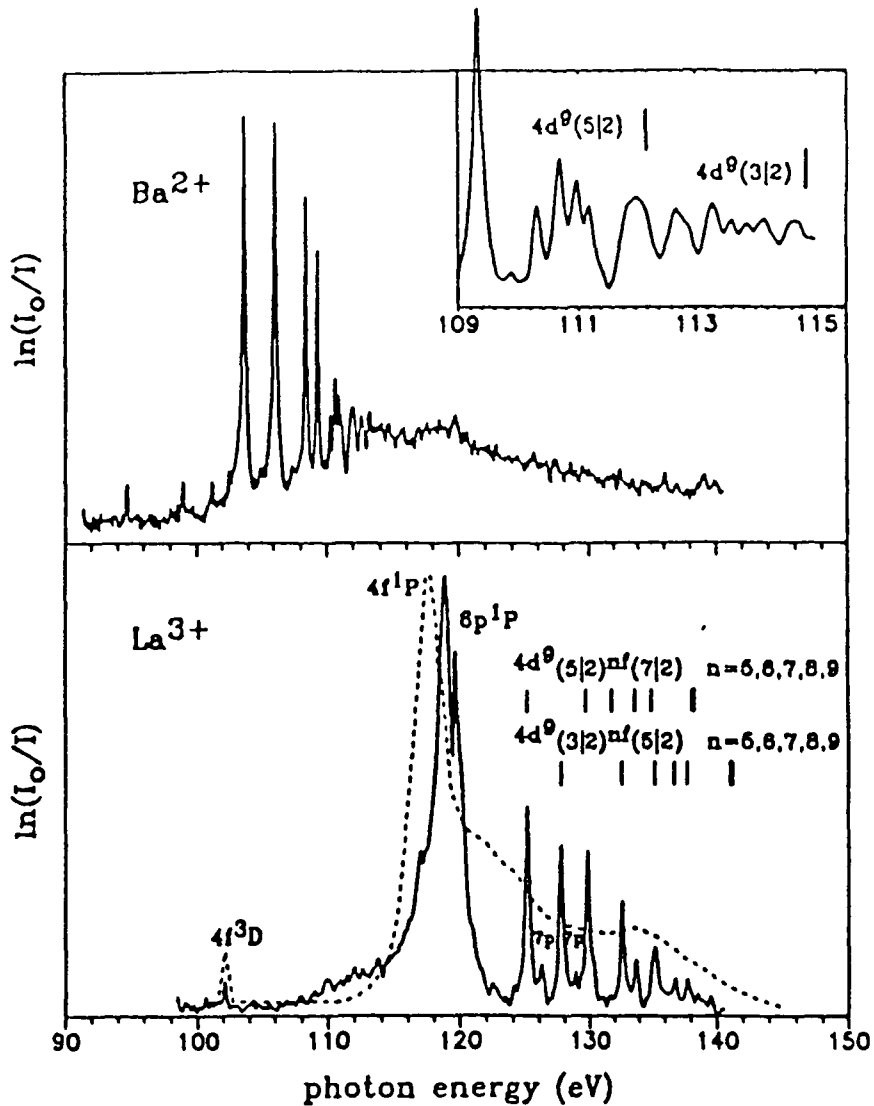


Figure 3 10 Photoabsorption spectra of  $Ba^{2+}$  and  $La^{3+}$  in the 4d excitation region using the dual-laser plasma (DLP) technique. The enlarged  $Ba^{2+}$  spectrum shows the  $4d^9_{(5/2),(3/2)}nf$  Rydberg series for  $n = 9, 12$ , where the states with the  $4d^9_{(3/2)}$  hole lie above the  $4d^9_{(5/2)}$  threshold. The thresholds deduced from the experimental data are  $112.2 \pm 0.2$  eV and  $114.8 \pm 0.2$  eV, which agree well with the values given in (Clark 1984). The  $La^{3+}$  spectrum is shown together with photoabsorption data of solid  $LaF_3$  from Olsen et al (1980).

strong resonance line in the spectrum is again the  $4d \rightarrow 4f(^1P)$  transition.

However, the experimental data show that the concentration of oscillator strengths into the  $4f(^1P)$  state has already occurred in  $\text{La}^{3+}$ , which suggests, that the main step between a hydrogenic and a collapsed  $4f(^1P)$  orbital takes place between  $\text{Ba}^{2+}$  and  $\text{La}^{3+}$ .

Further insight into the orbital collapse phenomenon was provided in the calculations by Hansen et al (1989), where he showed, that the increase of oscillator strengths occurs concomitantly with a strong broadening of the resonance line. A very recent RPAE calculation for the  $4d \rightarrow 4f$  transition in  $\text{Ce}^{4+}$  (Ivanov 1992) supports this contention which is clearly confirmed by the experimental data of the Xe isoelectronic Ba and La spectra.

In Figure 3.11 the  $4f(^1P)$  radial wavefunctions and appropriate local potentials are plotted for  $\text{Ba}^{2+}$ ,  $\text{La}^{3+}$  and  $\text{Ce}^{4+}$ . The figure illustrates the collapse along the Xe isoelectronic sequence and shows, how the potential barrier between the inner and the outer valley disappears in moving from  $\text{Ba}^{2+}$  to  $\text{Ce}^{4+}$ . The comparison also shows, that the biggest step in the gradual collapse occurs between  $\text{Ba}^{2+}$  and  $\text{La}^{3+}$  but is not completed before  $\text{Ce}^{4+}$ .

### 3.2.5 4d Photoabsorption of $\text{La}^{3+}$ , Solid $\text{LaF}_3$ , $\text{LaCl}_3$ and La Metal

Apart from their fundamental theoretical interest, photoabsorption cross sections of free ions also provide key data for the understanding of the electronic structure of solids and molecules. In order to illustrate this point, we compare our experimental data in Figure 3.12 with cross sections of solid  $\text{LaF}_3$  (Olsen et al 1982, Suzuki et al 1975),  $\text{LaCl}_3$  and La metal (Suzuki et al 1975). All spectra show the dominant  $4d^9 4f(^1P)$  resonance and the weak  $4f(^3D)$  line at about 102 eV.

Since La is trivalent in the molecular and the solid state, the analyses of the corresponding spectra have always been based on the concept of an effectively

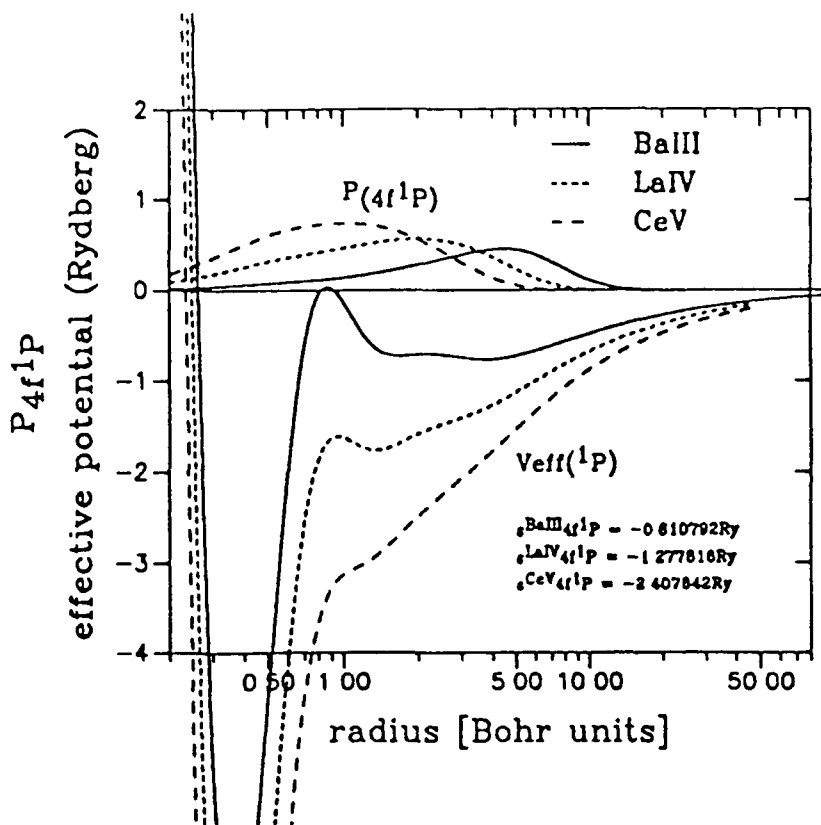


Figure 3.11  $4f(1P)$  radial wavefunctions and their appropriate effective local potentials for  $\text{Ba}^{2+}$ ,  $\text{La}^{3+}$  and  $\text{Ce}^{4+}$  isoelectronic sequence. Note the logarithmic scale for the radius. The potential, which is dropped below the  $4f(1P)$  threshold, still remains sufficiently strong for  $\text{Ba}^{2+}$  to separate the potential in an inner well region and an outer one (double valley potential). The appropriate wavefunction is located above the outer valley with its maximum at about  $5.0a_0$ . With increasing  $Z$ , the barrier disappears and the  $4f(1P)$  radial wavefunctions collapse into the inner well region with its maximum of about  $2.0a_0$  in  $\text{La}^{3+}$  and  $1.2a_0$  in  $\text{Ce}^{4+}$ .

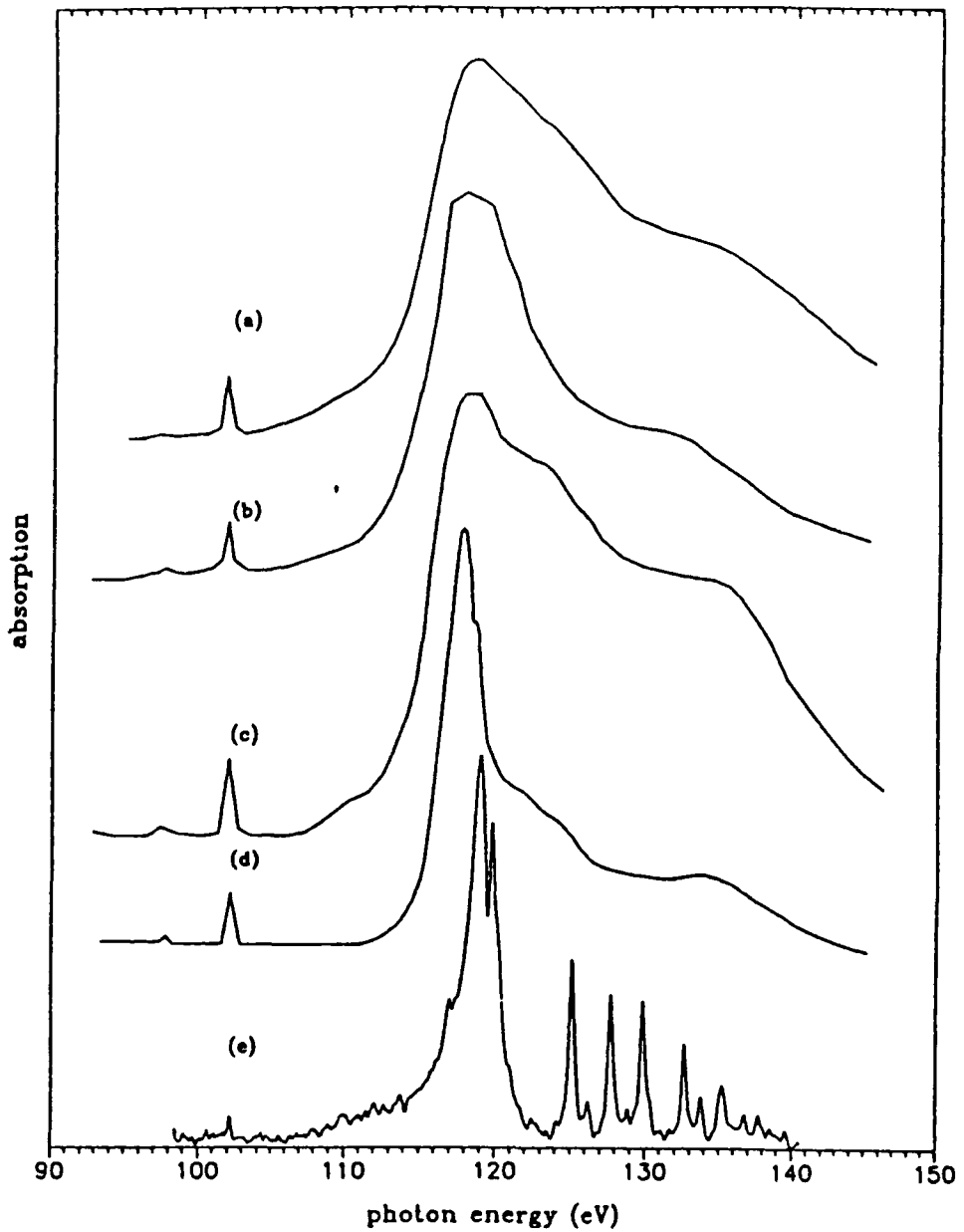


Figure 3 12 Absorption spectrum of  $\text{La}^{3+}$  in comparison with La metal, solid  $\text{LaF}_3$  and solid  $\text{LaCl}_3$  (a) La metal, (b)  $\text{LaCl}_3$ , (c)  $\text{LaF}_3$  all from Suzuki et al (1975) (d)  $\text{LaF}_3$  from Olsen et al (1982), (e)  $\text{La}^{3+}$

free triply charged ion in the ground state essentially unperturbed by the metallic environment (Dehmer & Starace 1972, Starace 1972, Sugar 1972) or by the ligands of the other halides. This was justified on the assumption, that the  $4d^94f$  states are strongly localized in the atom and interatomic interactions for these electrons with their environment are negligible. This is corroborated by the similarity between our  $\text{La}^{3+}$  spectrum and the  $\text{LaF}_3$  spectrum by Olsen et al (1982) to which I shall confine myself in the following discussion.

Olsen et al (1982) observed several peaks and shoulders in the  $\text{LaF}_3$  spectrum, which can be identified by comparison with the ion data. The shoulder at 118.8 eV therefore corresponds to the  $4d_{(3/2)}^96p_{(1/2)}$  state in  $\text{La}^{3+}$ . Furthermore, the line width of the  $4d^94f(^3D)$  term given by Olsen et al (1982) is 0.12 eV, while in the ion spectrum the width is measured to be 0.16 eV. However, based on the calculated results and on the observation made by Olsen et al (1982), it seems that the natural width is actually far narrower and the instrumental resolution being comparable in both experiments (using a  $20\mu\text{m}$  slit in the DLP experiment). This leads to the conclusion, that the  $4f(^1P)$  resonance of  $\text{La}^{3+}$  in its solid state is actually influenced by the environment albeit moderately, which causes the resonance to be broadened and shifted by about 1.3 eV towards lower energy. The 4d excitations into higher Rydberg states are also recognizable in the  $\text{LaF}_3$  spectrum. However, in these cases the disappearance of the pronounced line structure that prevails in the free ion spectrum is a clear indication of the non localized character of these states.

## Conclusion

In this Chapter, we presented the photoabsorption spectrum of  $\text{La}^{3+}$  ions in the 4d excitation region which was recorded using the DLP-technique. CI-HF, RPAE/MBPT and TDLDA/RTDLDA calculations were also carried out and discussed in comparison with the experimental data. The experimental results con-

firm the theory which predicted a dominant  $4d^9 4f(1P)$  resonance line but which was not observed in the previous experiment (Hansen et al 1989) It is shown, that the giant dipole resonance in  $\text{La}^{3+}$  associated with the 4d subshell excitation has acquired a definite discrete  $4d^{10} \rightarrow 4d^9 4f(1P)$  character at the expense of the  $4d^{10} \rightarrow 4d^9 \epsilon f$  continuum transitions Polarization effects revealed through large term dependence of the  $4d^9 4f(1P)$  state are found to be strong Comparison with the corresponding spectrum of  $\text{Ba}^{2+}$  confirms the theory which predicts that the collapse of the  $4f^1 P$  orbital along the Xe isoelectronic sequence has a gradual nature and is not yet complete for  $\text{Ba}^{2+}$  Finally, the giant dipole resonance in  $\text{La}^{3+}$  remains essentially unaffected by a solid state environment such as  $\text{LaF}_3$



# Chapter 4

## XUV Photoabsorption of Laser Generated Au Vapour

### Abstract

Photoabsorption by atomic Au in the 5p and 4f excitation region has been studied using the Dual Laser Plasma technique. The observed features are dominated by two prominent Fano-type resonance lines which can be attributed to  $5p \rightarrow 5d$  and  $4f \rightarrow 5d$  transitions of valence excited  $5d^9 6s^2(^2D_{5/2})$  Au followed by autoionisation. The experimental results are compared to spectra calculated for the excitation of  $5d^{10} 6s^1(^2S_{1/2})$  ground and  $5d^9 6s^2(^2D_{5/2}, ^2D_{3/2})$  valence excited states within the (R)Hartree-Fock theory and the Relativistic Time Dependent Local Density Approximation.

### 4.1 Introduction

The frequent use of gold in many industrial applications e.g. gold coated XUV mirrors make it of particular interest for study in the XUV excitation region. In the free atom form gold has the ground state configuration  $(5d^{10} 6s^1)$  (Moore 1958) with a filled 5d subshell, whereas in the metal, 5d hybridization with over-

lapping 6s and 6p bands leads to a shift of the 5d band in which the hybridized part is located above the Fermi level. The result is that the absorption edges are dominated by excitations to the hybridized 5d states in the 6s and 6p conduction bands (Dietz et al 1989). The faint photoabsorption features observed at the positions of the  $N_{6,7}$  edges in solid gold by Gudat et al (1974) appear to correspond to the observations made by Dietz et al. We therefore expect the photoabsorption data of free gold atoms from the *valence excited* state to be of particular interest for comparison with the solid state spectrum in order to investigate the atomic character of gold in a solid state matrix. Other interesting phenomena expected to be observed, include a cross over of the  $5p \rightarrow 5d$  and  $4f \rightarrow 5d$  transition lines when following the sequence of 5d transition metals along the periodic table. With increasing  $Z$ , the 4f shell is more tightly bound to the core which results in a gradual shift of the  $4f \rightarrow 5d$  transitions over the 5p excitation region. Finally, gold may be vapourized in a conventional furnace and is therefore amenable to detailed study of the excitation and decay dynamics by photoelectron spectroscopy. Photoabsorption data on atomic gold should be a useful starting point for such experiments.

One of the first systematic studies of photoabsorption in the XUV energy region of the 5d transition metals Ta, W, Re, Pt and of Au was carried out by Haensel et al (1969) using a synchrotron light source and samples prepared as thin films. They observed strong absorption at low energies which decreased rapidly with increasing photon energy. Two strong and broad absorption features, which originated from excitation of the electrons of the 5p shell, were observed between 30 and 70eV, superimposed on the background which was interpreted in terms of transitions of the valence electrons into continuum states. Transition lines from the 4f shell, which occur in the same energy region, were only observed for Pt.

More recently Dietz et al (1980) utilized electron-energy loss spectroscopy to measure the 5p and 4f excitation edges in solid Pt and Au. Their data provided more detailed information about the excitation mechanisms in the solid. They

found that in the case of Pt the line shapes are controlled by Fano-type configuration interactions in which the quasi-discrete core  $\rightarrow$  d excitation interferes with the excitation of valence electrons into continuum states. Interference effects between core and valence electron excitations were also observed for gold, but here the line shape could not be described by applying the Fano model.

Gold has already been studied in the VUV photoabsorption energy region (6.2-13.5eV) by Jannitti et al (1979) and in the same energy region by Dyke et al (1979) utilizing HeI photoelectron spectroscopy, where the  $5d^{-1}6s$  and the  $5d^{10}6s^{-1}$  ionisation energies were measured. The  $N_{6,7}O_{4,5}O_{4,5}$  Auger lines in solid gold have been investigated by Nyholm et al (1986) and Evans et al (1990); and in the free gold atom by Aksela et al (1984), which enabled them to deduce the 4f binding energies.

Costello et al (1991a) successfully carried out inner-shell photoabsorption studies for W and Pt. Their results together with calculations by Boyle in ref. [Costello et al 1991a] utilizing the many-body perturbation theory corroborate the predicted cross over phenomenon of the  $5p \rightarrow 5d$  and  $4f \rightarrow 5d$  transitions.

In the following chapter photoabsorption measurements of atomic Au in the 5p and 4f excitation region are presented. The results will be compared with theoretical photoabsorption cross sections calculated for the ground state  $5d^{10}6s^1(^1S_{1/2})$  and excited states  $5d^96s^2(^2D_{5/2}, ^2D_{3/2})$  of neutral gold.

## 4.2 Photoabsorption of Au in the 5p and 4f Excitation Region

Figure 4.1 shows the result of a series of photoabsorption measurements in the 4f excitation energy region obtained by varying the time delay between the generation of the absorbing and backlighting plasmas.

The sharp resonance at 80eV is attributed (see later) to the  $4f \rightarrow 5d$  transition

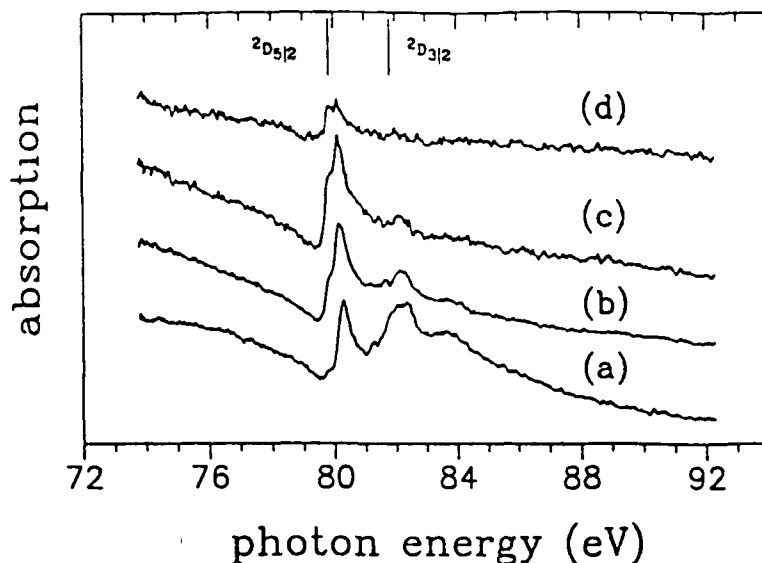


Figure 4.1 Relative absorption cross sections of Au vapour in the  $4f \rightarrow 5d$  excitation region taken at different time delays between the laser pulses a) 100ns, b) 200ns, c) 600ns and d) 1000ns. Spectrum c) shows photoabsorption from predominantly the  $^2S_{1/2}$  and  $2D_{5/2}$  states. The bars mark the position of the  $4f^{14}5d^96s^2(^2D_{5/2}) \rightarrow 4f^{13}5d^{10}6s^2(^2F_{7/2})$  and  $4f^{14}5d^96s^2(^2D_{3/2}) \rightarrow 4f^{13}5d^{10}6s^2(^2F_{5/2})$  transitions.

in valence excited atomic gold from  $4f^{14}5d^96s^2(^2D_{5/2})$  to  $4f^{13}5d^{10}6s^2(^2F_{7/2})$ ; the  $^2D_{5/2}$  state lies 1.6 eV above the ground state  $^2S_{1/2}$  and is metastable in the dipole approximation. Mosnier et al (1994) have previously shown that photoabsorption from valence excited states is achievable in laser created plasmas subject to the appropriate excitation and observation conditions. The advantage is of course, that such studies provide access to upper states which are not optically allowed from the ground state. The associated  $4f^{14}5d^96s^2(^2D_{3/2})$  to  $4f^{13}5d^{10}6s^2(^2F_{5/2})$  transition is observed at 82 eV and as the time delay is increased, reduces in strength compared with the  $^2D_{5/2}$  feature. This may be understood in terms of the greater excitation energy (3.0 eV) of the  $^2D_{3/2}$  valence excited level above the ground state. At a time delay of 600 ns (Figure 4.1c) the spectrum is dominated by the  $^2D_{5/2}$  feature with only a small hint of the  $^2D_{3/2}$  remaining. Therefore the photoabsorption spectrum at 600 ns is expected to arise predominantly from the ground ( $^2S_{1/2}$ ) and valence excited ( $^2D_{5/2}$ ) states. It proved difficult to record

satisfactory spectra for time delays greater than 600ns as the rapid expansion of the laser plasma plume reduced the optical opacity so that very poor signal to noise ratios were obtained (Figure 4.1)

Figure 4.2 shows the photoabsorption spectrum over the 40-110eV region recorded at the 600ns delay. The general shape of the spectrum resembles very much that of Pt recorded by Costello et al (1991a) except in the energy range of 80eV, where only one dominant resonance line is observed for gold.

In conjunction with the time resolved photoabsorption study of the Au plasma a comprehensive set of atomic structure calculations for the main dipole transition lines from ground and excited states of the  $5d^{10}6s^1$  and  $5d^96s^2$  configurations were undertaken. The main results are presented in Table 4.1. The dominant, broad and asymmetric peak at 55eV is attributed mainly to the  $5p \rightarrow 5d$  transition from  $5p^65d^96s^2(^2D_{5/2})$  to  $5p^55d^{10}6s^2(^2P_{3/2})$  followed by super Coster-Kronig decay into the  $5p^65d^86s^2\epsilon(p, f)$  channels due to the large overlap between the 5p and 5d orbitals. The interference with direct 5d photoionisation is responsible for the asymmetric shape of the resonance. A similar interpretation for the sharper but no less pronounced  $4f \rightarrow 5d$  resonance line at 80eV is made where the  $4f^{13}5d^{10}6s^2(^2F_{7/2})$  state autoionises into the same continua with emission of an electron from the 5p, 5d or 6s subshell. Here too, the direct photoionisation process interferes with the resonant one to give a typical Beutler-Fano profile.

As mentioned above, there is little evidence of photoabsorption from the excited  $5d^96s^2(^2D_{3/2})$  state, since the predicted  $4f^{14}5d^96s^2(^2D_{3/2})$  to  $4f^{13}5d^{10}6s^2(^2F_{5/2})$  transition at around 82eV is very weak. The calculations in Table 4.1 show, that the broad feature at 70eV can be explained in terms of photoabsorption from the  $^2S_{1/2}$  and (to lesser extent)  $^2D_{3/2}$  states to the  $5p^55d^{10}6s^2(^2P_{1/2})$  states, followed by a rapid decay which yields a large peakwidth of about 7eV.

Interesting also is the line structure observed in the 100eV energy region for which there is so far no definite explanation. By shortening the time delay between the laser pulses, their relative intensity changes together with the char-

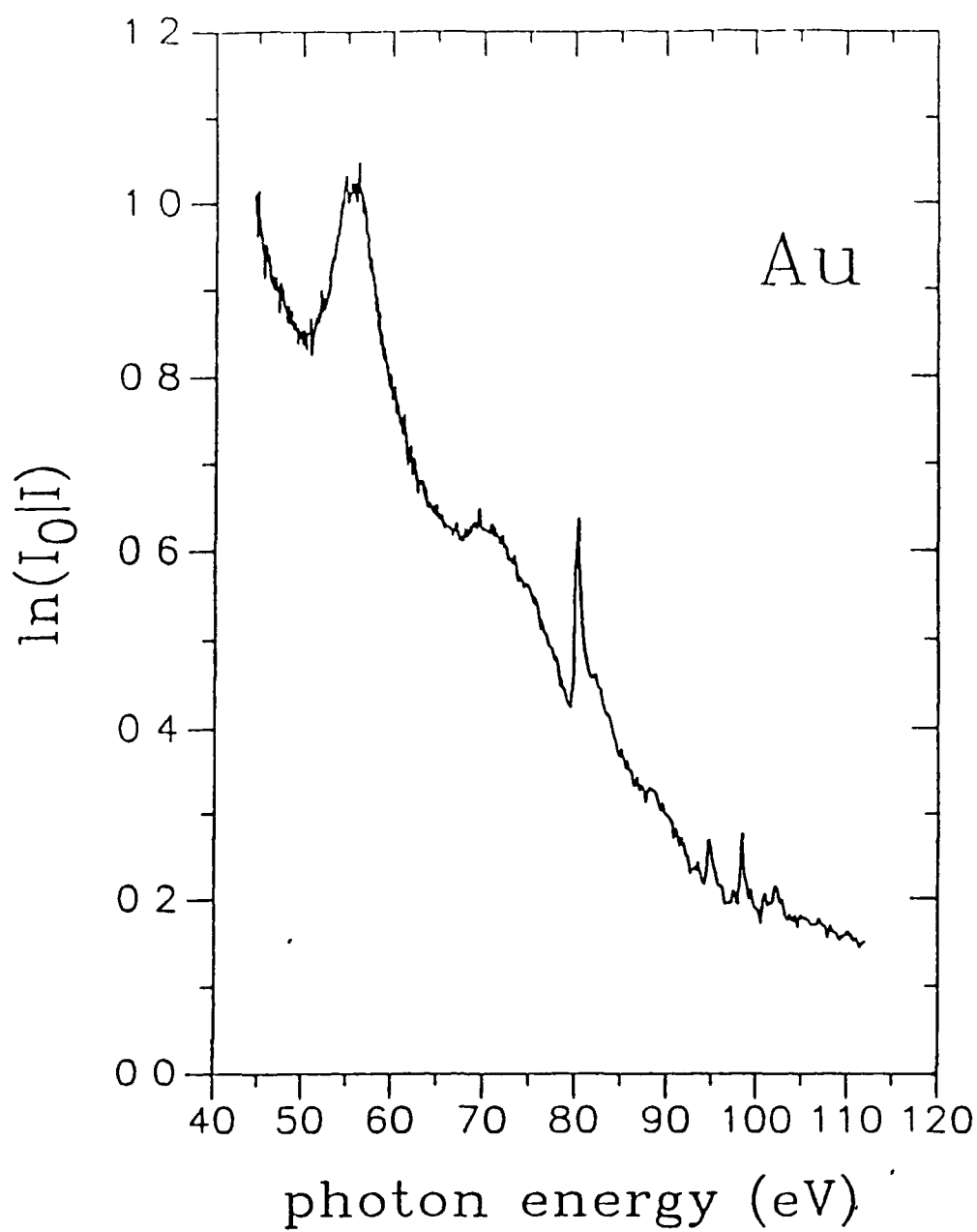


Figure 4 2. *Relative absorption cross section of Au vapour in the 5p and 4f excitation region taken at 600ns time delay between the two laser pulses*

Table 4.1: *The strongest transition lines from states belonging to the  $5d^{10}6s^1$  and  $5d^96s^2$  configurations of neutral gold. All energy values are in respect to the ground state  $5d^{10}6s^1(^2S_{1/2})$ .*

initial state	$E_i$ (eV)	final state	$E_f$ (eV)	$\Delta E$ (eV)	red. Dipole ( $ea_0$ )	autoionization width (eV)
$5d^{10}6s^1(^2S_{1/2})$	0.0	$5p^55d^{10}6s^2(^2P_{3/2})$	57.0	57.0	-0.51	8.1
		$5p^55d^{10}6s^2(^2P_{1/2})$	73.1	73.1	-0.36	6.7
$5d^96s^2(^2D_{5/2})$	1.4	$5p^55d^{10}6s^2(^2P_{3/2})$	57.0	55.6	-1.72	7.9
		$4f^{13}5d^{10}6s^2(^2F_{7/2})$	80.5	79.1	0.45	0.39
		$4f^{13}5d^{10}6s^2(^2F_{5/2})$	84.2	82.8	0.10	0.39
$5d^96s^2(^2D_{3/2})$	3.0	$5p^55d^{10}6s^2(^2P_{3/2})$	57.0	54.0	0.57	8.2
		$5p^55d^{10}6s^2(^2P_{1/2})$	73.1	70.2	-1.28	6.6
		$4f^{13}5d^{10}6s^2(^2F_{5/2})$	84.2	81.2	-0.37	0.38

acteristic 4f line of  $^2D_{5/2}$  Au. Therefore these lines must be associated with the neutral species in the gold plasma. They may represent the  $4f \rightarrow 6d$  absorption lines from valence excited gold since their energy values are in part larger than the 4f binding energies (91.6eV and 95.3eV) of Au ground state given by Aksela et al (1984); however it cannot be ruled out an interpretation based on multiple excitations.

In order to extract the Fano parameters  $E_o$ ,  $q$  and  $\Gamma$  for the observed  $5p \rightarrow 5d$  and  $4f \rightarrow 5d$  transition lines the features were fitted each with a Beutler-Fano profile (Fano 1961)

$$\sigma = \sigma_a[(q + (E - E_o)/\Gamma)^2 / (1 + ((E - E_o)/\Gamma)^2)] + \sigma_b \quad (4.1)$$

employing the model of an isolated autoionisation resonance coupled to several continua. The line shape is characterized mainly by the asymmetry parameter  $q$ , the FWHM  $2\Gamma$  and the energy position  $E_o$  of the resonance line. The quantities  $\sigma_a$  and  $\sigma_b$  represent the two portions of cross sections describing transitions into

continuum states which do and do not interact with the discrete autoionising state respectively. The decreasing background was approximated by a linear function of energy. The best fit parameters of the  $5p \rightarrow 5d$  resonance line are  $E_o = 54.3\text{eV}$ ,  $2\Gamma = 6.5\text{eV}$ ,  $q = 2.3$ , and for the  $4f \rightarrow 5d$  transition line  $E_o = 80.0\text{eV}$ ,  $2\Gamma = 0.7\text{eV}$  and  $q = 2.0$ .

### 4.3 Hartree-Fock Calculations for Au

*Ab initio* (R)HF calculations using the Cowan code (Cowan 1967,1968) were carried out in order to deduce theoretical Fano parameters for comparison with the fitted ones. These calculations include relativistic corrections of the mass-velocity and the Darwin term to the configuration average energy. The major steps which were undertaken in order to obtain the Fano parameters are introduced briefly in the following paragraph.

In the first step, the dipole matrix elements  $D_{ij}$  and energy positions  $E_o^{ij}$  for the transition lines  $|i\rangle \rightarrow |j\rangle$  were calculated. In the second step, the decay rates  $A_{jk}^a$  of the discrete excited state  $|j\rangle$  into the various continua  $|k\rangle$  were evaluated, which are determined by the configuration interaction matrix elements  $V_{jk}$  between the states  $|i\rangle$  and continua  $|k\rangle$ . The decay rate of the excited states is assumed to be dominated by autoionisation processes, therefore the FWHM  $2\Gamma$  is proportional to the sum of the autoionisation rates. In the third step, the continuum dipole matrix elements  $D_{ik}$  connecting the initial discrete state and final continuum state were obtained. In the Fano theory (Fano 1961, Ueda 1987) for an isolated resonance coupled to several continua the asymmetry parameter  $q$  is given by

$$q_{ij} = \frac{D_{ij}}{\pi \sum_k M_{jk} D_{ik}} \quad (4.2)$$

with  $M_{jk} = V_{jk} / \sqrt{\sum_k V_{jk}^2}$

The calculated values for the  $5p \rightarrow 5d$  resonance, for which 31 continuum channels were taken into account, are  $E_o = 55.6\text{eV}$ ,  $2\Gamma = 7.9\text{eV}$  and  $q = 1.7$ , and



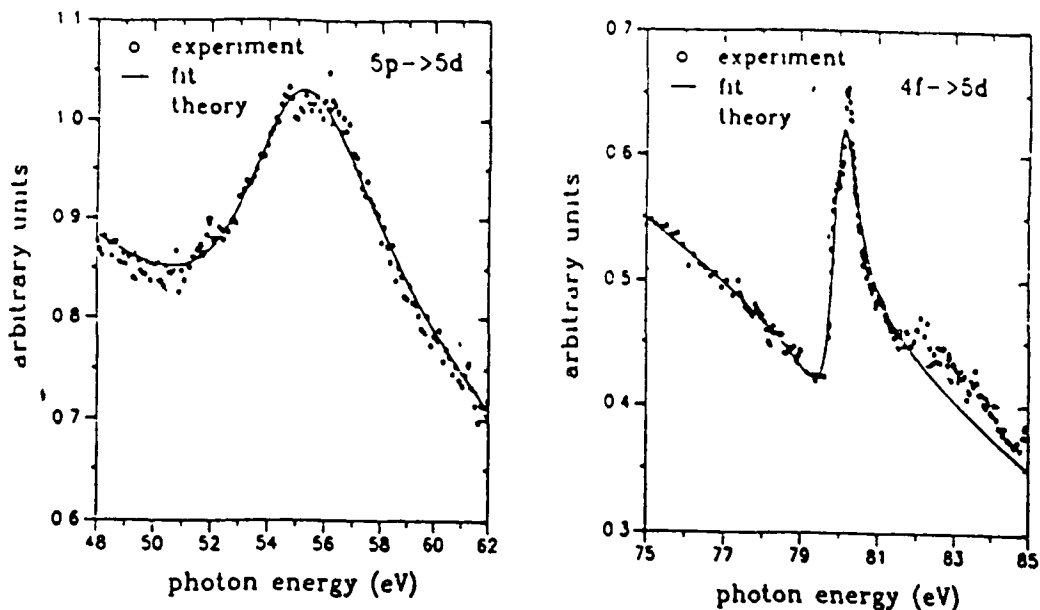


Figure 4.3: (left) Photoabsorption data in the  $5p \rightarrow 5d$  excitation region. The data points are fitted with a Fano profile employing the model of a single discrete state interacting with several continua. The obtained fit values are  $E_o = 54.3\text{eV}$ ,  $2\Gamma = 6.5\text{eV}$  and  $q = 2.3$ . The dashed curve shows the calculated cross section with  $E_o = 55.6\text{eV}$ ,  $2\Gamma = 7.9\text{eV}$  and  $q = 1.7$ . (right) Photoabsorption data in the  $4f \rightarrow 5d$  excitation region in comparison with the calculated cross section (dashed curve). The data points are fitted with a Fano profile employing the model of a single discrete state interacting with several continua. The obtained fit values are  $E_o = 80.0\text{eV}$ ,  $2\Gamma = 0.7\text{eV}$  and  $q = 2.0$ . The calculated Fano parameters are  $E_o = 79.2\text{eV}$ ,  $2\Gamma = 0.39\text{eV}$  and  $q = 2.2$ .

for the  $4f \rightarrow 5d$  resonance with 52 continuum channels the obtained parameters are  $E_o = 79.2\text{eV}$ ,  $2\Gamma = 0.4\text{eV}$  and  $q = 2.2$ . The theoretical results for both resonance lines are in reasonable agreement with the fitted values. The experimental and theoretical results are shown together for comparison in Figure 4.3.

In order to provide a more complete interpretation of the photoabsorption data over the whole energy range, Martins (1994) calculated absolute photoabsorption spectra of the three lowest even parity states of gold over the 40-110eV range. Energy dependent  $\sigma_a$ ,  $\sigma_b$ ,  $\Gamma$  and  $q$  parameters were used to describe the resonant cross sections, which were then added to the nonresonant contribution in order to provide the total cross section. Since the discrete resonances are widely separated

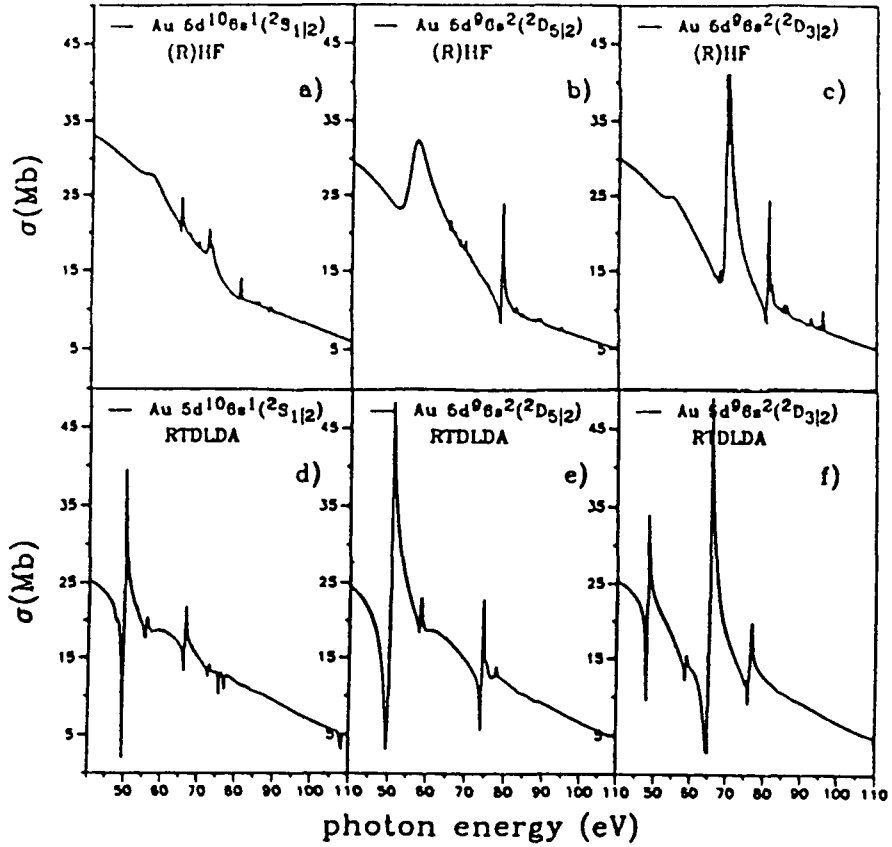


Figure 4.4 a)-c) Calculated photoabsorption spectra of Au within the (R)HF theory for the ground state  $5d^{10}6s^1(^2S_{1/2})$  and valence excited  $5d^9 6s^2(^2D_{5/2}, ^2D_{3/2})$  states d)-f) Calculated photoabsorption spectra of Au within RTDLDA for the ground state  $5d^{10}6s^1(^2S_{1/2})$  and valence excited  $5d^9 6s^2(^2D_{5/2}, ^2D_{3/2})$  states

in energy, their mutual interactions are negligibly small which makes Fano theory applicable. The agreement with the experimental data was improved by scaling the Slater integrals by 0.8. The individual contributions from the  $^2S_{1/2}$  ground state and the valence excited  $^2D_{5/2}, ^2D_{3/2}$  states are shown separately in Figure 4.4a-c.

## 4.4 Time Dependent Local Density Approximation Calculations for Au

Zangwill (1983) interpreted the  $3p \rightarrow 4s$  resonance of atomic copper as a damped collective oscillation of the entire  $3p$  subshell with subsequent decay into the  $3d$  photoionisation channel. His calculations are based on a Time Dependent generalisation of the density functional formalism within the Local Density Approximation (TDLDA) and are closely related to the Random Phase Approximation with Exchange (RPAE).

We have employed the relativistic RTDLDA code *DAVID* written by Liberman & Zangwill (1984) to calculate the total photoionization cross sections for the ground and valence excited states of gold. Here the one electron Dirac equation is solved in order to construct the electron charge density in the gold atom. Each atomic shell is split into two spin-orbit subshells with spin projection parallel or antiparallel to the orbital angular momentum. The results are shown in Figure 4 4d-f and can be compared directly with the (R)Hartree Fock results. We can see, that both the (R)HF and the RTDLDA calculations yield qualitatively comparable photoabsorption behaviour in terms of absolute values and fine structure components. It is also clear that the observed spectrum is mostly due to the ground  $^2S_{1/2}$  and valence excited  $^2D_{5/2}$  levels as mentioned earlier.

In order to make the comparison clearer, Figure 4 5 shows the experimental spectrum together with the (R)HF and RTDLDA results. The experimental curve in Figure 4 5 is multiplied by a constant in order to match the maximum to that of the (R)HF spectrum. All theoretical curves shown in Figure 4 5 are the average of the  $^2S_{1/2}$  and  $^2D_{5/2}$  cross sections. (This is equivalent to assuming equal  $^2S_{1/2}$  and  $^2D_{5/2}$  populations in the gold vapour and is for illustrative purposes only.) The (R)HF results describe very satisfactorily the experimental spectrum. The direct comparison with the RTDLDA calculation and with the experimental data suggests that the use of the Hartree-Fock configuration interaction approach and

the mean field formulation are essentially equivalent for the description of the photoabsorption spectrum of gold

Following Zangwill (1987) further insight can be achieved by comparing RLDA and RTDLDA results. Differences between the results of the independent particle RLDA model and the many-body RTDLDA model are attributable to the dynamic response effects included in the latter. The RLDA/RTDLDA comparison in Figure 4.5 shows that the time dependent approach yields an enhanced photoabsorption cross section in the recorded energy range above 50eV. The absence of the  $5p \rightarrow 5d$  and the  $4f \rightarrow 5d$  resonances in the RLDA curve is not unexpected as the resonant photoemission process can not be described within an independent particle model. By shifting the RTDLDA spectrum by about 5eV to higher energies reasonable agreement with experiment in terms of energy positions and relative absorption strength may be obtained but with incorrect form parameters particularly for the 5p resonance.

## 4.5 Conclusion

In summary, for the first time XUV photoabsorption data of atomic Au in the 5p and 4f excitation region has been recorded. The results provide first and foremost information about the photoabsorption properties from the valence excited  $5d^9 6s^2 ({}^2D_{5/2})$  state. The observed spectrum is dominated by two prominent Fano-type resonance lines which can be attributed to  $5p \rightarrow 5d$  and  $4f \rightarrow 5d$  transitions of valence excited  $5d^9 6s^2 ({}^2D_{5/2})$  Au followed by autoionisation. The characteristic features in the spectrum could be satisfactorially described with the Hartree-Fock theory of resonant photoabsorption taking first order relativistic corrections into account. Furthermore detailed calculations of absolute photoabsorption cross sections of gold from ground- and excited states based on the (R)HF and RTDLDA theories have been performed. The results lead to the conclusion that interference effects between core and valence electron excita-

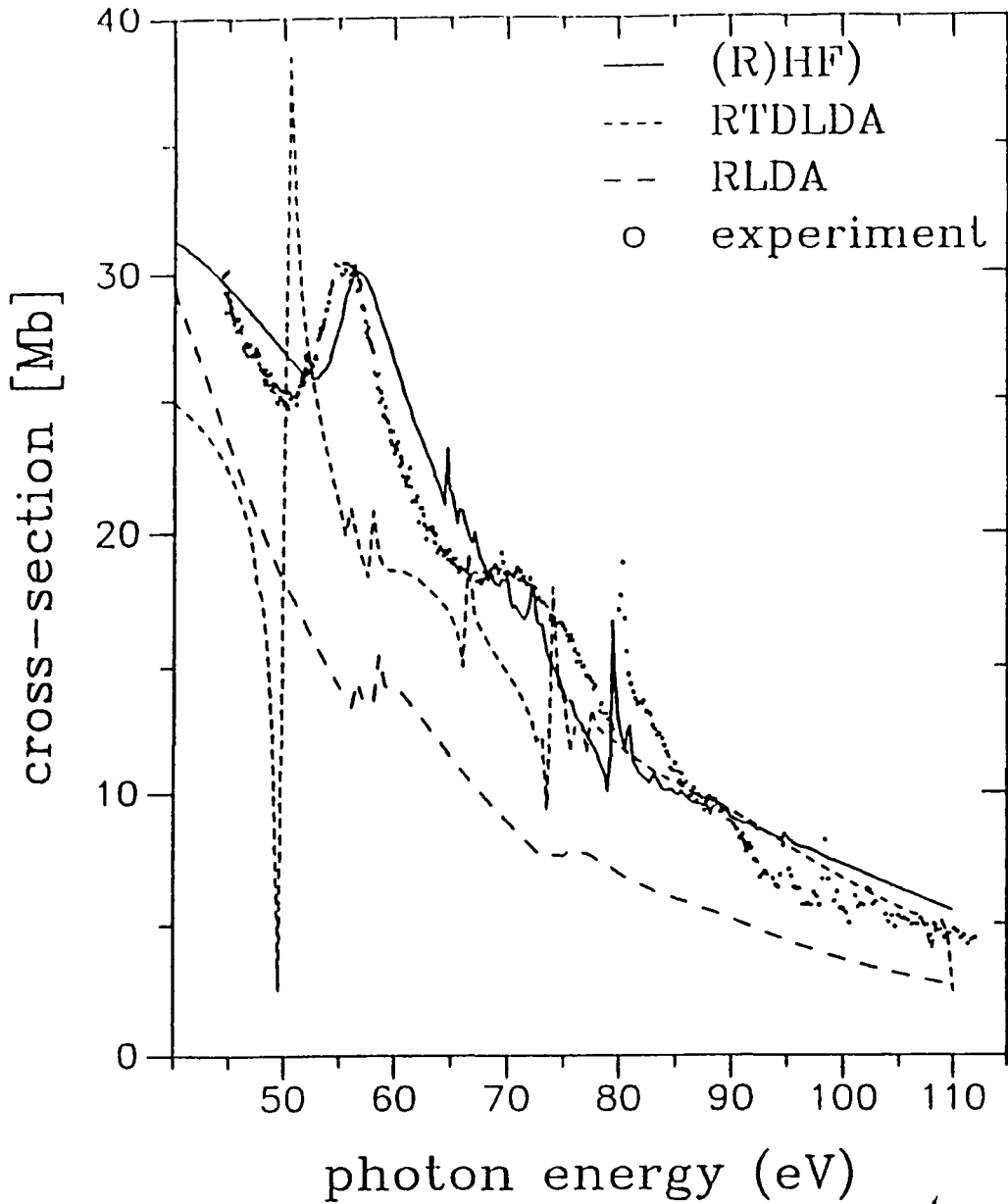


Figure 4.5. Measured relative photoabsorption cross section of a gold vapour in comparison with calculated absolute cross sections within the RLDA, the RTDLDA and the (R)HF theory. The experimental data are multiplied by a constant in order to match the maximum to that of the (R)HF spectrum. The calculated spectra are the averaged of the  $^2S_{1/2}$  and  $^2D_{5/2}$  cross sections, assuming equally populated levels in the gold vapour, for illustrative purposes only.

tions manifested in the asymmetric photoabsorption line profiles provide the most significant evidence for electron correlations in gold in the investigated spectral energy region

# Final Conclusion

To date, most experimental photoabsorption cross section data available represent spectra of atoms, molecules and solids, whereas the theory has already progressed to some extent in investigating the photoabsorption behaviour of ions especially in an isonuclear/isoelectronic comparison with its atomic counterparts. Theorists therefore have expressed their interest in suitable new experimental data which can be used to test the theoretical predictions and which promise new insight in the understanding of many-body effects. The exploration of a laser generated plasma in time and space with use of the DLP-technique can be used to establish predicted trends in photoabsorption and provide motivation for succeeding more sophisticated experiments involving photoion or photoelectron spectroscopy. The study of the decay channels requires in general a profound knowledge of the excitation mechanism which can be provided in a photoabsorption study.

It has been shown in this work, that the DLP-technique is able to provide good quality photoabsorption data as demonstrated for the well known Ba,La,Ce,Sm and Eu sequence. Furthermore the DLP-technique has been proven to be a unique tool in order to obtain new photoabsorption cross section data of excited atoms ( $\text{Au}^*$ ) and ions ( $\text{Ba}^+$ ,  $\text{Ba}^{2+}$ ,  $\text{La}^{3+}$ ) which is an important goal in following the new trends of interest in atomic physics.  $\text{La}^{3+}$  follows its isoelectronic partner  $\text{Ba}^{2+}$  which was recorded over 12 years ago (Lucatorto et al 1981) and may be regarded as a key result for the understanding of the photoabsorption behaviour in the Xe-isoelectronic sequence. The experimental data confirm the theory (Cheng & Froese Fischer 1983) which predicted a dominant  $4f(1P)$  resonance in the

La<sup>3+</sup> spectrum and settles a fundamental discrepancy between experiment and theory, since the resonance line could not be observed in previous experimental investigations (Hansen et al 1989) The photoabsorption data of Au are of more preliminary nature, which hopefully will stimulate further more detailed studies

The major weakness of the experimental technique is the lack of independent plasma-diagnostic data needed to cross check the identification of the ion stages in the absorption column under current investigation This was compensated in this work by detailed theoretical studies In fact, the interplay between theory and experiment led to the success in obtaining new good quality photoabsorption data Various theories such as the CI-HF, (R)TDLDA/(R)LDA, RPAE and MBPT were applied and tested, each of them incorporates its own calculational technique and physical understanding for the description of the atom-photon interaction process In the near future, the system will be also operational in the VUV photon energy region, this will allow the user to probe the absorption column in the valence and inner-shell energy regions simultaneously The XUV spectra will be characterized with help of the VUV data which are generally well known It might then be possible to obtain cross section data for the pure ground state of neutral gold, since the VUV photoabsorption spectrum was measured previously by Jannitti et al (1979)



# Bibliography

- [Aksela et al 1984] Aksela S, Harkoma M, Pohjola M and Aksela H J Phys B At Mol Opt Phys **17**, 2227 (1984)
- [Amusia 1965] Amusia M Ya, Phys Lett **14**, 36 (1965)
- [Amusia 1967] Amusia M Ya, Phys Lett **24A**, 394 (1967)
- [Amusia et al 1971] Amusia M Ya, Cherepkov N A and Chernysheva L V, Zh Eksp Teor Fiz **60**, 160 (1971)
- [Amusia & Sheftel 1976] Amusia M Ya, and Sheftel S I, Phys Lett A, **55A**, 469 (1976)
- [Amusia et al 1975] Amusia M Ya, Ivanov V K and Chernysheva L V, IX IC-PEAC, Abstract of Papers (Seattle, 1975), 1135 (1975)
- [Amusia et al 1976] Amusia M Ya, Ivanov V K and Chernysheva L V, Phys Lett A **59A**, 191 (1976)
- [Amusia 1977] Amusia M Ya, in Atomic Physics **5**, eds Marrus R, Prior M and Shugart H, Plenum Press New York (1977)
- [Amusia et al 1980] Amusia M Ya, Ivanov V K, Sheinerman S A and Sheftel S I, JETPh (Soviet Physics), **78**, 910 (1980)
- [Amusia et al 1989a] Amusia M Ya, Ivanov V K, Kupchenko V A and Chernysheva L V, Zeitschr Phys D - At Mol Clust **14**, 215 (1989)

- [Amusia et al 1989b] Amusia M Ya, Ivanov V K and Kupchenko V A, *Zeitschr Phys D - At Mol Clust* **14**, 219 (1989)
- [Amusia 1990] Amusia M Ya, *Atomic Photoeffect*, Plenum Press (1990)
- [Baier et al 1994] Baier S, Gottschalk G, Kerkau T, Luhmann T, Martins M, Richter M, Snell G and Zimmermann P, *Phys Rev Lett* **72**, 2847 (1994)
- [Becker et al 1986] Becker U, Kerkhoff H G, Lindle D M, Kobrin P H, Ferret T A, Heimann P A, Truesdale C M and Shirley D A, *Phys Rev A*, **34**, 2586 (1986)
- [Bertsch et al 1991] Bertsch G F, Bulgac A, Tománek D, and Wang Y, *Phys Rev Lett* **67**, 2690 (1991)
- [Bloch 1933] Bloch F, *Zeitschr Phys* **18**, 363 (1933)
- [Brand & Lundqvist 1963] Brand W and Lundqvist S, *Phys Rev* **132**, 2135 (1963)
- [Brand et al 1967] Brand W, Eder L and Lundqvist S, *J Quant Spectr Rad Transfer* **7**, 411 (1967)
- [Brillouin 1932] Brillouin L, *J Phys (Paris)* **3** (1932)
- [Brown 1971] Brown G, *Unified Theory of Nuclear Models and Forces* North Holland, Amsterdam (1971)
- [Bruckner 1955a] Bruckner K A, *Phys Rev* **97**, 1353 (1955)
- [Bruckner 1955b] Bruckner K A, *Phys Rev* **100**, 36 (1955)
- [Carrol & Kennedy 1977] Carrol P K and Kennedy E T, *Phys Rev Lett* **38**, 1036 (1977)
- [Carroll et al 1980] Carroll P K, Kennedy E T and O'Sullivan G *Applied Optics* **9**, 1454 (1980)

- [Cheng & Froese Fischer 1983] Cheng K T and Froese Fischer C, *Phys Rev A* **28**, 2811 (1983)
- [Cheng & Johnson 1983] Cheng K T and Johnson W R, *Phys Rev A* **28**, 2820 (1983)
- [Clark 1984] Clark C W, *J Opt Soc Am B* **1**, 626 (1984)
- [Clark 1987] Clark C W, *Phys Rev A*, **35**, 4865 (1987)
- [Connerade & Mansfield 1982] Connerade J P and Mansfield M W D, *Phys Rev Lett* **48**, 131 (1982)
- [Connerade 1983] Connerade J P, *J Phys B At Mol Phys* **16**, L257 (1983)
- [Connerade & Pantelouris 1984] Connerade J P and Pantelouris M, *J Phys B At Mol Phys* **17**, L 173 (1984)
- [Connerade et al 1987] Connerade J P, Estava J M and Karnatak R C (eds) 1987 *Giant Resonances in Atoms, Molecules, and Solids* (New York Plenum Press) and references therein
- [Cooper 1964] Cooper J W *Phys Rev Lett* **13**, 762 (1964)
- [Cooper et al 1989] Cooper J W, Clark C W, Cromer C L, Lucatorto T B, Sonntag B, Kennedy E T and Costello J T, *Phys Rev A* **39**, 6074 (1989)
- [Costello et al 1991] Costello J T, Kennedy E T, Sonntag B and Clark C W, *Phys Rev A* **43**, 1441 (1991)
- [Costello et al 1991a] Costello J T, Kennedy E T, Sonntag B F and Cromer C L *J Phys B At Mol Opt Phys* **24** 5063 (1991)
- [Costello et al 1991b] Costello J T, Kennedy E T, Mosnier J-P, Carrol P K and O'Sullivan G, *Physica Scripta* **T34**, 77 (1991)

- [Cowan 1967] Cowan R D, Phys Rev **163** 54 (1967)
- [Cowan 1968] Cowan R D, J Opt Soc Am **58**, 808 (1968)
- [Cowan 1981] Cowan R D, *The Theory of Atomic Structure and Spectra*, University of California Press (1981)
- [Cowan 1984a,b] Cowan R D, programs  $\mathcal{RCN}$  mod32/HF mod8/ $\mathcal{RCN}\epsilon$ , *Computation of Atomic Radial Wavefunctions*, Los Alamos National Laboratory (1984) and program  $\mathcal{RCG}$  mod 9, *Computation of Angular Matrix Elements, Energy Levels and Atomic Spectra*, Los Alamos National Laboratory (1984)
- [Cromer et al 1985] Cromer C L, Bridges J M, Roberts J R and Lucatorto T B, Applied Optics **24**, 2996 (1985)
- [Dehmer et al 1971] Dehmer J L, Starace A F, Fano U, Sugar J and Cooper J W, Phys Rev Lett **26**, 1521 (1971).
- [Dehmer & Starace 1972] Dehmer J L and Starace A F, Phys Rev B **5**, 1792 (1972)
- [Desclaux 1975] Desclaux J P, Comput Phys Commun **9**, 31 (1975)
- [Dietz 1980] Dietz R E , McRae E G and Weaver J H, Phys Rev B **21**, 2229 (1980)
- [Dyke 1979] Dyke J M, Fayad N K, Morris A and Trickle I R, J Phys B At Mol Opt Phys **12**, 2985 (1979)
- [Dzionk et al 1989] Dzionk Ch, Fiedler W, van Lucke M and Zimmermann P, Phys Rev Lett **62**, 878 (1989)
- [Ederer et al 1975] Ederer D L, Lucatorto T B, Saloman E B, Madden R P and Sugar J, J Phys B At Mol Phys **8**, L21 (1975)

- [Evans et al 1990] Evans J A, Laine A D, Fowles P S, Duo L, McGilp J F, Mondio G, Norman D and Weightman P, *J Phys C Condens Matter* **2** 195 (1990)
- [Fano 1961] Fano U, *Phys Rev* **124**, 1866 (1961)
- [Fliflet et al 1975] Fliflet A W, Kelly H P and Hansen J E, *J Phys B At Mol Phys* **8**, L268 (1975)
- [Froese Fischer 1977] Froese Fischer C, *The Hartree-Fock Method for Atoms*, John Wiley and Sons (1977)
- [Goldstone 1957] Goldstone J *Proc Roy Soc Lond A* **239**, 267 (1957)
- [Grant 1970] Grant I P, *Adv Phys* **19**, 747 (1970)
- [Griffin et al 1983] Griffin D C and Pindzola M S, *Comments At Mol Phys* **13**, 1 (1983)
- [Griffin et al 1987] Griffith D C, Cowan R D and Pindzola M S, in *Giant Resonances in Atoms, Molecules and Solids* p 25, eds Connerade J P, Esteva J M and Karnatak R C, Plenum Press, New York-London (1987)
- [Gudat 1974] Gudat W, Kunz C and Karlau J, *Appl Opt* **13**, 1412 (1974)
- [Gunnarsson & Lundqvist 1976] Gunnarsson O and Lundqvist B I, *Phys Rev B*, **13**, 4274 (1976)
- [Haensel et al 1969] Haensel R, Radler K and Sonntag B, *Solid State Communications*, 1495 (1969)
- [Hansen 1972a] Hansen J E, *J Phys B At Mol Phys* **5**, 1983 (1972)
- [Hansen 1972b] Hansen J E, *J Phys B At Mol Phys* **5**, 1096 (1972)
- [Hansen et al 1975] Hansen J E, Fliflet A W and Kelly H P, *J Phys B At Mol Phys* **8**, L127 (1975)

- [Hansen et al 1989] Hansen J E, Brilly J, Kennedy E T and O'Sullivan G, *Phys. Rev. Lett.* **63**, 1934 (1989).
- [Hermann & Skillman] Herman and Skillman, *Atomic Structure Calculations*, Prentice-Hall, (1963).
- [Hertel et al 1992] Hertel I V, Steger H, de Vries J, Weisser B, Menzel C, Kamke B and Kamke W, *Phys. Rev. Lett.* **68**, 784 (1992).
- [Hohenberg & Kohn 1964] Hohenberg P and Kohn W *Phys. Rev.* **136**, 864 (1964).
- [Ivanov 1992] Ivanov V K, in *Vacuum Ultraviolet Radiation Physics*, eds. F. J. Wuilleumier, Y. Petroff and I. Nenner, proceedings of the 10th VUV conference, 178 (1992).
- [Ivanov et al 1993] Ivanov V K, Kupchenko V A and Shendrik M S, private communication (1993).
- [Ivanov 1994] Ivanov V K, private communication.
- [Jannitti 1979] Jannitti E, Cantù A M, Grisendi T, Pettini M and Tozzi G P, *Physica Scripta* **20**, 156 (1979).
- [Jannitti et al 1987] Jannitti E, Nicolosi P and Tondello G, *Physica Scripta* **36**, 93 (1987).
- [Jensen 1937] Jensen H, *Zeitschr. Phys.* **106**, 620 (1937).
- [Kelly 1963] Kelly H P, *Phys. Rev.* **131**, 684 (1963).
- [Kelly 1964] Kelly H P, *Phys. Rev.* **136**, 896 (1964).
- [Kelly 1987] Kelly R L, *J. Phys. Chem. Ref. Data* **16**, Suppl. 1 (1987).
- [Kiernan 1994] Kiernan L PhD. these (1994).

- [Koble 1991] Koble U Diplom thesis (1991)
- [Kohn & Sham 1965] Kohn W and Sham L J, Phys Rev **140**, 1133 (1965)
- [Kravis et al 1993] Kravis S, private communication (1993)
- [Kukk et al 1994] Kukk E, Aksela S, Aksela H, Sairanen O-P, Yagishita A, and Shigemasa E, J Phys B At Mol Opt Phys **27**, 1965 (1994)
- [Lieberman & Zangwill 1984] Lieberman D A and Zangwill A, Com Phys Comm **32**, 63 (1984)
- [Lyon et al 1986] Lyon I C, Peart B, West J B and Dolder K, J Phys B At Mol Opt Phys **19**, 4137 (1986)
- [Lyon et al 1987] Lyon I C, Peart B, West J B and Dolder K, J Phys B At Mol Opt Phys **20**, 1471 (1987)
- [Lucatoro & McIlrath 1980] Lucatoro T B and McIlrath T J, Applied Optics **19**, 3948 (1980)
- [Lucatoro et al 1981] Lucatoro T B, McIlrath T J, Sugar J and Younger S M, Phys Rev Lett **47**, 1124 (1981)
- [Madden & Codling 1963] Madden R P and Codling K, Phys Rev Lett **10**, 516 (1963)
- [Mansfield & Connerade 1976] Mansfield M W D and Connerade J P, Proc R. Soc Lond A, **352**, 125 (1976)
- [Martins 1994] Martins M, private communication, (1994)
- [Moore 1958] Moore C E 1958 Natl Bur Stand (U S ), Circ No 467 (U.S GPO, Washington, D C , Vol 3
- [Mosnier et al 1994] Mosnier J-P, Costello J T, Kennedy E T, Kiernan L and Sayyad M H, Phys Rev A, **49**, 755 (1994)

- [Nagata et al 1990] Nagata T, Yoshino M, Hayaishi T, Itikawa Y, Itotı Y, Kozumı T, Matsuo T, Sato Y, Shigenasa E, Takıazawa Y and Yagaıshıta A, *Physica Scripta* **41**, 47 (1990)
- [Nyholm et al 1986] Nyholm R, Helenelund K, Johansson B and Hornstrom S-E, *Phys Rev B*, **34**, 675 (1986)
- [Nuroh et al 1982] Nuroh K, Stott M J and Zaremba E, *Phys Rev Lett* **49**, 862 (1982)
- [Olsen & Lynch 1982] Olsen C G and W Lynch D W, *J Opt Soc Am* **72**, 88 (1982)
- [Pan et al 1987] Pan C, Carter S L and Kelly H P, *J Phys B At Mol Opt Phys* **20**, L335 (1987)
- [Radtke 1979a,b] Radtke E R, *J Phys B At Mol Phys* **12**, L71 & L77 (1979)
- [Richter et al 1988] Richter M , Meyer M, Pahler M, Prescher T, von Raven E, Sonntag B and Wetzel H E, *Phys Rev A* **39**, 5666 (1988)
- [Sairanen et al 1991] Sairanen O-P, Aksela S and Kivimaki A, *J Phys Condens Matter* **3**, 8707 (1991)
- [Sanchez & Martin 1990] Sanchez I and Martin F, *J Phys B At Mol Opt Phys* **23**, 4263 (1990)
- [Scherz 1990] Scherz U , *Theoretische Festkoerperphysik* Technische Universitaet Berlin (1990)
- [Schwob et al 1987] Schwob J L, Wouters A W, Suckewer S and Finkenthal M, *Rev Sci Instrum* **58**, 9, 1601 (1987)
- [Sontag & Zimmermann 1992] Sonntag B and Zimmermann P, *Rep Prog Phys* , 911 (1992)



- [Starace 1972] Starace A F, Phys Rev B **5**, 1773 (1972)
- [Starace 1974] Starace A F, J Phys B At Mol Phys **7**, 14 (1974)
- [Sugar 1972] Sugar J, Phys Rev B **5**, 1785 (1972)
- [Suzuki et al 1975] Suzuki S, Ishii T and Sagawa T, J Phys Soc Jpn **38** 156 (1975)
- [Ueda 1987] Ueda K, Phys Rev A **35**, 2484 (1987)
- [Wendin 1970a,b] Wendin G, J Phys B **3**, 455&466 (1970)
- [Wendin 1971] Wendin G, J Phys B **4**, 1080 (1971)
- [Wendin 1973] Wendin G, Phys Lett **46A**, 119, (1973)
- [Wendin 1975] Wendin G, Phys Lett **51A**, 291 (1975)
- [Wendin 1976] Wendin G, in *Photoionization and Other Probes of Many Electron Interactions*, ed F Wuilleumier, NATO Advanced Study Insitute Series, Plenum Press, New York, p 61, (1976)
- [Wendin 1982] Wendin G, *Many-Electron Effects in Atomic Physics* in New Methods in Atomic Physics, Les Houches Summer School (1982), North Holland (and references therein)
- [Wendin 1984] Wendin G *Application of Many-Body Problems to Atomic Physics*, Les Houches Summer School Session XXXVIII, eds Grynberg G and Stora R, Elsevier Sciences Publishers B V, p 555 (1984)
- [Zangwill & Soven 1980] Zangwill A and Soven P Phys Rev A, **21**, 1561 (1980)
- [Zangwill 1981] Zangwill A, PhD thesis (1981)
- [Zangwill 1983] Zangwill A in Atomic Physics 8, eds I. Lindgren, A Rosen and S Svanberg (Plenum Press, New York, 1983)

- [Zangwill & Liberman 1984] Zangwill A and Liberman D A, *Comput Phys Commun* **32**, 63 (1984)
- [Zangwill 1987] Zangwill A in *Giant Resonances in Atoms, Molecules and Solids* eds J P Connerade, J M Esteva and R C Karnatak, Plenum Press, New York-London (1987)
- [Zangwill 1987] Zangwill A, *J Phys C Solid State Phys* **20** L627 (1987)
- [Zimmermann 1976] Zimmermann P *Eine Einfuehrung in die Theorie der Atom-spektren*, Bibliographisches Institut AG (1976)

# Acknowledgements

First of all I would like to express my gratitude to Professor Eugene T Kennedy for his kindness taking me on as a postgrad student and his excellent guidance with inspiration and enthusiasm during this work

I am indebted to Dr John T Costello and Dr Jean-Paul Mosnier for the numerous helpful and stimulating discussions and proofreadings of the submitted papers and the presented thesis

I am grateful to Dr Michael Martins for numerous discussions concerning the Cowan codes and to Professor Vadim K Ivanov for various discussions about the RPAE method. Their support and contribution of theoretical results prior to publication had an immense impact on this work which is very much appreciated

I would also like to thank all postgrads of the Laser Plasma Group at DCU, especially Lawrence and Hassan for their good company in room N123

Last but not means least, I wish to thank Maicke and Detlef for their support, infinite patience and encouragement during my stay here in Ireland. Their immeasurable contribution is also very much appreciated